Quantitative evaluation of peptide analogue distribution in mouse tissue using 3D computer modelling

Jensen, Casper Bo

Publication date:
2017

Document Version
Publisher's PDF, also known as Version of record

Quantitative evaluation of peptide analogue distribution in mouse tissue using 3D computer modelling

Casper Bo Jensen

Kongens Lyngby 2017
PhD-2017-458

Technical University of Denmark
Department of Applied Mathematics and Computer Science
Richard Petersens Plads, building 324,
2800 Kongens Lyngby, Denmark
Phone +45 4525 3031
compute@compute.dtu.dk
www.compute.dtu.dk PhD-2017-458

Summary (English)

The use of automated image analysis of microscopy images is increasing to enable high throughput approaches and unbiased analysis of the increasingly large data sets produced. This thesis investigates the use of automated image analysis to quantify peptide analogue distribution in mouse brain tissue. The main group of peptides included in this work was glucagon-like peptide 1 receptors agonists (GLP-1RA) used for treatment in diabetes and obesity. Two main image modalities have been applied for image acquisition; Light Sheet Fluorescence Microscopy (LSFM), and slide scanner images of 2D histology sections. The work demonstrates the use of automated image analysis based on image registration to quantify LSFM data of the peptide brain distribution following peripheral administration. The methodology was expanded during the PhD work to also include study of receptor mapping and brain activation. The automated analysis was enabled by integration with a digital multimodality brain atlas from the Allen Institute of Brain Science (AIBS). The work showed that GLP-1RAs accessed multiple brain regions mainly in the hypothalamus and hindbrain and led to increased brain activation in regions related to decreased food intake. The developed integrated brain atlas provides a novel analysis approach for LSFM data to aid researchers understand the complex brain biology related to development of pharmaceuticals with brain mode of action.

Summary (Danish)

Brugen af automatiseret billedanalyse af mikroskopi-billeder stiger for at muliggøre analyse af store datasæt. I denne afhandling undersøges muligheden for at benytte automatiseret billedanalyse til at kvantificere hjernefordelingen af peptidanaloger i mus. Hovedgruppen af peptider undersøgt i dette arbejde var glucagon-like peptide 1 receptors agonister (GLP-1RAs) som bruges i behandling af diabetes og fedme. To typer af mikroskoper blev benyttet til dataopsamling; Light Sheet Fluorescence Microscopy (LSFM), og slide scanner billeder af 2D histologi sections. Arbejdet demonstrerer brugen af automatiseret billedanalyse til at kvantificere LSFM data af peptidfordeling i hjernen efter perifær injektion. I løbet af PhD projektet blev metoderne udvidet til også at tillade studie af receptorfordeling og hjerneaktivitet. Den automatiserede analyse bygger på integration med et multimodalt digitalt hjerneatlas fra Allen Institute of Brain Science (AIBS). Projektet viste at GLP-1RAs har adgang til adskillige hjerneområder primært i hypothalamus og baghjernen, og at de medførte øget hjerneaktivitet i områder relateret til nedsat fødeindtag. Det udviklede integrarede hjerneatlas muliggør en ny type af analyse af LSFM data som kan hjælpe forskere med at forstå den komplekse hjernebiologi relateret til udvikling af medicin med direkte effekter i hjernen.

Preface

This thesis was prepared at the Image Analysis and Computer Graphics Section at Department of Applied Mathematical And Computer Science at the Technical University of Denmark (DTU) in collaboration with the Histology and Imaging department, Global Research, Novo Nordisk A/S. The thesis was done in fulfillment of the requirements for obtaining a doctor of philosophy (PhD) within the topic of image analysis. The work presented in the thesis was financed by Innovation Fund Denmark and Novo Nordisk A/S. The thesis presents research concerning automated image analysis of microscopy images of biological tissue, mainly describing brain distribution, receptor localization, brain activation and brain connectivity in connection with peptides involved in regulation of appetite and food intake. The first part of the thesis presents the theoretical background for pharmaceuticals with brain mode of action, together with background on the applied instruments and analysis methods. The second part presents the major findings and put these into the context of the presented methodologies. Finally, the thesis is concluded, and followed by five manuscripts that were prepared during the PhD project. The project has been supervised by associate professor Anders Bjorholm Dahl and research scientist Anna Secher, and co-supervised by Professor Knut Conradsen and research scientist Jacob Hecksher-Sørensen. The research has been carried out at DTU and Novo Nordisk A/S. External research was conducted at Novo Nordisk Research Center Seattle in combination with visits to the Allen Institute of Brain Science.

Lyngby, 31-August-2017

Casper Bo Jensen

Acknowledgements

I would like to sincerely thank my supervisors Anders Bjorholm Dahl, Anna Secher, Knut Conradsen, and Jacob Hecksher-Sørensen for their valuable and encouraging support throughout the project. Both professionally and personally. Also a big thanks to Rasmus Larsen who supervised the first part of the project, and to Anda Cornea and Aaron Mercer for welcoming me and hosting me in Seattle. Acknowledgements also go to my former and current colleagues at the Image Analysis and Computer Graphics section. Especially, Mark Lyksborg and Kasper Marstal for scientific sparring and collaboration on manuscripts. The same acknowledgements go to Lotte Bjerre Knudsen, Tess Tsai-Hsiu Lu, Sanaz Gabery and Tomas Alanentalo, colleagues from Novo Nordisk. I would also like to thank Jeanette Bannebjerg Johansen, Heidi Solvang Nielsen, Hanne Duus Laustsen, Maibritt Pedersen and Steen Kryger for helping me with laboratory work at Novo Nordisk. I would like to thank my family for being loving and supportive. Finally, a great appreciation to Ida for always being there: Always proud, but newer impressed.

Contributions

Papers included in this thesis

Paper A

Casper Bo Jensen, Tess Tsai-Hsiu Lu, Sanaz Gabery, Kasper Marstal, Tomas Alanentalo, Aaron Jeffrey Mercer, Anda Cornea, Knut Conradsen, Jacob Hecksher-Sørensen, Anders Bjorholm Dahl, Lotte Bjerre Knudsen, Anna Secher. *Integrated Brain Atlas for Unbiased Mapping of Nervous System Effects Following Liraglutide Treatment*, under submission, 2017.

Paper B

Casper Bo Jensen, Charles Pyke, Morten Grønbech Rasch, Anders Bjorholm Dahl, Lotte Bjerre Knudsen, Anna Secher. *Characterization of the glucagon-like peptide-1 receptor in mouse brain using a novel antibody and in situ hybridization*, submitted to Endocrinology, 2017

Paper C

Casper Bo Jensen, Anna Secher, Jacob Hecksher-Sørensen, Knut Conradsen, Rasmus Larsen. *Quantification of Brain Access of Exendin-4 in the C57BL Mouse Model by SPIM Fluorescence Imaging and the Allen Mouse Brain Reference Model*, Scandinavian Conference on Image Analysis. Springer, Cham, 2015.

Paper D

Casper Bo Jensen, Tomas Alanentalo, Knut Conradsen, Anders Bjorholm Dahl, Jacob Hecksher-Sørensen, Anna Secher,. *Whole brain pStat3 activation: Why leptin is not a good obesity treatment*, under preparation, 2017

Paper E

Casper Bo Jensen, Mark Lyksborg, Jacob Hecksher-Sørensen, Anna Secher, Knut Conradsen, Anders Bjorholm Dahl. *Active appearance segmentation for intensity inhomogeneity in light sheet fluorescence microscopy.* Biomedical Imaging (ISBI), 2016 IEEE 13th International Symposium on. IEEE, 2016.

Abstracts not included in this thesis

Casper Bo Jensen, Anna Secher, Jacob Hecksher-Sørensen, Tess Tsai-Hsiu Lu, Pernille Barkholt, Knut Conradsen, Anders Bjorholm Dahl, Jacob Jelsing, Niels Vrang, Lotte Bjerre Knudsen. *Quantification of Semaglutide Distribution and Action in Mouse Brain Regions Associated with Reward and Food Intake*, Abstract and poster at American Diabetes Association's conference, 2017

Aaron J. Mercer, Anda Cornea, Jarrad M. Scarlett, Jenny Brown, Hong T. Nguyen, Casper Bo Jensen, Frank H. Koegler, Michael W. Schwartz, Kevin L. Grove, *Central distribution of FGFR1c and beta klotho: Implications for FGF21 and FGF19 pharmacotherapies*, Abstract and poster at Neural Control of Appetite, Metabolism and Weight, Keystone Symposia, 2017

List of Abbreviations

AIBS	allen institute of brain science
BBB	blood brain barrier
BMI	body-mass index
CCFv3	common coordinate framework version 3
chpl	choroid plexus
CNS	central nervous system
CSF	cerebrospinal fluid
CVO	circumventricular organ
DBE	dibenzyl ether
DIO	diet induced obese
FDR	false discovery rate
GI	gastrointestinal
GLP-1	glucagon-like peptide 1
GLP-1R	glucagon-like peptide 1 receptor
GLP-1RA	glucagon-like peptide 1 receptor agonists
EGFP	enhanced green fluorescent protein
IEG	immediate early gene
IHC	immunohistochemical
ISH	in situ hybridization
LepRb	leptin receptor, long form
LSFM	light sheet fluorescence microscopy
MI	mutual information
rNGF	regularized normalized gradient field
SD	standard deviation
AAM	active appearance model
AAV	adeno-associated virus

For abbreviation and full name of brain regions please refer to Appendix F.

Contents

Chapter 1

Introduction

The work in this industrial PhD project was funded in part by the Innovation Fund Denmark. The activities within the fund aim to strengthen the collaboration between academia and industry. The project was performed in collaboration with Novo Nordisk A/S, a pharmaceutical company with marketed treatment options within diabetes, hemophilia, growth hormone therapy, hormone replacement therapy, and obesity. Over the last three decades, mean body-mass index (BMI) has increased by 0.4 kg/m^2 per decade worldwide [FSC+11], and in the US the prevalence of obesity was 35.5% among adult men and 35.8% among adult women in 2009-2010 [FCKO12]. Further, the prevalence of the extreme weight categories (BMI>40 and >50) increased more than 70% from 2000-2010 [SH13]. The dramatic increase in the prevalence of obese and overweight individuals has intensified interest in obesity as a major health problem. For the individual the consequence of obesity is an increased risk of acquiring metabolic diseases like type II diabetes and cardiovascular disease [C+09]; and for society the economic burden is pushing the already stretched healthcare budgets [CM12]. Thus the development of treatment options for obesity has long been in focus for many in the pharmaceutical industry, but so far very few companies have been successful. One reason for this is that the so far most effective treatment options primarily function through the brain. The brain has limited access from the periphery were pharmaceutical compounds are often delivered, and also potential for unwanted side effects. For pharmaceutical compounds to work directly in the brain they must be able to access the brain in select regions or by crossing the blood brain barrier (BBB). Thus the future design of treatment options will benefit from a better understanding on how and where pharmaceutical compounds enter the brain. Research is ongoing regarding how the pharmaceutical compounds or naturally occurring peptides enters the brain from the blood [LLL+13], [PK01]], but the brain distribution of pharmaceuticals are still poorly understood due to lack of good experimental methods.

A technology which might overcome these limitations is LSFM which is a non-destructive, *ex vivo* method to produce well-registered optical sections suitable for 3D reconstruction [DLS+07]. This allows researchers to visualize the distribution of fluorescently labelled peptides in the whole mouse brain. Recently, LSFM has further been used to evaluate whole mouse brain activation [RAK+16] which is another important aspect when researching the effect of pharmaceuticals. However, as the image detail is approaching single cell resolution the data sets become enormous and high throughput quantitative and unbiased analysis is only possible using appropriate software programs. In order to accelerate the speed and quality of the results obtained from LSFM it will be important to develop computer algorithms to assist in the analysis. The development of such algorithms is the main purpose of this PhD project. The chosen analysis approach has been focused on computational atlases which are increasing in neuro-imaging and employed in various imaging modalities both in humans and animal models [FEB+11], [LHA+07]. Digital atlases are produced by computation of averages of ensembles of segmented images after image registration [WZW04],[VL09]]. A new image can then be analysed by image registration to the atlas (average image) and superimposition of the segmented structures from the atlas.

An important family of obesity treatment options is modified peptides based on the natural occurring glucagon-like peptide 1 (GLP-1) molecule released in the intestine in response to food intake, and a neurotransmitter produced in the hindbrain. It has been shown that GLP-1RAs act on peripheral organs but also target GLP-1 receptors (GLP-1R) in the brain, and that this contributes in large part to the weight loss effect [SJB+14], [SGAS+14]. Another naturally occurring peptide is leptin, which is released from fat tissue and provides information on body energy status to the brain by activating the long form of its receptor (LepRb). Leptin is thus also part of the system that controls food intake and energy homeostasis [FH98]. The automated analysis approach developed during this PhD project was used to investigate brain actions of GLP-1RAs and leptin when administered peripherally to mimic treatment of patients.

1.1 Laboratory Work

A large amount of experimental and laboratory work have been performed during the course of the PhD project. The work has mostly concerned tissue preparation and image acquisition using LSFM. The process has been important as variations in the laboratory work directly shows up in the images as different artifacts which is a challenge to the automated quantitative analysis. As a data analyst it is in general important to be somewhat part of the experiments in order to understand and optimize the process. The following paragraphs outline the laboratory work performed in the project. Tissue samples of the mouse brain have been the main focus throughout the thesis. The samples have been imaged either in 3D using LSFM, or as 2D sections using classical histology. Both image platforms are used with *ex vivo* tissue samples that require preparation prior to image acquisition. Paper A, C, D, and E include whole brain data obtained with LSFM. The laboratory work included tissue extraction, fixation, clearing, mounting and setting up the LSFM acquisition sequence. An important

learning was that variations in the clearing protocol led to large differences in the amount of tissue deformation observed in the brain samples, which again was an important factor when evaluating the image segmentation quality. The images in Figure 1.1a shows some of the laboratory work performed with LSFM imaging. Paper A and B include imaging and analysis of 2D histology sections of paraffin embedded brain samples. In the acquired images the largest artifacts were related to physical damage during the tissue cutting. Another important learning was that the tissue cutting rarely was performed at the orthogonal angles otherwise strived for. This was important when performing image registration to 2D atlases often produced with orthogonal angels, e.g. coronal sections.

1.2 Objectives

The main objective of this thesis was to develop algorithms for automated quantification of whole mouse brain LSFM data. The developed computational approach should allow high throughput quantification to be accomplished. Figure 1.1b-d shows an example of LSFM data where segmentation of brain regions allows quantification of the fluorescent signal.

The aim of the brain atlas to be constructed based on images from LSFM was to provide a valuable resource for current and future research investigating peptide access to the mouse brain. During the project the objective broadened from peptide access to further include investigation of brain activation, peptide receptor mapping, and to some extend brain connectivity.

The conducted experiments have focused on GLP-1RAs and leptin, and their application as anti-obesity treatment options.

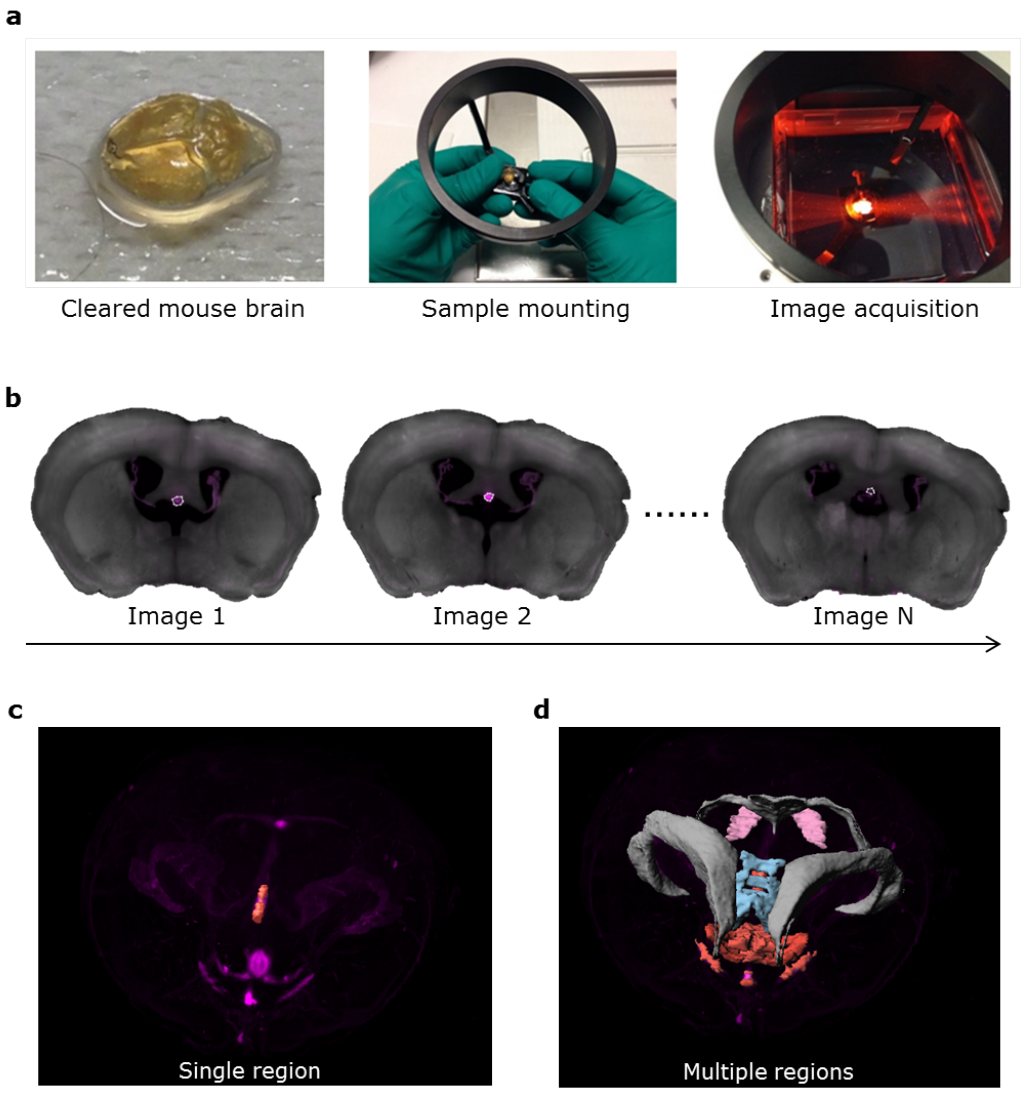

Figure 1.1: (a) Left: cleared mouse brain. Middle: mounting of brain sample. Right: Mounted brain sample inside imaging chamber scanned with a laser light sheet. (b) Examples of 2D coronal projections from the 3D LSFM acquisition. Manual segmentation of brain regions would require going through many such images and drawing brain structures by hand. (c) Example of an annotated brain structure in 3D. (d) Example of multiple brain region annotations applied in 3D. These annotations were obtained using a digital brain atlas to automate the analysis process.

1.3 Thesis Overview

The thesis consists of two parts followed by a part with the contributions, i.e. the manuscripts which represent the scientific findings in the thesis. Part I presents the methodology and theoretical background concerning peptides, the utilized microscopy systems, image analysis, and statistical framework. Part II of the thesis explains how the methodology has been applied to obtain the results in the contributions. Part II should be seen as the link between the methodology and the contributions. The thesis is concluded as the last chapter in Part II. The contributions are included in Part III in their current layout.

Part I

Methodology

Chapter 2

Central regulation of appetite

This section describes central regulation of appetite in connection with peptide hormones. This is a vast topic and the focus will be limited to a subset of systems most relevant for the work conducted in this PhD project. This includes two peptide hormones; GLP-1 and leptin, which are hormones both part of the exchange of information between the brain and other organ systems. This is followed by a description of brain access looking at how these peptides may reach the brain, and a description of what brain activation might occur as response to the peptides entering the brain.

2.1 Peptide hormones

Communication between the brain and other organ systems are important in order to maintain energy homeostasis. This communication can take place through electric signaling conducted through nerves such as the vagus nerve which provide connections between the gastrointestinal (GI) tract and the brain. The communication can also be facilitated through hormones released from specialized cells to travel through the blood to the brain (Fig 2.1). Two such peptide hormones involved in the control of food intake are GLP-1 and leptin. The pharmaceutical industry has attempted to create treatment options for diabetes and obesity based on these natural occurring peptides by developing agonists with improved pharmacokinetics. The efforts have been successful concerning GLP-1 where several marked treatments are available for type II diabetes and one for obesity, namely liraglutide marked under the brand name Saxenda. Treatment options based on leptin have not succeeded.

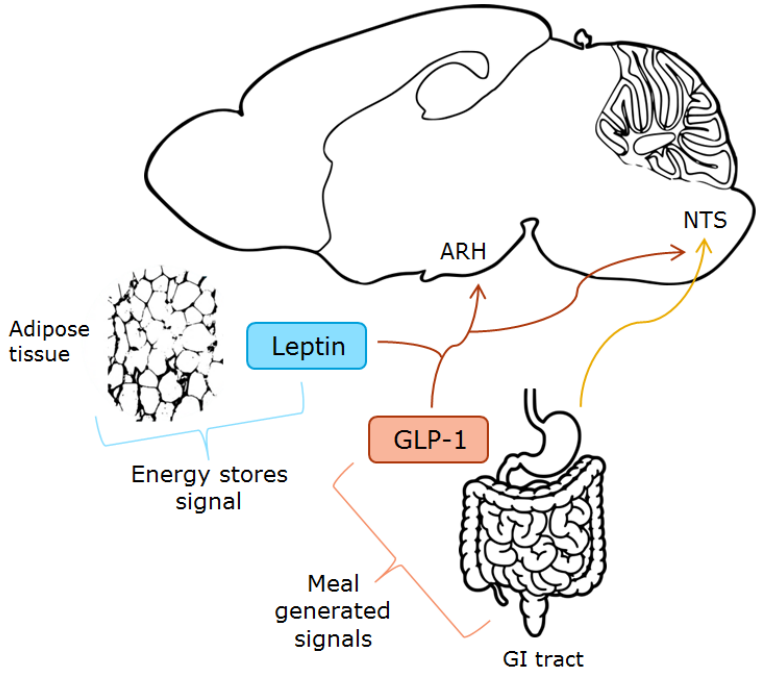

Figure 2.1: Sketch showing examples of how the mouse brain receives information from the periphery. Leptin is released from adipose tissue into the vascular system to signal the level of energy storage. Satiety signals from the GI tract are transmitted through the vagus nerve and through the vascular system. Important brain regions receiving the information are arcuate nucleus (ARH) in the hypothalamus, and nucleus of the solitary tract (NTS) in hindbrain.

2.1.1 GLP-1

GLP-1 is an incretin hormone released from gut endocrine L-cells following meal ingestion. GLP-1 has an important role in regulating insulin release by activation of the GLP-1R expressed on pancreatic beta cells thereby normalizing blood glucose levels [ZMMH02]. GLP-1 is also produced and released as a neurotransmitter from hindbrain neurons [TC15]. The GLP-1R distribution is abundant in the brain [MLS99], [CRH$^+$15], and these receptors can potentially be activated both by the endogenous GLP-1 produced in the brain and/or by circulating GLP-1 from the periphery. The fact that GLP-1Rs are expressed in many brain regions indicate diverse actions of this peptide, many of which has been discussed before [VL10], [DCZ$^+$03]. Following peripheral administration longer acting GLP-1RAs affect appetite [VCSJ$^+$14] and lower bodyweight [OGGC$^+$16] likely through mechanisms in the brain [SJB$^+$14], [SGAS$^+$14]. Liraglutide is a GLP-1RA approved and widely used for the treatment of diabetes [NHF$^+$06], and is also approved as a treatment option for weight management, reducing appetite and body weight following peripheral once-daily administration [OGGC$^+$16].

2.1.2 Leptin

Leptin is a peptide hormone encoded by the ob gene expressed mainly in adipose tissue. Secretion of leptin from adipocytes provides information on body energy status to the brain by activating LepRb [BSD+03]. Leptin has been showed to control food intake and energy homeostasis [FH98]. Like GLP-1R the LepRb is abundantly expressed throughout the mouse brain. The highest concentrations of LepRb neurons are found in the hypothalamus, such as the ventral premamillary (PMv), Dorsomedial nucleus of the hypothalamus (DMH), and ARH [PLJM11] which are important centers for regulating feeding [EES99]. Besides controlling energy homeostasis leptin is also involved in regulating body temperature and supporting reproductive function [MMLL09]. The ob gene is needed to produce functional leptin, and the db gene is needed for the cells to produce LepRb. Recessive mutations in either the ob or db genes result in obesity and diabetes in a syndrome resembling morbid human obesity [Col78], [CCT+96]. Without a functioning leptin system *ob/ob* and *db/db* mice models obtain identical phenotypes, each weighing three times more than normal mice. Leptin replacement therapy in humans with leptin deficiency caused by genetic mutation can restore a lean phenotype. However, when the obesity is instead caused by increased energy intake the state is related to hyperleptinemia and leptin tolerance or leptin resistance [BM09].

2.1.3 Brain access

Molecular traffic between the periphery and the central nervous system (CNS), as is needed to deliver potential therapeutics to specific areas of the brain, is restricted by brain barriers. The most well-known barriers are the BBB and the blood-cerebrospinal fluid (CSF) barrier. As an example the hypothalamus is restricted by a BBB composed of tight junctions between endothelial cells lining brain microvessels [NBF+11]. However, circumventricular organs (CVOs) containing fenestrated capillaries allowing free access of blood borne molecules exists in the brain. Examples of CVOs include area postrema (AP), median eminence (ME), vascular organ of the lamina terminalis (OV), and subfornical organ (SFO). Another example of structures with fenestrated capillaries are the choroid plexus (chpl) located in the ventricular system, e.g. the fourth (V4) and lateral (VL) ventricle. Recent literature suggests the ME to be a site for uptake of peripheral peptides such as leptin from the blood [SLL+13], [BDL+14] and this could be extended to include GLP-1RAs. Indeed nearly all CVOs including the ME have a high expression of GLP-1R suggesting interaction of peripheral GLP-1 in these regions. In this PhD work we have utilized fluorescently labelled peptides to investigate brain access of different peptides. The labelled peptides were injected either subcutaneous or intravenous and allowed to distribute for a number of hours having the possibility to access the brain. The mice were then euthanized and the brains were extracted for LSFM imaging.

2.1.4 Brain activation

If the circulating peptides access the brain and bind their receptor, the targeted cells may be activated. The binding of a receptor may initialize several downstream signals within the cells. As an example downstream Stat3 signaling mediates the effects of leptin on melanocortin production and body energy homeostasis [BSD$^+$03]. In the process of signaling Stat3 becomes phosphorylated and thus referred to as pStat3. During the work in this PhD thesis pStat3 signaling were imaged by using whole mount staining [RWS$^+$14] with a primary pStat3 antibody. However, it should be noted that pStat3 signaling is not leptin receptor specific and may also be initiated by other molecules. Likewise, pStat3 is not the only mediator of leptin action [RLM08].

The study of direct brain activation from GLP-1R is more difficult as no direct marker is available. An alternative is to use a broad activation marker such as c-Fos, which is part of the family of immediate early genes (IEGs) whose expression levels reflect recent changes in neuronal activity [RAK$^+$16]. IEGs have low temporal resolution, and up-regulation of their expression usually lags neuronal stimulation by 30 minutes. Their expression can outlast the end of activity by several hours. During the work in this PhD thesis c-Fos was used to investigate the brain activation following peripheral administration of GLP-1RAs. In the discussion of brain activation it is important to note that receptor binding by a ligand can not always be visualized by c-Fos expression. Also the receptor binding may can cause inhibition, e.g. lower or no c-Fos activation compared to baseline activity level.

Neurons project widely in the brain to convey information from one region to the other. Thus direct activation in one brain region may lead to secondary activation in other brain regions forming complex neuro-circuits. A way to study brain connectivity is using recombinant adeno-associated virus (AAV), expressing EGFP to perform anterograde tracing of axonal projections [CDdLS98]. Such analysis was performed in large scale by AIBS to create a mesoscale connectome of the adult mouse brain [OHN$^+$14]. These connectivity maps have been downloaded and used to add context to some of the LSFM experiments performed regarding brain activation.

Chapter 3

Imaging systems

This chapter presents the imaging systems used in this PhD thesis. LSFM has been used to acquire 3D data of the whole mouse brain, while a slide scanner has been used to acquire 2D images of histology sections. The main focus has been on LSFM, where much work has also gone into optimization of tissue preparation and scan sequences. The slide scanner has been used with a standard setup.

3.1 LSFM

LSFM is a non-destructive method to produce well-registered optical sections suitable for 3D reconstruction. The system provides high sensitivity, micrometer resolution, and short acquisition time enabling imaging of a whole mouse brain in less than one hour [DLS+07]. LSFM belongs to the family of light microscopes, hence the contrasts available for imaging are based on fluorescence properties of the molecules in the sample. This also implies that samples must be chemically cleared prior to imaging, to allow the light sheet to illuminate the sample with minimal scattering.

3.1.1 Microscope setup

The LSFM system used during this Phd work is seen in Figure 3.1a. A broad spectrum laser is led into the microscope where a series of optical elements such as mirrors and lenses shape the laser beam into a thin light sheet with a gaussian beam profile (Fig. 3.1b). Prior to beam shaping unwanted wavelengths are filter away providing a specific excitation wavelength. The light sheet illuminates a sample located inside a dibenzyl ether (DBE) filled imaging chamber and excites molecules in the sample. Photons emitted from the sample in response to excitation are observed by a microscope zoom body. The

emitted light is filtered providing a specific emission wavelength. A sCMOS camera produces digital 2D images of the sample. To acquire a 3D volume a step motor moves the sample in small increments through the light sheet. The sequence can be repeated to acquire multiple contrasts of the same sample using different filter settings.

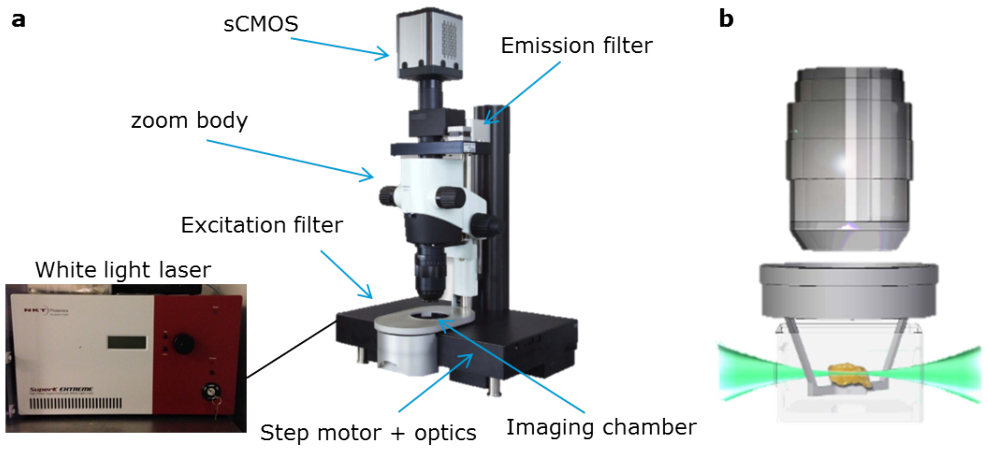

Figure 3.1: (a) LSFM system used during the Phd work. The microscope is a Lavision II setup from Lavision Biotec. A white light laser from NKT photonic delivers the laser which are shaped into a light sheet and used to excite the sample positioned inside the imaging chamber. Emitted light from the sample travels through a zoom body and images are acquired with a Andor NEO sCMOS camera. (b) Illustration of a light sheet (green) which illuminates a tissue sample (yellow). Image reproduced by permission from Lavision Biotec.

3.1.2 Tissue preparation

To obtain transparent samples mice were euthanized by cardiac perfusion and the brain extracted. Following extraction the tissue was fixed to avoid further degradation by enzymes and to avoid diffusion of ligands from receptors. Depending on the desired contrast mechanism a whole brain staining protocol was applied. In this thesis work the iDISCO protocol [RWS+14] was used. The final step in tissue preparation was tissue clearing where a solvent-based approach was used to obtain cleared samples when imaged in DBE [EBJ+12]. The tissue preparation often lead to artifacts in the imaged brain seen as mechanical damage from tissue extraction, and shrinkage and deformation from fixation and clearing. The process is summarized in Figure 3.2a-b.

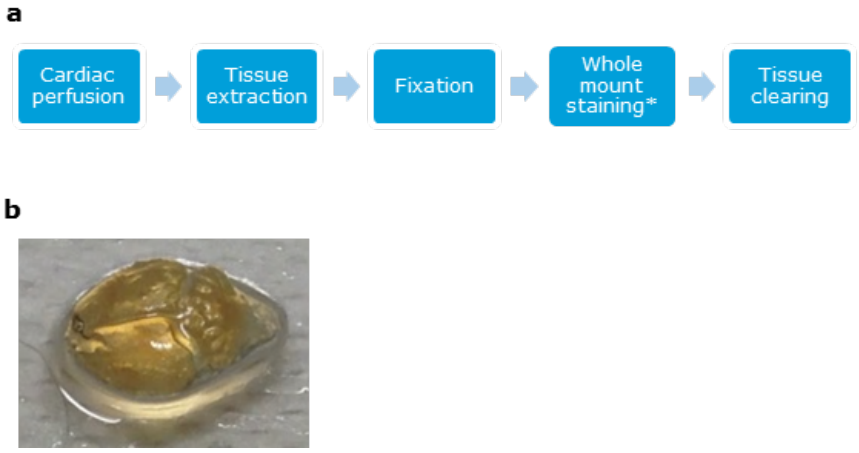

Figure 3.2: (a) Tissue preparation steps to obtain a mouse brain sample for LSFM imaging. *Whole mount staining is not performed if the study involves flurescently labelled peptides. (b) Cleared mouse brain (yellow). The cleared brain will become transparent when emerged into a DBE filled imaging chamber.

3.1.3 Contrast mechanisms

As the name implies the contrast mechanisms of LSFM is based on fluorescence. Fluorescence is a property of some molecules which enables them to take up energy from light at a specific wavelength (excitation) and shortly after release energy in form of light at a slightly shifted wavelength (emission). Excitation and emission wavelengths are specific for different molecules which are utilized during imaging. Different molecules of normal human and animal tissue are fluorescent which is normally termed auto-fluorescence. Auto-fluorescence has a broad excitation and emission spectrum, but is normally most intense at lower wavelengths. During this Phd project the auto-fluorescence from brain tissue was recorded and used for anatomical information (Fig 3.3). It was observed that different tissue preparation protocols influenced the auto-fluorescence, especially the white matter of the brain. Also regarding the white matter a discovery was made enabling a strong contrast in the white matter tracts by the use of an emission filter and excitation filter with identical wavelengths. To study the brain distribution of peptides of interest a commercial fluorescent molecule with known spectra characteristics was chemically attached to the peptide (Fig 3.3). A similar approach was used with whole mount IHC staining where a commercial fluorescent molecule was attached to a secondary antibody which would then bind to a primary antibody to detect an antigen of interest.

Contrast mechanism	Filter settings	Image example - overview	Image example – zoom
Auto-fluorescence	Excitation: 545 nm Emission: 620 nm	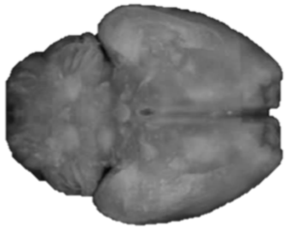	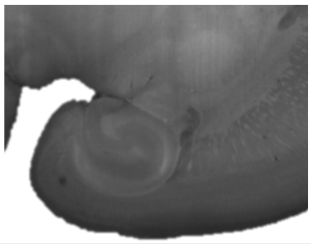
Auto-fluorescence, *white matter enhanced*	Excitation: 620 nm Emission: 620 nm	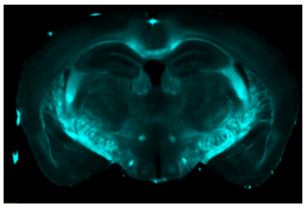	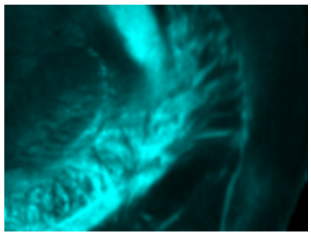
Labelled peptide	Excitation: 620 Emission: 710 nm	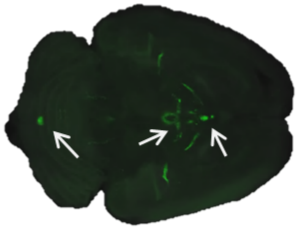	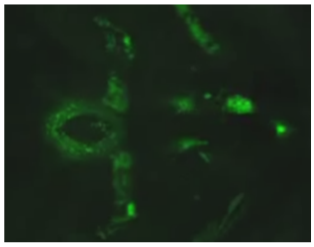
Whole brain staining	Excitation: 545 Emission: 620 nm	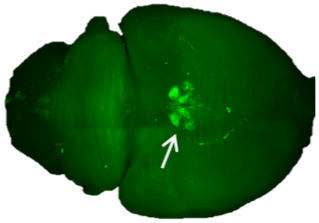	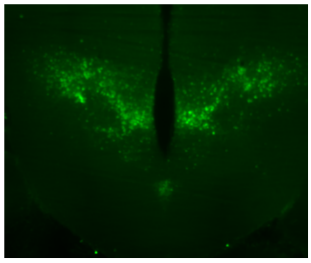

Figure 3.3: Overview of the LSFM contrast mechanisms used during the Phd work. White arrows indicate specific signals from commercial fluorescent molecules. Filter settings refer to the settings of the LSFM microscope during data acquisition. Image examples are either 3D maximum intensity projections or 2D projections. Please note that the microscope acquires light intensities, i.e. produces grayscale images. Color maps are applied for visualization purposes only.

3.2 Slide scanner

A slide scanner is a form of light microscope constructed such that many 2D slides with thin tissue samples may be loaded into the scanner simultaneously. The slides are imaged one by one and saved as digital files usually in a pyramid format enabling zoom up to 40X. Slide scanners are available for both fluorescence and chromogene stained tissue samples. In this Phd work data was obtained using chromogene stained tissue samples.

3.2.1 Tissue preparation

After tissue removal the first tissue preparation step was fixation performed to preserve structure. The fixation will terminate cell metabolism, prevent enzymatic degradation, kill potential pathogenic microorganisms, and fix lignads to receptors. Next, the tissue sample must be embedded in a medium that allows it to be cut into thin sections. In the work of this thesis, sections were dehydrated and embedded in paraffin. Lastly, the paraffin block containing the tissue is mounted in a microtome and cut into thin slices and placed on glass slides before imaging.

3.2.2 Contrast mechanisms

Contrast dyes, such as e.g. hematoxylin will broadly stain cellular components of the tissue with graduated intensity. Specific stains will on the other hand only stain specific components of the tissue leaving the rest of the tissue unstained. Examples of a specific staining techniques are immunohistochemical staining (IHC) and *in situ* hybridization (ISH).

Neurons are the primary cell type of brain tissue. Neurons consist of a cell body from which an axon of varying length transmit electronic signal from the neuron to other neurons. In the light microscope the ribosomal content of the cell body appears as small bodies, called Nissl bodies, and these stain intensely with basic contrast dyes [RP06]. This was utilized to obtain anatomical information from brain tissue (Fig 3.4). IHC staining is based on reactions between antigens and antibodies. Antibodies, also called immunoglobulins, are glycoproteins produced by the immune cells in response to foreign proteins called antigens. A pair of antibodies and antigens will bind upon meeting. This specific binding may then be examined in the microscope and thereby provide a specific staining of the antigen of interest [RP06] (Fig 3.4). ISH is part of the family of hybridization techniques where single-stranded RNA or DNA molecules interact with complementary nucleotide sequence, called a nucleotide probe. With ISH the binding between probe and singled stranded RNA or DNA is performed within cells or tissues, such as in thin histology sections. In this Phd work a recent developed commercial ISH platform based on non-radioactive chromogene detection was used to detect mRNA [AZM$^+$16], [WFS$^+$12] (Fig 3.4).

Contrast mechanism	Staining type	Image example - overview	Image example – zoom
Neuronal cell bodies	Nissl stain	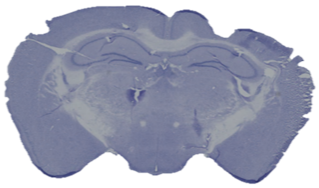	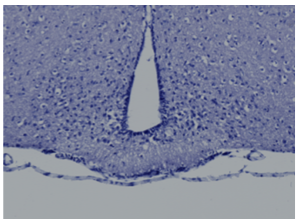
Antigen (e.g. protein)	IHC		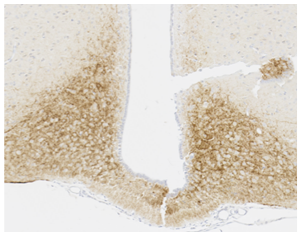
Single stranded RNA	ISH		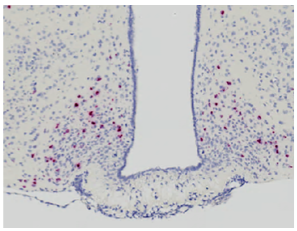

Figure 3.4: Overview of the histology contrast mechanisms used during the Phd work. For the IHC example brown color show positive stained cells. With ISH the red dots show positive stained cells. Details on the exact staining protocols such as information about antibodies, RNA probes, etc. are provided in the individual papers.

Chapter 4

Image analysis

This chapter describes a number of subjects within automated image analysis. First, a digital brain atlas is introduced, followed by a description of image registration used to align samples based on the atlas. The next sections describe the methods applied to extract specific information from the microscopy images, including spectral unmixing and image segmentation methods. A description of the statistical methods applied in this thesis work is also provided, and lastly a description of an alternative segmentation approach based on active appearance models (AAMs).

4.1 Digital brain atlas

Currently, no digital brain atlas is public available constructed from LSFM data. However, a high quality atlas also based on auto-fluorescence is available from AIBS constructed from two-photon microscopy images [OHN+14]. This atlas was used as basis for analysis of LSFM data.

4.1.1 AIBS atlas

The AIBS data portal holds many open access resources for brain research. Most data regarding the mouse brain is aligned to the Common Coordinate Framework version 3 (CCFv3) reference space based on a template brain constructed from 1675 specimens (Fig 4.1a). A number of resources are coupled to this template brain such as detailed annotations, a histology based template, and a range of neural connectivity maps (Fig. 4.1b-d). During the PhD project these data have been linked to LSFM as well as 2D histology data.

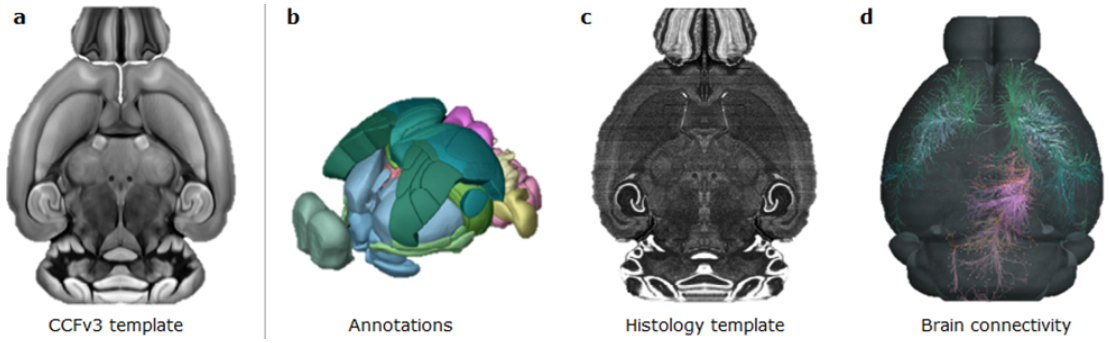

Figure 4.1: (a) CCFv3 template based on two-photon microscopy images from 1675 individual mouse brains. (b) Detailed annotations constructed to fit the CCFv3 template. (c) Aligned template re-constructed from 2D Nissl stained histology sections. (d) Neural connectivity maps constructed from mouse brains after stereotactical injection of AVV to trace axons projecting out from the injection site. Figure modified from [oBS17].

4.2 Image registration

To utilize the digital brain atlas a moving image (individual brain sample) $I_M(x)$ must be deformed to fit a fixed image (atlas template) $I_F(x)$. The images have dimension d and are defined on their own spatial domain: $\Omega_F \subset \mathcal{R}^d$ and $\Omega_M \subset \mathcal{R}^d$, respectively. With LSFM d=3 and with histology sections d=2. Image registration is now the problem of computing a transformation $T(x) = x + u(x)$ that makes $I_M(T(x))$ spatially aligned with $I_F(x)$ [KS15] (Fig 4.2a). In the PhD work a global affine coordinate transformation for initialization followed by non-rigid b-spline coordinate transformation for local deformations was utilized. The underlying image is then deformed by manipulating a defined mesh of control points based on the b-splines. The number of control points is important in regards to regularization, i.e. how much deformation is allowed. Determining the right amount of regularization is important as too much regularization will restrict the deformation not reaching the optimal solution, while too little regularization will lead to unrealistic deformations in the image. A fast way to regularize the deformation is to apply multi-level b-splines [SRQ$^+$01] where the final local transformation is the sum of the transformations at each level. To compute the most optimal transformation aligning $I_M(x)$ to $I_F(x)$ a similarity measure is needed. The simplest similarity measure is sum of squared differences (SSD) which works well in situations where the images originate from the same modality and contains similar intensity distributions. A similarity measure which is applicable in a wider range of situations, e.g. cross modality registrations, is mutual information (MI) [SHH99]. These similarity measures were used for different registrations during this PhD work. To obtain the most optimal transformation it is common to use an iterative optimization strategy such as gradient descent. The number of iterations will influence the amount of deformation, with less iterations providing a higher degree of regularization. In the work presented in this PhD thesis two libraries were utilized for computing and applying transformations, namely Elastix [KSM$^+$10], and IRTK [RSH$^+$99], [SRQ$^+$01].

4.2.1 LSFM studies

To avoid cross-modality cross-subject registrations a LSFM template was constructed and aligned to the AIBS atlas. This template was based on one representative mouse brain. Once constructed this template was used to align other LSFM samples to the AIBS atlas. As mentioned in Section 3.1.2 a number of tissue preparation steps are performed prior to LSFM acquisition. The preparation step can cause large deformation of the tissue (Fig 4.2a). The tissue shrinkage was observed to be non-uniform in different parts of the brain which meant that the standard approach of applying an affine transformation to account for global deformation was not adequate in this situation. To mitigate the effects of the non-uniform tissue shrinkage a registration model which allowed different degrees of shrinkage in each of the larger brain structures was developed. In practice this was enabled by performing a pre-segmentation to divide the brain into ten larger structures by image registration with low regularization allowing large deformations. Next, an affine and b-spline transformation as described in Section 4.2 was performed for the ten individual brain structures and combined to yield the final registration result (Fig 4.2b).

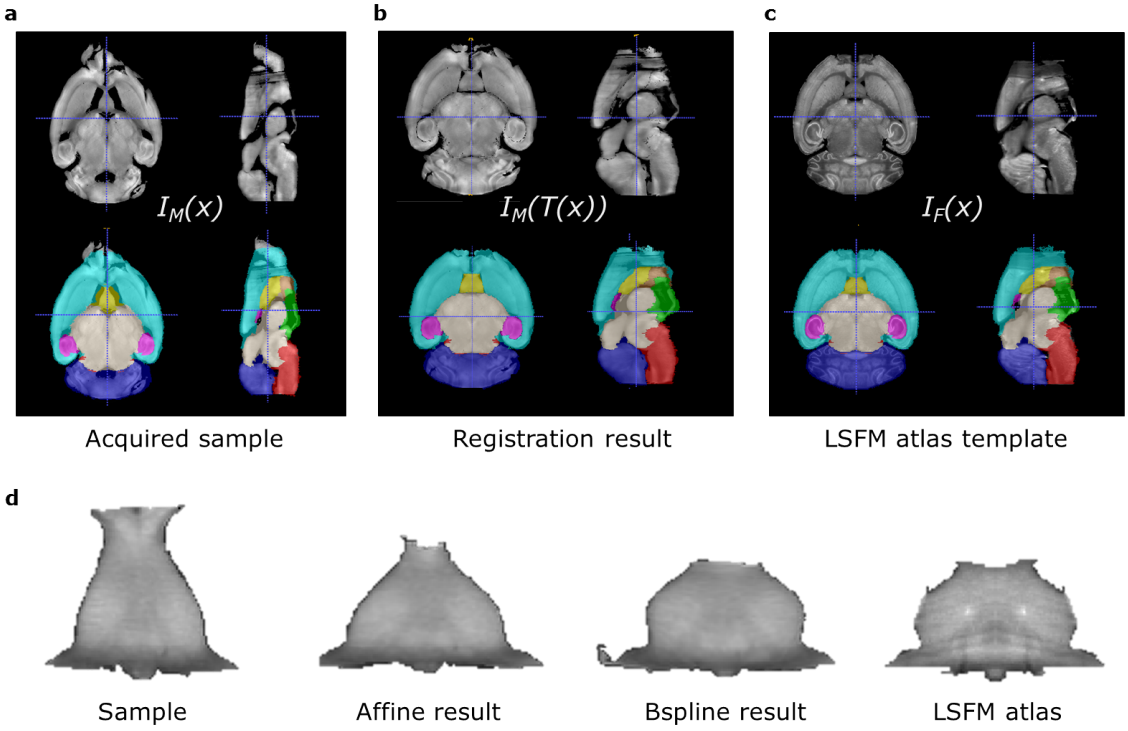

Figure 4.2: (a) Example of acquired brain sample to be registered to the LSFM template of the integrated brain atlas. (b) The result of aligning the sample to the LSFM template. The registration was performed in separate parts to mitigate non-uniform deformations. Separate affine and b-spline registration was performed for ten larger structures, here visualized by the overlay colours in the lower part of the figure. (c) LSFM template to which the brain sample was aligned. (d) Example of the registration performed for one of the larger structures in the alignment between the brain sample and LSFM template. Images are taken from the yellow structure shown in the lower part of (a)-(c).

4.2.2 2D Histology studies

A number of challenges were encountered in the process of aligning 2D histology section to the histology-based template of the AIBS atlas. An experiment was performed to determine what types of background stain were suitable to provide adequate contrast for registration. A Nissl counter stain was found to be most similar to the AIBS atlas template, while a haematoxylin stain also provided much of the contrast information needed (Fig. 4.3). The second challenge was that the tissue sections rarely were cut at exact orthogonal angles, which otherwise are the standard of most atlas plates. If two sections to be aligned are produced at different angles they will not contain the same anatomical information making the registration meaningless. To mitigate this challenge interpolated sections of the 3D AIBS atlas template were manually produced to match the cutting angles of the 2D nissl stained sections prior to registration (Fig. 4.4).

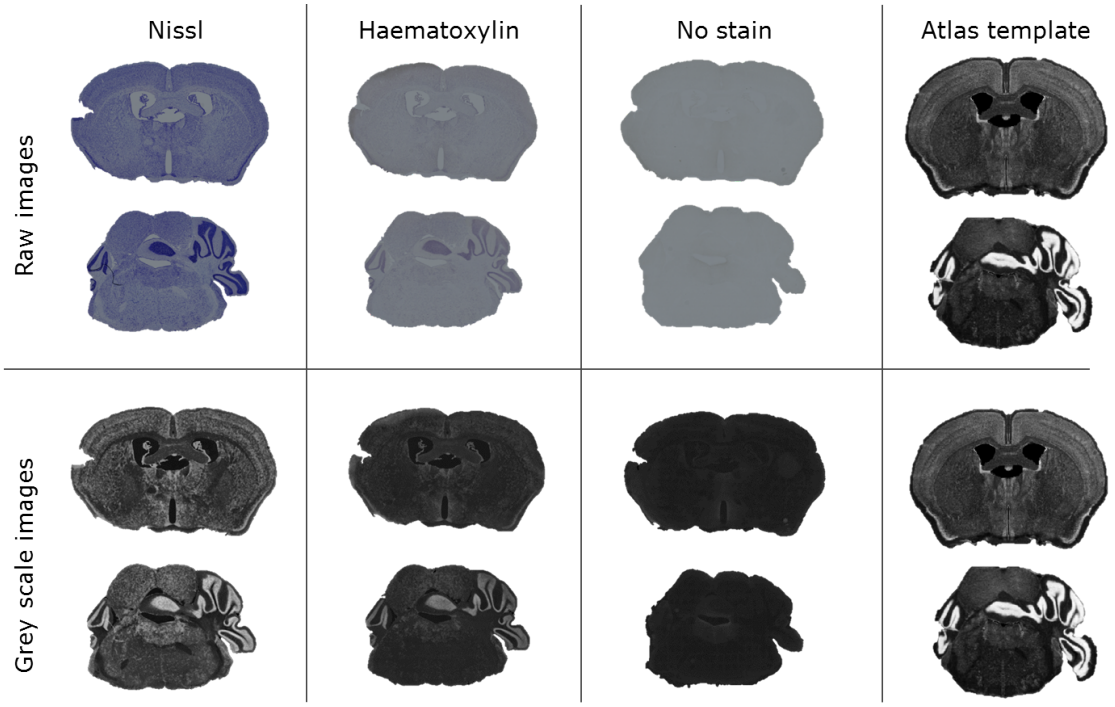

Figure 4.3: Images to compare anatomical contrast information between nissl stain, haematoxylin, or no staining, in relation to the AIBS atlas template. The acquired images were converted to gray scale images to be more comparable to the atlas.

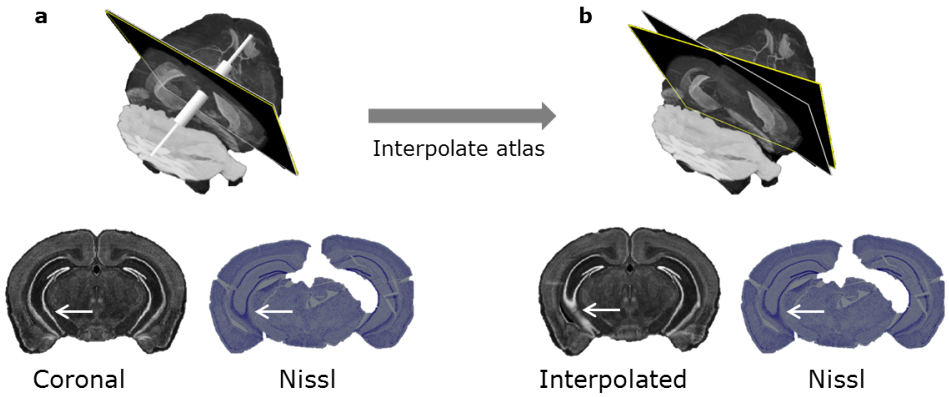

Figure 4.4: (a) Nissl stained section compared to an orthogonal coronal projection from the AIBS histology-based template. The nissl stained section was cut at an non-orthogonal angle seen e.g. by the hippocampus (white arrow). (b) Interpolated atlas projection matching the cutting angle of the Nissl stained section.

4.3 Spectral unmixing

Spectral unmixing algorithms can be divided into two groups; one requires that the sample is sequentially scanned through the frequency range [DBT+01], and the other requires only a few spectrums to be are recorded [MHN+10]. The second type is referred to as blind unmixing. Blind unmixing saves time in acquisition, however it does rely on more assumptions as less data is available. In this work a blind unmixing algorithm was developed as it was not feasible to obtain the full frequency spectrum for every brain sample. Algorithm 1 describes the blind unmixing algorithm developed and used in this phd project to reduce auto-fluorescence in images of fluorescently labelled peptides.

Algorithm 1 compute unmix channel

1. Load auto-fluorescence channel (auto)
2. Load specific channel (spec)
3. Compute histogram of non-zero voxels from auto with 40 bins
4. Pre-allocate result volume (unmix)
5. **For each** histogram bin
6. tempInd = indicies of voxels within histogram bin
7. tempCoeff = median(auto(tempInd)) / median(spec(tempInd))
8. Unmix(tempInd) = spec(tempInd) - (auto(tempInd) ./ tempCoeff)
9. **End**
10. Save unmix channel (unmix)

In line 1 and 2 the acquired LSFM data containing an auto-fluorescence channel and a specific channel is loaded into memory. In line 3 a histogram is computed for the non-zero values of the auto-fluorescence channel. For each of the histogram bins the voxels contained in each bin is selected (line 6) and the median of those voxels is computed for the auto channel and specific channel respectively. A coefficient equal to the ratio between the two median values is computed by division (line 7). The unmix version

of the voxels is computed by subtracting the estimated auto-fluorescence from the acquired specific channel (line 8).

In essence the idea of the algorithm is that the recorded specific channel contains signal from the labelled peptide (wanted signal) as well as auto-fluorescence from the tissue (un-wanted signal). By estimating the auto-fluorescence contribution in the specific channel and subtracting it from the image only the contribution from the labelled peptide is left (Fig 4.5). The auto-fluorescence in the specific channel is estimated as a linear function in each histogram bin. For the algorithm to work it is assumed that the number of voxels with signal from labelled peptides is low (minimal influence on median value computed in each bin), and that the auto-fluorescence of the tissue is more intense at lower wavelengths.

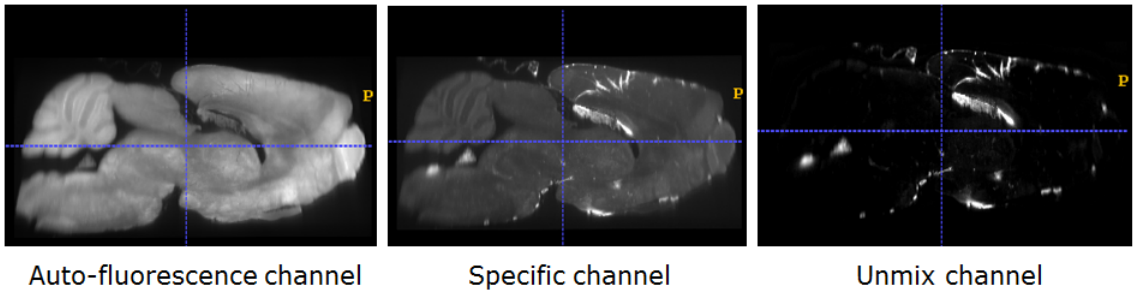

Figure 4.5: Left: Sagital projection of acquired auto-fluorescence channel. Middle: Corresponding sagital projection of the specific channel. Right: Corresponding sagital projection of computed unmix channel.

4.4 Cell segmentation

In the experiments involving whole brain staining a different approach was used to enhance the specific signals used as input for the subsequent statistical analysis. Instead of using the acquired specific channel (or the unmix version) heat maps were computed to provide a compact representation of the acquired whole brain stained signals. The heat maps were based on cell segmentation of positive stained cells. Cell segmentation was performed based on blob filters in combination with morphological operations.

By viewing an image as a function of two variables with the voxel intensity being the function value a blob filter can be constructed based on the eigenvalues of the local hessians at each image point. The Hessian matrix or hessian is a square matrix of second-order partial derivatives, and thus describes the local curvature. The top-hat filter is used to enhance bright objects of interest in a dark background. Top-hat filtering computes the morphological opening of the image based on a structuring element, e.g. a disk, and then subtracts the result from the original image. Essentially, the filters suppress large regions while keeping the small ones as specified by the size of the structuring element.

Algorithm 2 describes the cell segmentation algorithm used prior to constructing the heat maps. The cell segmentation algorithm is applied to each acquired 2D image of the LSFM scan sequence one by one. In line 3, two eigenvalues of the hessian matrix are computed for each voxel in the image of the specific channel. In line 4, a feature is constructed by addition of the eigenvalues to enhance the contrast of blob shaped objects in the image. In line 5, top-hat filtering is used to remove uneven background illumination from the image. For six iterations the sequence of blob filtering and top-hat filtering is repeated to separate larger clusters of cells into individual cells (line 6-10). In line 11, a binary image of the voxels containing positive stained cells is constructed by thresholding. An example showing the cell segmentation algorithm is seen in Figure 4.6. After cell segmentation a heat map was created by summing uniform intensity discs with diameter of 20 μm placed on each voxel representing a cell. These heat maps were later used for visualization and quantification.

Algorithm 2 cell segmentation

```
1. Load auto-fluorescence channel (auto)
2. Load specific channel (spec)
3. [lambda1, lambda2] = blobFilter(spec)
4. feature = lambda1 + lambda2
5. ICell = imtophat(imcomplement(feature))
6. For i=1:6
7.     [lambda1, lambda2] = blobFilter(ICell)
8.     tempFeature = lambda1 + lambda2
9.     ICell = imtophat(imcomplement(tempFeature))
10. End
11. ICellFinal = ICell > threshold
```

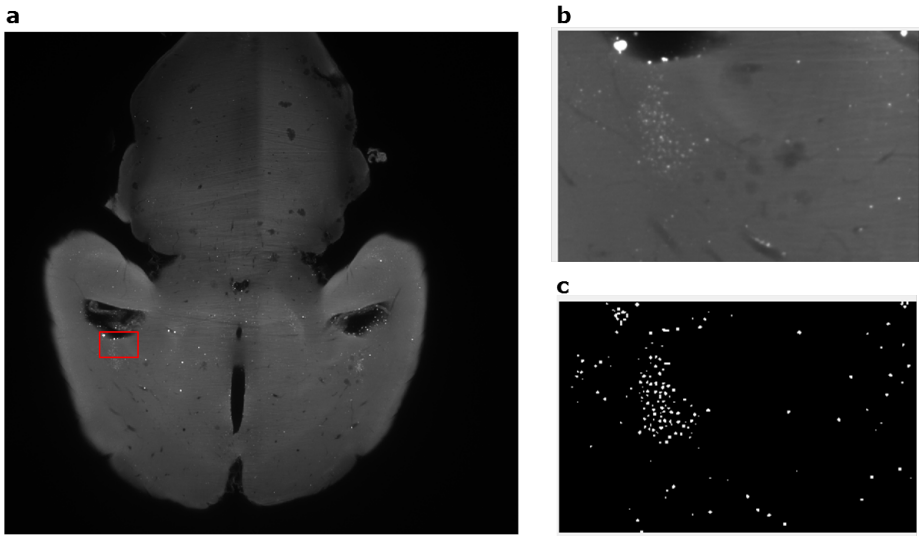

Figure 4.6: (a) Raw image of whole brain stained sample acquired with LSFM. (b) Higher magnification of the red square in (a). The bright dots are positive stained cells. (c) Result of applying Algorithm 2 to obtain a binary representation of the cells.

4.5 Statistical analysis

In this PhD project the most used statistical analysis was comparison of specific signals within a number of brain regions between different study groups. The specific signals may be unmixed fluorescent signal (labelled peptides), or the signals of generated heat maps (whole brain staining). The aim is to compare the total signal in a brain region between different study groups e.g. animals treated with a pharmaceutical compound compared to vehicle. If one think that the mean total signal in a brain region between treatment and vehicle are equal this may be stated as:

$$H_0 : \mu_1 = \mu_2$$
$$H_1 : \mu_1 \neq \mu_2$$

where μ_1 is the mean total signal in the brain region of treated animals and μ_2 is the mean total signal in the brain region of vehicle injected animals. $H0$ is called the null hypothesis and H1 is called the alternative hypothesis. In this example the alternative hypothesis is two-sided because it would be true if either mean value is larger than the other. The hypothesis is tested by computing an appropriate test statistic to either reject or fail to reject the null hypothesis. When testing the hypothesis, two types of errors may be committed:

$$\alpha = P(\text{type I error}) = P(\text{reject } H_0 \mid H_0 \text{ is true})$$
$$\beta = P(\text{type II error}) = P(\text{fail to reject } H_0 \mid H_0 \text{ is false})$$

where α is the probability of rejecting the null hypothesis when it is true, and β is the probability of not rejecting the null hypothesis when it is false. When testing the hypothesis, α, also called the significance level, is normally specified. In this PhD project the two-sample t-test [Mon17] has been used for hypothesis testing. With this test it was assumed that the samples originated from two independent normal distributions with equal variance.

In the studies presented in this PhD project a digital brain atlas was used in combination with image registration to automatically extract the total specific signal in a range of brain regions, leading to multiple t-tests. A way to control the error rate under multiple testing is the concept of false discovery rate (FDR) [BH95]. When multiple tests are performed the goal is to determine a subset of brain regions where the differences seem substantial enough to pursue for further testing. If this subset of brain regions is referred to as discoveries, FDR allows the researcher to tolerate a certain number of tests to be incorrectly discovered. The FDR-controlling procedure introduced by Benjamin and Hochberg [BH95] can be described as follows: Consider testing N hypotheses, $H_1, H_2, ..., H_N$ based on their corresponding p-values, $p_1, p_2, ..., p_N$. Allow a fraction q of discoveries to be false. Sort the p-values in ascending order, $p_{(1)} \leq p_{(2)} \leq ... \leq p_{(N)}$ and denote $H_{(i)}$ the hypothesis corresponding to $p_{(i)}$. Let k be the largest i for which $p_{(i)} \leq i/N \cdot q$. Then reject all $H_{(i)}, i = 1, 2, ..., k$. In this PhD work the FDR procedure was used to control for multiple testing.

4.6 Active appearance models

Activate appearance models (AAMs) were in Paper E investigated as an alternative segmentation strategy for LSFM images. AAMs can be used to segment shapes in images [CET01]. The idea is to construct models of the shapes of interest based on manual annotated training images, and to use these models to segment the shapes in novel images. The motivation is to achieve robust segmentation by using the trained AAMs to constrain segmentation solutions to be valid examples of the class of images and shapes being modeled. The AAM is constructed to model the shape variation and texture variation [CET01]. By texture is meant the pattern of intensities across an image patch. To construct the model a set of images with corresponding landmarks is required. In this PhD work a model was constructed of five brain region shapes (VL, DG1, DG2, ZI, and SPVC). Four to six corresponding landmarks were manually annotated on similar coronal sections extracted from acquired LSFM data (Fig. 4.7a). Each shape was equidistantly up-sampled to consists of 40 landmarks per shape, and normalized by the generalized procrustes analysis (GPA) [DM98]. A shape variability model was constructed based on the eigenvectors of the Nd x Nd shape covariance matrix, where d is the number of image dimensions, and N is the number of landmarks used to represent each shape (Fig. 4.7b). The texture variability model was similarly constructed based on eigenvectors of the Kd x Kd texture covariance matrix, with K equal to the number of intensities sampled from each training example. To make the model robust despite of inhomogeneous illumination seen with LSFM acquisition of large tissue samples the texture was modeled using the regularized Normalized Gradient Field (rNGF) [HM06] instead of the original pixel intensities. The final AAM was constructed by concatenating the parameters of the individual shape and texture models and performing an additional eigen decomposition. Figure 4.7c shows an example of using the constructed model to segment the shapes from a novel image not previously seen by the model.

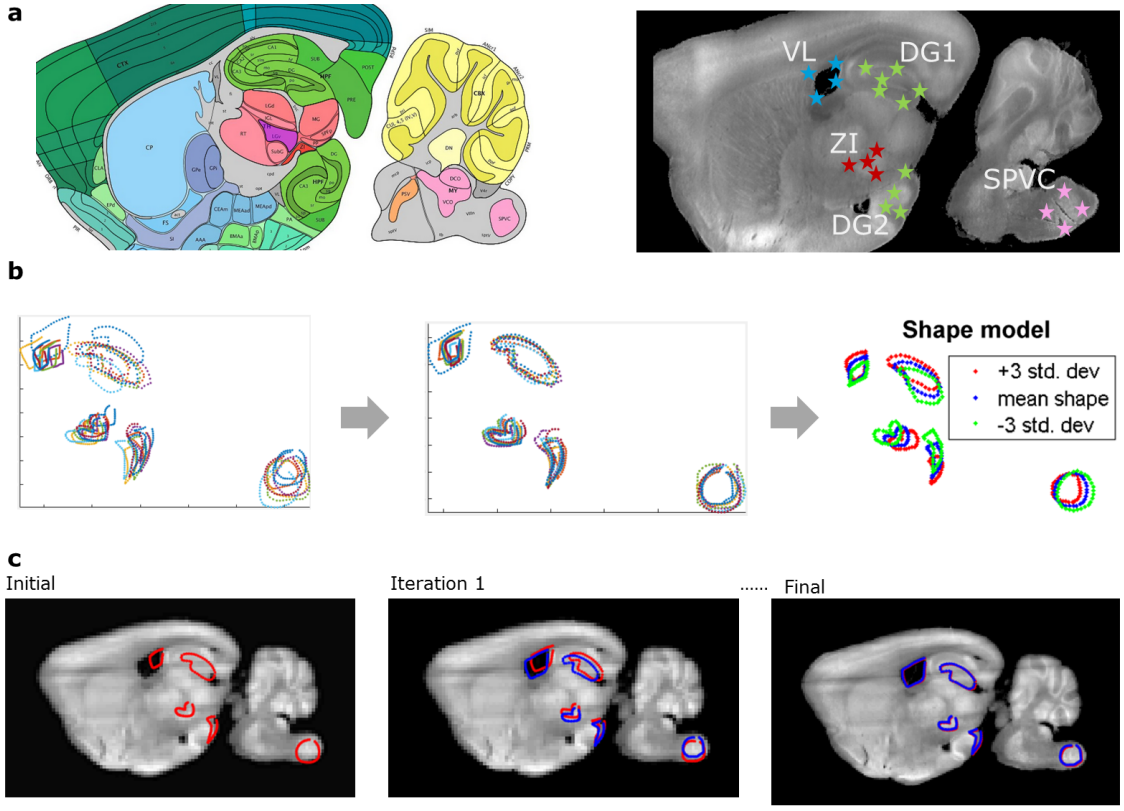

Figure 4.7: (a) Left: Sagtial atlas plate from the AIBS reference atlas. Right: Sagtial projection of LSFM data with labelled brain regions and manually positioned landmarks. (b) Left: Landmarks representing the variation in shape of the five modeled brain regions. Middle: Landmarks aligned by GPA. Right: Constructed shape model. (c) Segmentation using the model. From an initial start guess the model converges toward a solution over a number of iterations.

Part II

Applications

Chapter 5

Data integration

This chapter presents the result obtained by combining the different aspects of the methodology presented in Part I of the thesis to construct an integrated brain atlas enabling automated quantification of brain receptor expression, brain distribution of labelled peptides, brain activation and to some degree brain connectivity. A developed atlas is used to automate analysis of data from the modalities presented in Section 3.1 and 3.2 utilizing the image analysis tools presented in chapter 4 in order to help answer biology questions related to the peptides presented in Section 2.1.1 and 2.1.2. The integrated brain atlas was directly used to obtain the results in Paper A and D, while a less mature implementation of the atlas was used to obtain the results in Paper B and C.

5.1 Integrated brain atlas

The CCFv3 from AIBS (Section 4.1.1) was used as basis for constructing an integrated brain atlas to enable quantification and comparison of data regarding brain access, receptor location, brain activity, and brain connectivity. The atlas implementation combines user data from LSFM and histology sections, as well as connectivity maps downloaded from the AIBS data portal (Fig. 5.1). Brain access and brain distribution was visualized by LSFM imaging of *in vivo*-dosed fluorescently labelled peptides. Brain receptor location was mapped using IHC (in 2D and 3D). Whole brain IHC was used to visualize brain activation. Brain connectivity was added to the atlas based on connectivity maps downloaded from the AIBS data portal. For exploration purposes, all mapped data were imported into a commercially available software program allowing visualization of 3D maximum intensity projections as well as sagittal, horizontal, and coronal 2D projection images. Automatic extraction of statistical measures in brain regions of interest was performed using the annotation model of the CCFv3 from AIBS.

The aim of the atlas is to integrate data sets from different sources. This was enabled by providing data sets with two main components: 1) anatomy information and 2) specific signal information. The anatomy information was used to spatially align the data using image registration as described in Section 4.2, while the specific information helped answer biological questions. Furthermore, collecting all experiment data into a common reference atlas allows the user to gather an anatomical database of information which can be directly compared to parallel and future studies. The following subsections describe strengths and weaknesses of the current atlas implementation.

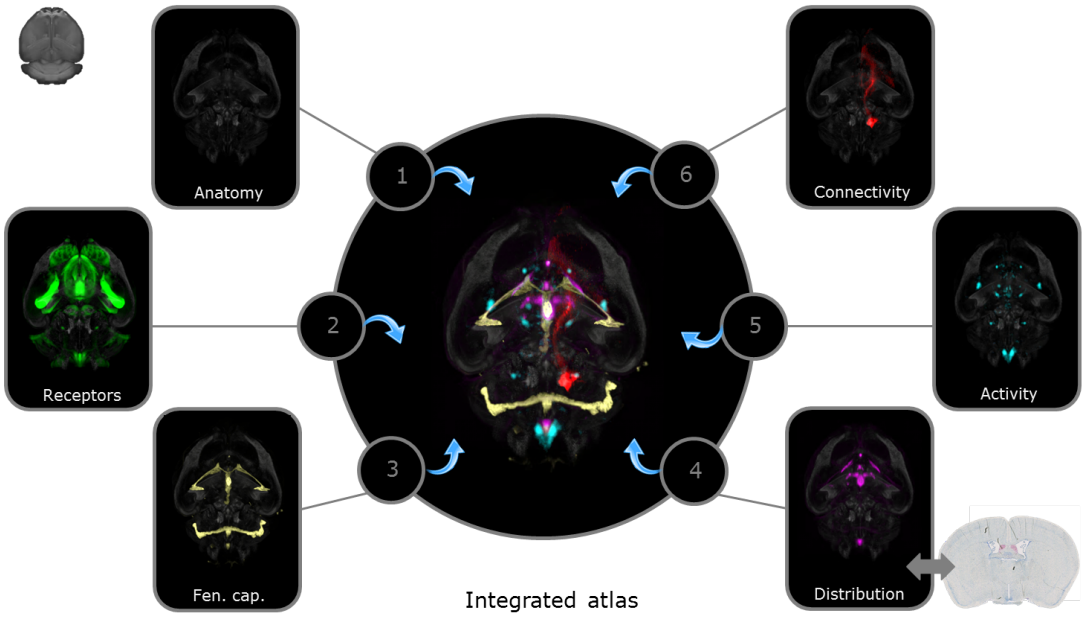

Figure 5.1: (1) Anatomy from auto-fluorescence. (2) Receptor mapping from whole brain IHC, here GLP-1R. (3) Brain access seen by fluorescently labelled antibody against the fenestrated capillaries. (4) Brain distribution of fluorescently labelled peptides, here liraglutide^{VT750}. The 2D histology section is included to indicate that such sections can be aligned to 3D LSFM data. (5) Brain activation from whole brain staining, here c-Fos response to liraglutide treatment. (6) Brain connectivity visualized by connectivity maps downloaded from the AIBS data portal. All data set were mapped to a common reference space to create the integrated brain atlas.

5.1.1 Fluorescently labelled peptides

The use of fluorescently labelled compounds allows the researcher to track the administered compounds directly using LSFM. Such experiments provide information about how the peptides distribute which is important information during development of a pharmaceutical compound. However, one challenge with fluorescently labelled compounds is that the attached fluorephore may change the chemical characteristics of the compound such that e.g. the pharmacokinetic profile is different between the labelled and unlabelled version of the compound. The fluorephore itself may potentially even change the distri-

bution, e.g. allow or restrict access compared to the unlabelled molecule. With fluorescently labelled liraglutide used in Paper A a good correspondance between fluorescently labelled and radioactive (3^{H}) labelled liraglutide in terms of brain access and distribution has previously been showed (unpublished data). Fluorescently labelled liraglutide also has comparable biological effects regarding body weight loss and appetite regulation in mice (data not shown).

5.1.2 Whole brain IHC

Whole brain IHC was utilized in this thesis to visualize receptor localization and brain activation markers. The method may however be used to study any antigen with an available antibody. One of the technical challenges with larger tissue samples such as a whole mouse brain is tissue penetration by the antibody. Ideally the availability of the antibody should be uniform through the tissue sample, however in many cases more antibody will be available near the edges of the sample and less antibody available in the deeper parts of the sample. This leads to a bias in the image intensities when the tissue samples are imaged with LSFM. In this thesis quantification of whole brain IHC stained samples was performed by first performing a segmentation of positively stained cells and then constructing heat maps from the resulting binary representation. In this way the effects of the non-uniform antibody penetration is minimized in the quantification. On the other hand, the difference in intensity of the positively stained cells will in some cases also provide relevant biological information which is currently not reflected in the performed quantification.

5.1.3 Connectivity maps

The ability to automatically search the publicly available connectivity maps from AIBS based on acquired LSFM data provides an opportunity to gain a more comprehensive understanding of the acquired data. In this thesis the connectivity maps were used to investigate secondary brain activation seen following liraglutide treatment. The challenge is that although more than 2000 connectivity maps are available this is still only a limited subset of the full brain connectome. Updates with more connectivity maps are regularly made available on the AIBS website and by adding these the tool will continue to gain value. A similar resource available from the AIBS website is gene expression data of approximately 20.000 genes in the mouse brain based on ISH. Going forward these could also be downloaded and automatically be compared to LSFM data in a similar way as the connectivity maps. It should be noted that these types of analyses are hypotheses generating tools; hence follow up experiments should be performed to validate findings.

5.1.4 2D sections

The ability to directly compare 3D LSFM data with 2D histology data allows the researcher to gain a broader understanding of the data. A case where this method is useful is regarding data from ISH. Whole brain ISH is not commonly used so to directly compare LSFM data with ISH data a tool like

the one developed in this thesis is needed. As described in Section 4.2.2 the cutting of sections are often not orthogonal so interpolated atlas plates are needed for correct registration. In the current implementation this interpolation is performed by the user which lead to operator bias. To avoid this bias automated construction of an interpolated atlas section is needed, or alternatively a direct method for registration between a 2D section and the 3D atlas.

5.1.5 Registration quality

The usefulness of the developed brain atlas largely depends on the registration quality. All brain samples are *ex vivo* samples which lead to more difficult registrations compared to e.g. *in vivo* data where the brain still sits in the skull. The process of removing the brain often leads to mechanical damage to the tissue seen as small or large tissue cracks in the acquired data. Furthermore, as described in Section 4.2.1 the applied tissue preparation protocol for LSFM causes non-uniform tissue deformation with different parts of the brain shrinking more than others. These challenges made it difficult to select proper regularization parameters for the registrations. To mitigate these problems a registration model was introduced where larger individual parts of the brain was registered alone and combined to create the final result. Especially the computation of a different affine deformation for each of the larger brain structures improved the segmentation quality. The registration quality was tested as part of the work in Paper A. Based on manually positioned landmarks the average error was around 5 voxels corresponding to 100 μm. Going forward, new tissue preparation protocols such as e.g. [PCQ+16] may led to less tissue deformation and improved alignment to the digital atlas.

Chapter 6

GLP-1

This chapter presents how the registration and segmentation methods presented in Chapter 4 were applied to investigate effects of GLP-1RAs related to appetite regulation. The GLP-1R brain expression was mapped, as well as the brain distribution following peripheral administration of the GLP-1RAs liraglutide and exendin-4. Brain activation in response to liraglutide treatment was also investigated, and connectivity maps from AIBS were used to infer information on observed secondary activation. The results presented here are summaries of the results obtained in Papers A, B, and C.

6.1 GLP-1R mapping

In paper B the aim was to show the detailed distribution of GLP-1R immunoreactivity in combination with mapping of GLP-1R mRNA by non-radioactive ISH. This was done in part to compare the results obtained using the different staining approaches, and also to construct a set of anatomical reference plates to summarize the GLP-1R distribution through the mouse brain.

Image segmentation of the acquired IHC and ISH slide scanner images were performed using a multinomial regression classifier based on r,g,b image features. Prior to segmentation each IHC/ISH image pair was registered to a digital atlas plate obtained from the Allen mouse brain reference model (Fig 6.1c). In some regions mRNA and protein expression co-exists (Fig. 6.1d-e), but in other regions e.g. only protein expression were seen (Fig. 6.1f-g). The strength of using a specific antibody was emphasized by the ability to detect GLP-1R protein in regions devoid of mRNA and in neuronal projections where expression was not observed previously using a transgenic reporter system [CRH^{+}15]. The GLP-1R was abundantly expressed in numerous brain regions including the septal nucleus, the hypothalamus

and the brain stem. In total 22 atlas plates were constructed showing the localization of the GLP-1R through the mouse brain (Paper B, Fig 2).

Even though 22 sections provide comprehensive information on the GLP-1R distribution the approach of using 2D sections has limitations. As mentioned GLP-1R expression was observed on neural projections, but it is difficult to track axons through a set of sections. Going forward, the use of whole brain IHC staining will be a valuable tool to track these projections and gain and even better understanding of the GLP-1R distribution.

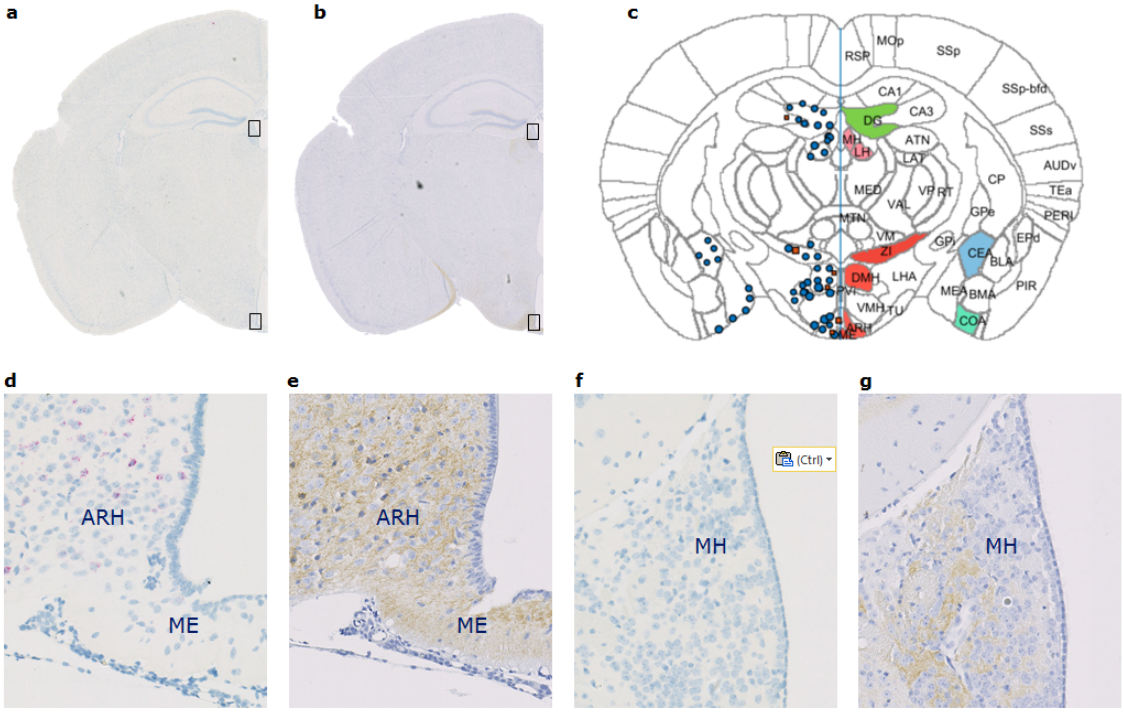

Figure 6.1: (a) Example of ISH image. (b) Example of IHC image. (c) Atlas plate obtained by automatic drawing of markers representing segmented signal following a 2D registration of the images in (a-b) to a digital atlas plate from AIBS. Blue circles correspond to the segmentation of the IHC image, and the red squares correspond to the segmentation of the ISH image. Brain regions with either positive IHC or ISH signal is highlighted with a fill color. (d-g) Zoom images shown for black boxes in (a-b).

6.1.1 Brain distribution of GLP-1RAs

As the GLP-1R was shown to be widely distributed throughout the mouse brain and since GLP-1 is also a neurotransmitter produced in hindbrain neurons [TC15], it is of interest to examine which GLP-1Rs are accessible to peripheral injected GLP-1RAs. In paper A the brain distribution of peripheral administered liraglutide^{VT750} was mapped to evaluate which brain regions could potentially be directly activated by the compound. In paper C the distribution of another GLP-1RA exendin-4 was quantified.

6.1.2 Liraglutide distributes to hypothalamus, hindbrain and cerebral nuclei

Fluorescently labelled liraglutide was injected *in vivo* and mouse brains were removed after six hours and compared to brains from vehicle injected animals. Using the nomenclature of the AIBS mouse brain atlas, liraglutide^{VT750} was significantly detected in CVOs such as AP and OV, as well as in regions shielded by the BBB such as ARH and paraventricular hypothalamic nucleus (PVH). Liraglutide^{VT750} was also observed in chpl, exemplified by the plexus located in V4 and VL (Fig. 6.2a). An average liraglutide^{VT750} distribution signal was computed and imported into the integrated brain atlas for visualization (Fig. 6.2b). The signal in the chpl was not thought relevant as no GLP-1R was present on these cells. By comparing to the broad distribution of GLP-1R this study showed that liraglutide targets a subset of receptors localized in the hypotalamus, hindbrain and cerebral nuclei.

Fluorescently labelled exendin-4 was likewise injected *in vivo* and the brains were removed after two hours and compared to vehicle injected brains. Using the nomenclature of the AIBS mouse brain atlas, exendin-4^{VT750} was significantly detected in AP, Nucleus of the solitary tract (NTS), ME, ARH, Periventricular hypothalamic nucleus, posterior part (PVp), OV, Septofimbrial nucleus (SF), and Lateral septal nucleus, caudal part (LSc). Overall, the distribution of exendin-4^{VT750} was similar to that of liraglutide^{VT750}. However, differences was observed mainly in the LSc were exendin-4^{VT750} signal was strong, but no liraglutide^{VT750} signal was seen. Conversely, liraglutide^{VT750} signal was observed in the PVH, were almost no exendin-4^{VT750} signal was observed. This is interesting as both compounds are GLP-1RAs, but still show a different brain distribution.

As the GLP-1RAs have different pharmacokinetic profiles and as the distribution studies only consists of a single time point each one could speculate that the observed difference in distribution is merely due to the difference in plasma concentrations of the compounds at those time points. However, this is not the case as multiple studies with different time points have been performed during the PhD project (data not shown). The liraglutide^{VT750} distribution has e.g. been evaluated after 10 minutes, 6 hours, 24 hours, and 48 hours without showing a signal in LSc. A dose dependency study of liraglutide^{VT750} has also been conducted which led to the conclusion that the distribution does not change as function of dose concentration, i.e. a higher concentrations will not lead to signal in new brain regions (data not shown). The distribution differences between the GLP1-RA compounds are thus probably due to their different chemical structures.

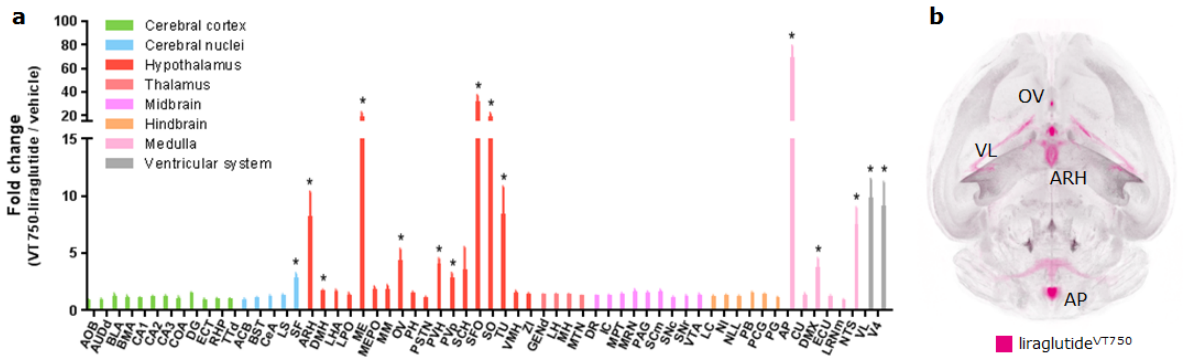

Figure 6.2: (a) Bar graph showing the mean fold change and standard deviation (SD) of the total fluorescence signal in selected brain regions comparing liraglutide^{VT750} and vehicle (n=5). An asterisk marks significant difference between treatments when analyzed in individual brain regions using a false discovery rate value of 5% to correct for multiple comparisons. Note the split y-axis when interpreting results and SD. See Supplementary Table 1 for full brain region names. (b) Maximum intensity projection of the average liraglutide^{VT750} signal computed from the individual brains in the study group (n=5).

6.1.3 The liraglutide distribution is GLP-1R dependent

In Paper A the ISH platform RNAscope [WFS^{+}12], [AZM^{+}16] was used to map the glp-1r mRNA location in a number of coronal slides throughout the C57BL/6J mouse brain. A heat map was computed from the ISH section to represent the glp-1r positive cells, and this heat map was aligned to the integrated brain atlas, which enabled direct visual comparison with the average liraglutide^{VT750} distribution. An example of a mapped glp-1r ISH heat map compared to the corresponding anatomical location in the average liraglutide^{VT750} distribution signal is seen in Paper A, Fig. 6. Overlap was seen in Supraoptic nucleus (SO) and SFO, while a liraglutide^{VT750} signal was also observed in the chpl located in VL where no receptor signal was present. Overall, all regions with liraglutide^{VT750} distribution also showed glp-1r mRNA except ME and chpl in the ventricular system. We know however from Paper B that GLP-1R is present in ME so this region may be added to the list of regions with a possible direct activation from liraglutide. The GLP-1R dependence was further validated as liraglutide^{VT750} signal was lost in *glp-1r*$^{-/-}$ mice except for signal in chpl.

6.2 Brain activation in response to liraglutide treatment

Knowing the GLP-1R brain distribution and the subset of these GLP-1Rs targeted by liraglutide^{VT750}, the next step in Paper A was to investigate possible change in brain activation following liraglutide treatment. The brain activation pattern was compared to the average distribution of liraglutide^{VT750} and connectivity maps from AIBS to delineate direct versus secondary activation.

6.2.1 Liraglutide treatments leads to activation in brain regions related to food intake

C57BL/6J mice were dosed subcutaneously with liraglutide, and the c-Fos response was compared to vehicle dosed controls four hours after treatment. The most prominent c-Fos increase following liraglutide injection was seen in Bed nuclei of the stria terminalis (BST), Paraventricular nucleus of the thalamus (PVT), Central amygdala nucleus (CEA), Parabrachial nucleus (PB), and NTS (Fig. 6.3a). Heat maps were constructed for each individual brain sample based on the number of c-Fos positive cells and aligned to the integrated brain atlas (Fig. 6.3b). The heat maps were used to quantify the differences between liraglutide and vehicle dosed animals in select brain regions (Fig. 6.3c). Brain activation in PB, CEA, and BST has previously been described to be related to lowering of food intake through a pathway involved in meal termination [CSZP13], [CHAA14].

In the interpretation of the study results it is again important to note that the activation is only evaluated at a single time point after treatment. A similar brain activation profile was however seen after chronic dosing of liraglutide (data not shown). Also, c-Fos is an activation marker, but direct effects of liraglutide may also cause inhibition, e.g. lead to decreased brain activity in certain regions. In this study we were not able to identify brain regions where liraglutide treated animals had decreased brain activation compared to vehicle treated animals. An interesting study would be to perform the same experiment in hungry mice to explore if liraglutide perhaps could lower activity in brain regions which promote food seeking an increased appetite. A final consideration is that brain activity may occur without detection by c-Fos. Thus one can not conclude that no activation occurs in e.g. cerebral nuclei just because no c-Fos increase was seen. It will be interesting to investigate more activation markers going forward.

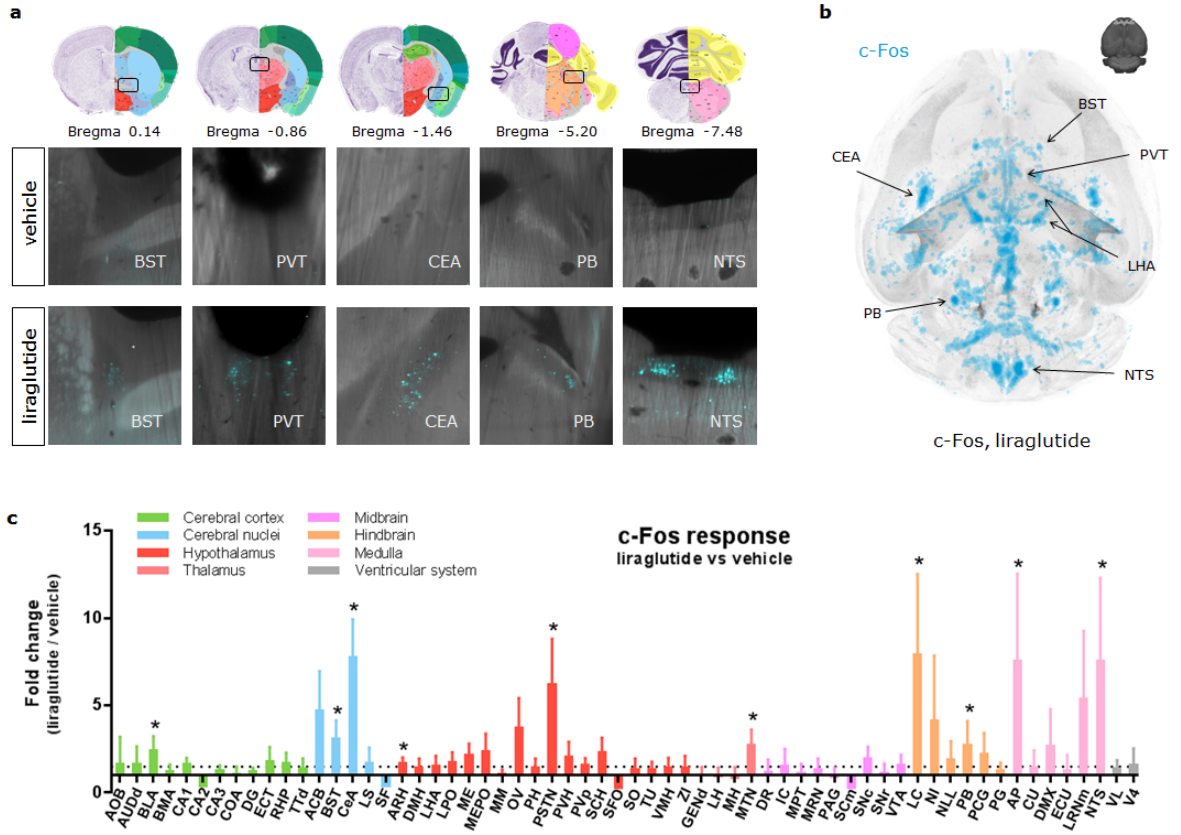

Figure 6.3: (a) Example images of c-Fos response in liraglutide vs vehicle dosed mice. Bregma coordinates denote the anatomical location. (b) c-Fos heat map computed from one liraglutide injected mouse. (c) Bar graph showing the mean fold change and SD of total c-Fos heat map signal in selected brain regions comparing liraglutide and vehicle dosed animals. An asterisk marks significant difference between treatments when analyzed in individual brain regions using a false discovery rate value of 20% to correct for multiple comparisons.

6.2.2 Brain activation appears to be a combination of direct and secondary activation

To investigate whether the observed c-Fos response could be direct effects of liraglutide interaction with GLP-1R a visual comparison of the liraglutide specific c-Fos increase with the liraglutide^{VT750} distribution from Fig. 6.2b was performed. The c-Fos increase was computed by subtraction of the average c-Fos signal in the vehicle group from the average signal in the liraglutide treated group (Fig. 6.4a). Some overlap was seen between the liraglutide^{VT750} distribution and the c-Fos increase (Fig. 6.4b), mainly in the hindbrain indicating possible direct activation from liraglutide in this area. However, the majority of c-Fos increase was seen in regions not overlapping with the liraglutide^{VT750} distribution, indicating secondary activation.

To investigate the observed secondary brain activation, the brain connectivity maps from AIBS were automatically ranked in regards to the similarity with the c-Fos increase. Projections from the lateral PB were seen in four of the ten most overlapping connectivity maps compared to the liraglutide specific c-Fos increase. As liraglutide^{VT750} showed no significant access in the PB, this suggests a role of the PB as a relay station of input from other targeted brain regions. Glutamatergic (slc17a6-IRES-Cre) projections from the lateral PB (4th most overlapping connectivity map) were imported into the integrated brain atlas to visualize how these neurons could be part of the secondary c-Fos response following liraglutide treatment (Fig 6.4c). This parabrachial pathway has in recent literature been described as a general circuit causing anorexia [CSZP13], [CHAA14], [CBSP16] and from the results also appears to be involved in the brain activation from liraglutide treatment. In connection with this literature it is described how the PB is activated from the AP/NTS which also fits well with observations about possible direct activation from liraglutide in these regions (Fig. 6.4b).

However, it must be noted that these analyses of overlaying the brain activity signal with the liraglutide^{VT750} distribution signals and connectivity maps from AIBS provides hypotheses and not actual confirmation. To further test the generated hypothesis of direct activation in the hindbrain, one could e.g. co-stain for c-Fos and GLP-1R in sections including AP/NTS of liraglutide treated animals. To test the hypothesis of secondary activation relayed by the PB one could e.g. co-stain for c-Fos and cgrp which is a marker of a subpopulation of neurons in the PB described to be involved in meal termination [CBSP16].

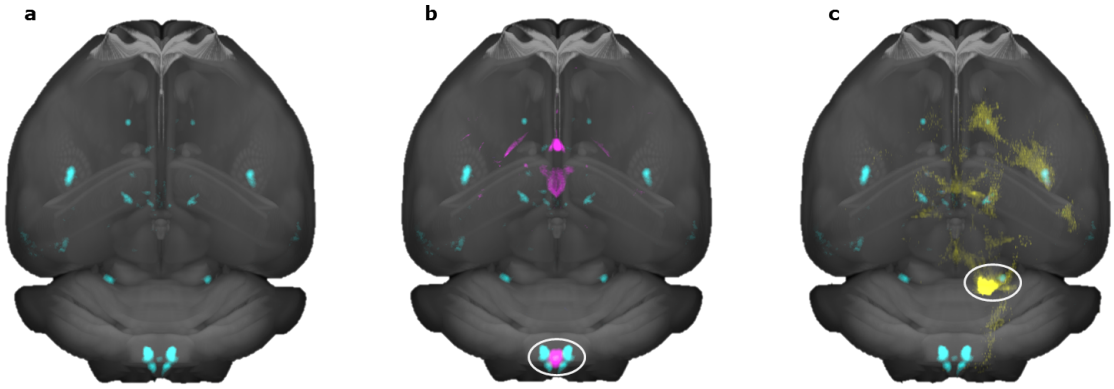

Figure 6.4: (a) Maximum intensity projection of the average c-Fos increase following liraglutide treatment (blue). Signals are overlaid onto the CCFv3 template from AIBS. (b) Maximum intensity projection of the average liraglutide^{VT750} distribution (purple) overlaid with the average c-Fos increase following liraglutide treatment (blue). (c) Maximum intensity projection of downloaded glutamatergic projections from PB (yellow) overlaid with the average c-Fos increase following liraglutide treatment (blue).

Chapter 7

Leptin

This chapter presents how the registration and segmentation methods presented in Chapter 4 were applied to investigate brain activation in response to leptin treatment. LepRb was mapped to select a subset of brain regions for further analysis of the brain response to exogenous leptin. Brain activation in response to leptin treatment was mapped at different time points after treatment and in different animal models. The results presented here are summaries of the results obtained in Paper D.

7.1 Mapping of LepRb

In paper D the aim of the receptor mapping was to detect brain regions where exogenous leptin may have a direct effect through LepRb. A genetic model previously utilized by Patterson et al. [PLJM11] was here also used to map the receptor localization. Three $\text{LepRb}^{\text{EGFP}}$ mouse brains were scanned using LSFM to image the whole brain in 3D. As previously described the LepRb distribution was broad and scattered throughout the mouse brain. High concentrations of receptor were seen in cortical regions, hypothalamic regions, midbrain regions and hindbrain regions. Cortical regions included Dorsal auditory area (AUDd), Supplemental somatosensory area (SSs), and Ectorhinal area (ECT). Hypothalamic regions included ARH, DMH, and Lateral hypothalamic area (LHA). Midbrain regions included dorsal nucleus raphe (DR), Periaqueductal gray (PAG), and Ventral tegmental area (VTA). Hindbrain regions included PB, NTS, and Dorsal motor nucleus of the vagus nerve (DMX). Based on receptor expression in these brain regions leptin potentially has the ability to directly affect both homeostatic feeding, meal generated signals, and reward driven feeding [MMLL09].

The LepRb^{EGFP} mouse model expresses enhanced green fluorescent protein (EGFP) under a LepRb promoter which means that fluorescence signal is observed in cells that express mRNA coding for LepRb. These signals are restricted to the cell soma which means that LepRb potentially could be expressed on axonal projections (as were seen with GLP-1R) or in synaptic cliffs without detection in this setup. A specific antibody against LepRb is needed to investigate this concern. However, no apparent pStat3 signal was observed in the later experiments in regions not showing LepRb expression in the LepRb^{EGFP} model.

7.2 pStat3 activation in response to leptin treatment

In paper D the aim was to investigate why peripheral leptin treatment is not an effective obesity treatment despite that leptin promotes weight loss in non-obese individuals [HBBW^{+}97]. In this PhD work, two main experiments were performed to: 1) evaluate the time course of the brain activation following a peripheral leptin injection, and 2) evaluate the difference in brain activation between lean and obese mice. Brain activation was evaluated based on pStat3 as this is a commonly used marker for direct activation of the LepRb [MFB04].

Following peripheral administration of leptin, animals were euthanized after 10 min., 30 min, 60 min, 120 min, and 240 min. The brains were extracted and imaged using LSFM after whole brain IHC staining for pStat3 (Fig. 7.1a). Heat maps representing the number of cells positive for pStat3 were created and quantified using the integrated brain atlas. It was observed that the pStat3 response peaked at different time points in different brain regions, although most activation peaked between 60 min. and 120 min. as e.g. seen in Ventromedial hypothalamic nucleus (VMH) (Fig. 7.1b).

Next, the potential differences in brain activation to exogenous leptin between lean mice and obese mice were investigated. Diet induced obese (DIO) mice were included as these mice mimic the human obesity epidemic partly driven by easy access to highly palatable foods which leads to leptin tolerance or resistance [BM09]. Brain activation was evaluated 60 minutes after subcutaneous leptin injection. The lean mice showed strong brain activation after leptin injection and low baseline activation with vehicle injection. The activation was most prominent in the hypothalamic regions. The DIO mice showed an attenuated response to leptin and higher baseline activation compared to lean mice. Quantification of the pStat3 response in eight hypothalamic regions showed a large dynamic in the lean model with fold changes ranging from 6.35 (ARH) to 285.06 (LHA) between leptin and vehicle treated animals (Fig. 7.2a). This increase in pStat3 activation was not seen in the DIO model where the largest fold change was modest 2.66 (PH) (Fig. 7.2b). The study showed that exogenous leptin provides little additional information to the brain compared to baseline conditions in the DIO mouse and this could be a hint to why leptin is not an effective obesity treatment.

The analysis was focused on the hypothalamic regions as this was the region with the strongest pStat3

signals. However, the same picture with a lowered dynamic in DIO model was also observed in the hindbrain, primarily seen in DMX and NTS. Little to no pStat3 signal was observed in areas of the limbic system such as in VTA or Nucleus accumbens (ACB) in either of the mouse models. Going forward, it could be interesting to explore secondary brain activation following leptin treatment in lean and DIO mice as this might provide further knowledge about leptin resistance.

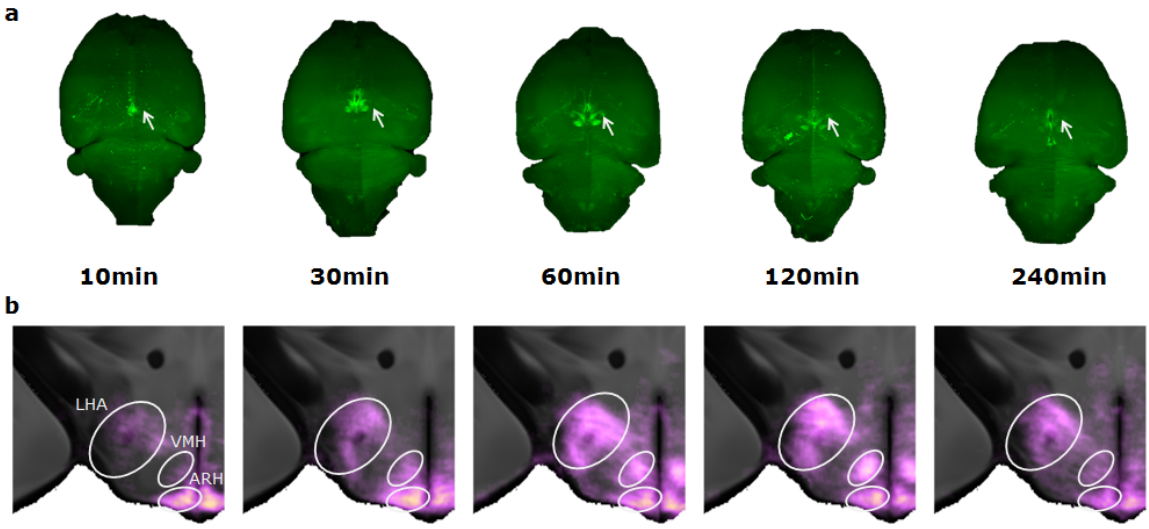

Figure 7.1: a) Examples of whole brain pStat3 stained brains from animals euthanized at different time points after peripheral leptin injection. The strongest activation signal was seen in the hypothalamus (white arrow). (b) Coronal sections of average heat maps generated for each time point. Heat maps are overlaid onto the CCFv3 template from AIBS. It is seen that the activation in general is strongest between 60 min. and 120 min.

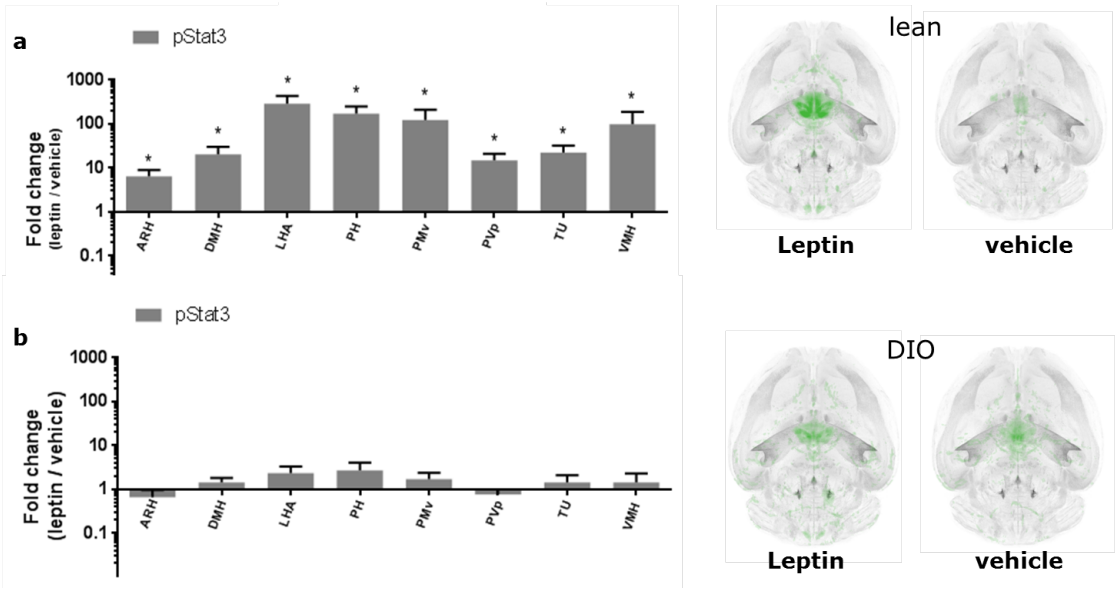

Figure 7.2: (a) Ratio of pStat3 activation between leptin and vehicle treated lean mice. All brain regions showed significant activation following leptin treatment using multiple comparisons with FDR correction of 5%. Note the log scale when interpreting standard deviations. (b) Ratio of pStat3 activation between leptin and vehicle treated DIO mice. No brain regions showed a significant activation increase from leptin treatment.

Chapter 8

User interface

This chapter describes how the integrated brain atlas and the most used algorithms were implemented at Novo Nordisk A/S to enable other researchers to use the developed analysis tools. This was an important milestone as this is an industrial PhD project. Thus researchers at the company should be able to continue using the automated quantification of LSFM data after the PhD projected has ended.

The developed algorithms were linked to Imaris which is a commercial software for 3D image viewing used at Novo Nordisk. The developed algorithms are made available through the image analysis menu located in the software. The integrated brain atlas is the backbone of the algorithms and all data sets aligned to the atlas are saved as open source nifti files for storage. The nifti files also allow the user to import specific brain signals from different experiments into the same Imaris file for explorative work and visualization. User input to the algorithms, as well as output such as extracted variables for statistical analysis, are exported to Microsoft excel files.

8.1 Developed scripts

Two main analysis pipelines were developed during the PhD project. The first pipeline enables automated quantification of LSFM data to analyze *in vivo* injected fluorescently labelled peptides in the whole brain. Data is acquired in 10.32 um isotropic resolution with one channel containing anatomical information from auto-fluorescence and another channel containing specific information from the labelled peptide. To analyze the data the user fills out an excel template with information on the location of the acquired image files, which study groups the individual brains belong to, and the desired location for result files to be saved. The algorithm will then construct an unmix version (Section 4.3) of the spe-

cific channel together with a preprocessed version of the auto-fluorescence channel. The preprocessed auto-florescence channel is registered to the LSFM template of the integrated brain atlas and the unmix channel is transformed to the atlas space using the computed parameters. Once image data of all brain samples from the experiment are aligned to the atlas space, average signals representing the different study groups of the experiment are constructed by averaging the aligned unmix channels. These average signals may later be imported into the same Imaris file to visually compare the experiment groups.

The second pipeline enables automated quantification of LSFM data from whole brain IHC stained brain samples. Data is acquired in 4.06 um isotropic resolution with one channel containing anatomical information from auto-fluorescence and another channel containing specific information from the stained cells. The analysis is the same as for the labelled peptides, however instead of a representation of the specific signal by an unmix channel, in this case the specific signal is represented by a heat map constructed based on the number of positive stained cells (Section 4.4). Once all heat maps representing the samples from the experiment are aligned to the atlas space, average signals representing the different study groups of the experiment are constructed by averaging the constructed heat maps. These average signals can again be imported into an Imaris file to ease visual comparison of the experiment groups.

Table 8.1 provides an overview of the implemented scripts. As all aligned brain samples can be imported into any Imaris file it is easy to compare information from different studies and study types. Figure 8.1 shows an example of aligned nifti files from different experiment loaded into the same Imaris file. Once imported to Imaris, 2D projections, maximum intensity projections, and movies can be constructed.

Plugin	**Study type**	**Purpose**	**Output**
CCFv3	Labelled peptide	Visualize and quantify labelled peptides	Individual unmix channels (nifti). Average brain (nifti). ROI statistics (excel).
iDISCO	Whole brain staining	Visualize and quantify whole brain stained samples	Individual heat maps (nifti). Average brain (nifti). ROI statistics (excel).
Import nifti	Labelled peptides + whole brain staining	Import brain signals to the integrated brain atlas for easy visual comparison	

Table 8.1: Developed scripts made accessible through the commercial Imaris software.

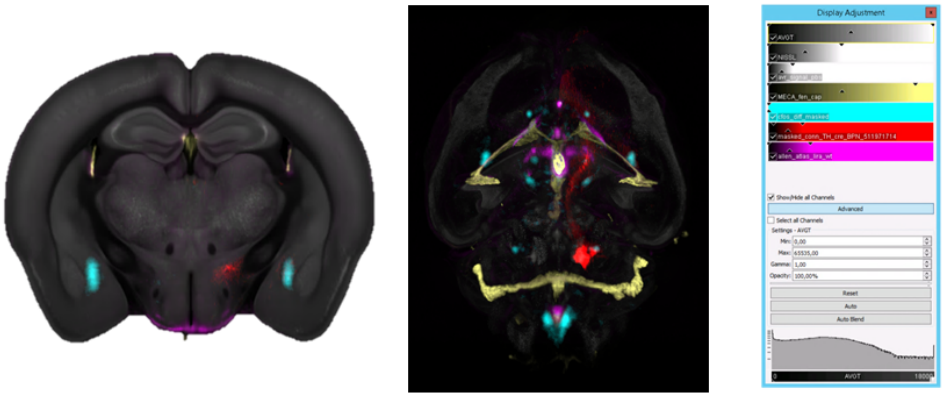

Figure 8.1: Left: Coronal projection of different data sets all aligned and imported into the same Imaris file for easy visual comparisons. The signals are overlaid onto the CCFv3 template from AIBS. Middle: Same data set now visualized as a 3D maximum intensity projection. Right: Screenshot from the Imaris user interface showing the different channels imported into the Imaris file. The user can tick on and off the different channels as well as adjusting color maps.

8.2 Number of analyzed brain samples

To highlight the usage of the developed scripts a count was performed regarding the number of individual brain samples analyzed each month during the last year of the PhD project (Fig. 8.2). The brain samples analyzed came from a mix of studies related to this PhD project as well as different research projects at Novo Nordisk. The total number of quantified brains within the last year was 466. The largest number of brains quantified in a single month was 80 which demonstrate the need for an automated analysis approach.

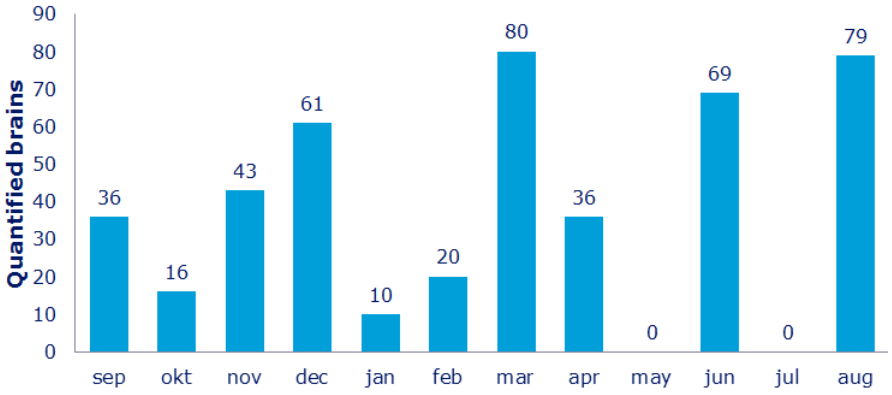

Figure 8.2: Number of brains analyzed within the last year of the phd project using the developed atlas approach for automated quantification.

Chapter 9

Active appearance segmentation

This chapter describes how the AAMs presented in Section 4.6 was used to segment selected brain regions in 2D sagital projection images from LSFM data. An AAM constructed based on rNGF was evaluated in terms of robustness to common LSFM artefacts. The results presented here are summaries of the results obtained in Paper E.

9.1 Segmentation quality

The aim of paper E was to evaluate the influence of common LSFM artifacts on the segmentation quality of a novel approach to constructing an AAM with the texture model based on rNGF instead of the classical SSD. LSFM systems are prone to different artifacts such as inhomogeneous illumination and possible blurry images. The inhomogeneous illumination may arise from suboptimal clearing of tissue samples, or from the imperfect characteristics of the generated light sheet especially seen with larger tissue samples. Blurry images may arise when the operator does not adjust the focus of the microscope correctly.

The first experiment investigated the effect of manipulating the images by applying a controlled artificial bias field to mimic slowly varying spatial intensity inhomogeneities. The Dice score [Dic45] was used to evaluate the quality of the segmentation. The overall Dice score of the model as function of the bias field strength was observed to degrade faster with the model based on the SSD similarity measure compared to the model based on rNGF.

The second experiment investigated the AAM model performance using a test set of images with common LSFM imperfections acquired at different times during the Phd work. The test set consisted of eight images where four contained brains with poor tissue clearing and the other four contained brains scanned with a lower quality light sheet arising from poor operator settings. Examples of segmentation results obtained with the rNGF-based AMM and the SSD-based AAM are seen in Fig. 9.1a. The SSD-based model fails to segment the VL in case of the lower quality light sheet. Dice scores of the individual brain structures are seen in Fig. 9.1b. The rNGF-based model results in higher Dice scores and less variance.

Going forward the AAMs could be extended to 3D and potentially be used to segment individual brain regions as a complementary method to the image registration approach. A challenge is the need for manual annotated training data which is a work intensive and difficult task in 3D. Another idea could be to use rNGF as similarity measure during the 3D atlas registrations since the similarity measure in this work showed favorable in the analysis of LSFM images.

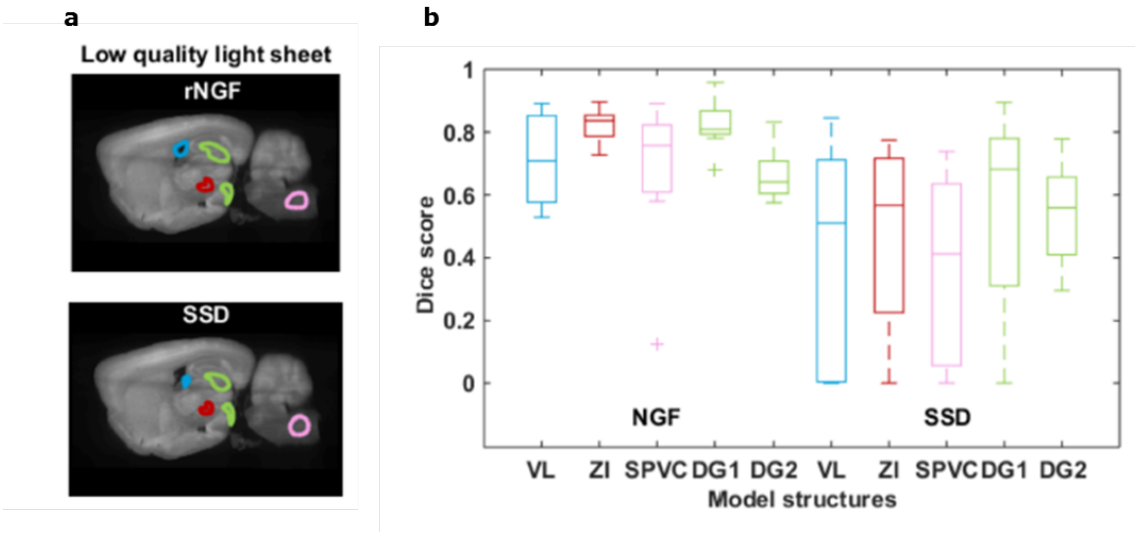

Figure 9.1: (a) Examples of segmentations obtained with rNGF-based model (top) and SSD-based model (bottom row). Images shows a brain recorded with lower quality light sheet. (b) Boxplot of Dice scores of the individual segmented structures. The median is represented as the center line of each box and the edges correspond to the 25th and 75th percentiles.

Chapter 10

Conclusions

The aim of the PhD project was to develop algorithms to enable automated high throughput quantification of whole brain LSFM data. This was accomplished by utilizing image registration to integrate the LSFM data with the CCFv3 digital brain atlas from AIBS. The LSFM system has been used to image distribution of fluorescently labelled peptides as well as brain receptor localization and brain activation in response to treatment with the peptides. During the project the methodology expanded to also include integration of information from user 2D histology sections and brain connectivity maps from AIBS. The developed atlas was used to investigate CNS biology related to GLP-1RAs and leptin.

GLP-1R was mapped in the mouse brain and showed a broad distribution. It was observed that fluorescently labelled liraglutide accessed a subset of these receptors after peripheral administration. Distribution was seen in hindbrain, hypothalamus, and cerebral nuclei. Peripheral administration of liraglutide led to brain activation in regions previously related to decreased food intake. A comparison between the observed brain activation and the distribution of fluorescently labelled liraglutide led to a hypothesis of direct activation by liraglutide in the hindbrain. A comparison between the observed brain activity and connectivity maps from AIBS led to a hypothesis of secondary brain activation relayed by the PB.

LebRb was mapped in the mouse brain and like GLP-1R showed a broad distribution. Brain activation in response to peripheral leptin treatment peaked between 60 minutes and 120 minutes in lean mice. The strongest brain activation was observed in the hypothalamus. Brain activation in response to leptin treatment was compared in lean mice and obese phenotypes. Leptin treatment led to a large increase in brain activation in lean mice compared to baseline, but failed to do so in DIO mice.

Going forward there are many opportunities to further improve the developed integrated brain atlas. Improvements may be achieved regarding both tissue preparation protocols, image acquisition protocols, and developed algorithms. The atlas could further be improved by integrating data from additional sources. One example could be gene expression data from AIBS. By testing additional antibodies with whole brain IHC staining in combination with LSFM it will also be possible to add information about other relevant receptors and activation markers related to brain control of body weight and appetite regulation. Integration and analysis of these data has the opportunity to aid in the development of improved treatment options for people with obesity.

Part III

Contributions

Appendix A

Integrated Brain Atlas for Unbiased Mapping of Nervous System Effects Following Liraglutide Treatment

Integrated Brain Atlas for Unbiased Mapping of Nervous System Effects Following Liraglutide Treatment

Casper Bo Jensen[1,2], Tess Tsai-Hsiu Lu[1], Sanaz Gabery[1], Kasper Marstal[2,4], Tomas Alanentalo[1], Aaron Jeffrey Mercer[3], Anda Cornea[3], Knut Conradsen[2], Jacob Hecksher-Soerensen[1], Anders Bjorholm Dahl[2], Lotte Bjerre Knudsen*[1], Anna Secher[1]

[1]Global Research, Novo Nordisk A/S, Måløv, Denmark;

[2]Image Analysis & Computer Graphics, Department of Applied Mathematics and Computer Science, Technical University of Denmark, Kgs. Lyngby, Denmark;

[3]Global Research, Novo Nordisk A/S, Seattle, USA;

[4]Biomedical Imaging Group Rotterdam (BIGR), Department of Radiology & Medical Informatics, Erasmus Medical Center, Rotterdam, Netherlands;

Light Sheet Fluorescence Microscopy (LSFM) of whole organs, in particular the brain, offers a plethora of biological data imaged in 3D. This technique is however often hindered by cumbersome non-automated analysis methods. Here we describe an approach to fully automate the analysis by integrating with data from the Allen Institute of Brain Science (AIBS), to provide precise assessment of the distribution and action of peptide-based pharmaceuticals in the brain. To illustrate this approach, we examined the acute central nervous system effects of the glucagon-like peptide-1 (GLP-1) receptor agonist liraglutide. Peripherally administered liraglutide accessed the hypothalamus and brainstem, and led to activation in several brain regions of which most were intersected by projections from neurons in the lateral parabrachial nucleus. Collectively, we provide a rapid and unbiased analytical framework for LSFM data which enables quantification and exploration based on data from AIBS to support basic and translational discovery.

Introduction

Light Sheet Fluorescence Microscopy (LSFM) is an imaging system with high sensitivity, micrometer resolution, and short acquisition time enabling imaging of a whole mouse brain in less than one hour[1]. This technology was previously used to evaluate the access of fluorescently labelled peptides from the periphery to the brain[2]. Quantification of the 3D brain distribution by manual annotation however is a slow process hindering high-throughput analysis of the large data sets. Recently, it was shown how the Common Coordinate Framework version 3 (CCFv3) of the Allen Institute for Brain Science (AIBS) can be utilized to automatically perform quantitative analysis of LSFM data based on image registration[3,4]. In the work by Reiner et al.[3], the authors used the digital CCFv3 atlas as basis for quantifying whole brain activity by automated analysis of immediate early genes such as c-Fos. A similar strategy for mapping c-Fos activation using image registration was performed by Kim et al.[5]. Here, we present a similar image registration approach, which extends the automated analysis further by utilizing the multi-modality nature of the AIBS atlas, which besides an average mouse brain template based on tissue auto-fluorescence[6] also contains an aligned histology-based template constructed from Nissl-stained brain sections[7]. This enables mapping of 3D information from LSFM together with 2D information from histological techniques such as *in situ* hybridization (ISH), for direct data comparison. In this manuscript we utilized LSFM to map brain distribution of fluorescently labelled peptides as well as whole brain c-Fos activation. ISH was used to map the localization of the peptide's endogenous receptor.

The AIBS data portal contains impressive amounts of open science data including expression patterns of approximately 20,000 genes in the adult mouse brain[7], and a brain-wide, cellular-level, mesoscale connectome for the mouse describing neural connectivity between brain regions[6]. Scientists at AIBS have mapped these data to the CCFv3 atlas for efficient online browsing and quantification. However, using the online tools there is no method to automatically compare data from user experiments with content from the AIBS data portal, presenting an unmet need. Our integrated brain atlas approach allows the researcher to download data sets from the AIBS data portal and directly integrate with user LSFM experiments. Thousands of high-resolution connectivity maps of neural connections in the mouse brain from a range of mouse lines are hence available for direct numerical comparison with the user LSFM data. Together, our integrated atlas approach provides a high throughput setup allowing automated comparison and quantification of peptide brain access, receptor expression, cell activation, and brain connectivity.

The glucagon-like peptide-1 receptor agonist (GLP-1RA) was chosen as a model drug to highlight the possibilities with our novel analysis approach. Liraglutide is a GLP-1RA approved and widely used for the treatment of diabetes[8], and is also approved as a treatment option for weight management, reducing appetite and body weight following peripheral once-daily administration[9]. It has been shown that GLP-1RAs act on peripheral organs but also target GLP-1 receptors (GLP-1R) in the brain. The brain actions of liraglutide are thought to contribute in large part to the weight loss effect[2,10]. Here, we first mapped the brain distribution of fluorescently labelled liraglutide following peripheral injection. The brain distribution signal was compared to the location of *glp-1r* expressing cells, pointing to potential peptide targets throughout the brain. Brain activation in response to peripheral administered liraglutide was quantified by mapping whole brain c-Fos activation compared to vehicle dosed controls. To increase the understanding of the activated neural networks the c-Fos findings were compared with neural connectivity maps from the AIBS data portal. Comparing the connectivity maps with liraglutide induced c-Fos increase, showed a robust correlation of activation cascades involving projections from the parabrachial nucleus (PB). Collectively, the integrated brain atlas approach combined with easy-to-use visualization tools and quantification model was shown to enable high-throughput studies aiming to investigate peptides with brain mode-of-action.

Results

Integrated brain atlas. The CCFv3 from AIBS was used as basis for constructing an integrated brain atlas to enable quantification and comparison of data regarding brain access, receptor location, neural activity, and brain connectivity. The atlas implementation combines user data from LSFM and histology, as well as connectivity maps downloaded from the AIBS data portal (Fig. 1a-c). LSFM was used to image *in vivo*-dosed fluorescently labelled peptides as well as whole brain immunohistochemistry (IHC) showing c-Fos activation. Histology was used to map *glp-1r* expressing cells using *in situ* hybridization (ISH). Alignment to the integrated brain atlas was performed using the image registration software Elastix[11] using affine and b-spline transformations for each of the larger brain structures (Supplementary Fig. 1). For exploration purposes, all mapped data were imported into a commercially

available software program allowing visualization of 3D maximum intensity projections as well as sagittal, horizontal, and coronal 2D projection images (Fig. 1d). Visual comparisons of results from different experiments were achieved by constructing average 3D signals combining individual brain samples, and overlaying these resulting average signals onto the CCFv3 template (Fig. 2). The average brain signals provide a compact representation of the raw data, which can be easily stored and later compared to future experiments. Automatic extraction of statistical measures in brain regions of interest was performed using the annotated model of the CCFv3 (Fig. 1e). Data presented in the following result sections were all automatically mapped to the integrated brain atlas enabling combined visualization and quantification (Fig. 1f).

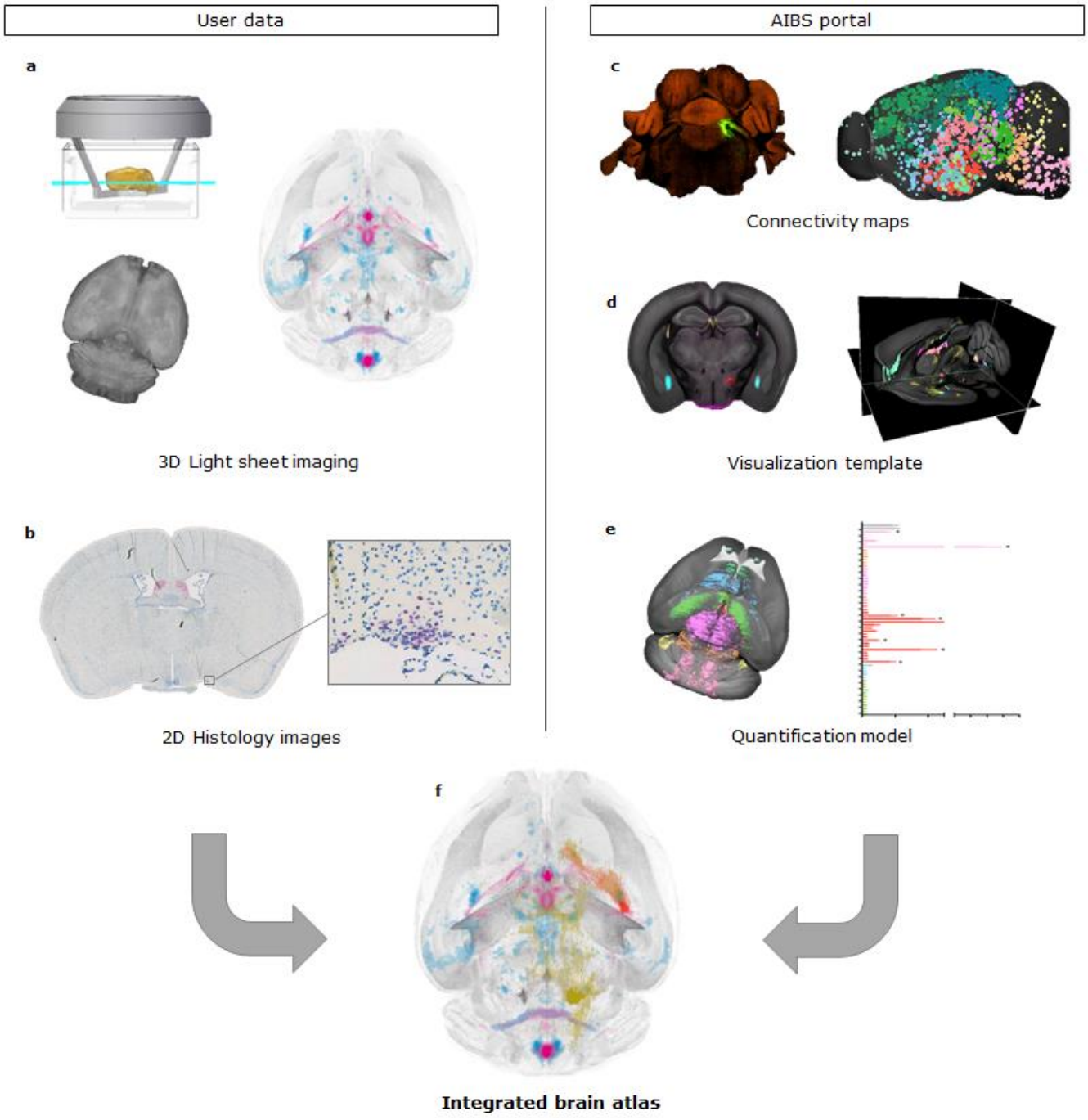

Figure 1 I Multi-modality brain atlas integrating information from user data and AIBS data portal. (a) LSFM data showing brain distribution of labelled peptides (pink), as well as brain activation patterns (blue) using whole brain IHC staining for c-Fos. Top left drawing shows a mouse brain (yellow) imaged by a light sheet (green). (b) Histology data showing receptor location based on *in situ* hybridization (ISH). (c) Connectivity maps from the AIBS data portal[6]. Left: example of injected viral tracer. Right: Colored circles indicating the primary injection site of each experiment. (d) Screen shots from a commercial 3D image rendering software used to explore overlay images of data mapped to the integrated brain atlas. (e) Illustration showing that all mapped data can be quantified automatically using the annotation of the CCFv3. The graph data is from Fig. 2b. (f) Illustration of the integrated brain atlas allowing quantification and comparison between experiments from different image modalities and labelling techniques. Data can be easily navigated as maximum intensity projections (3D) or orthogonal projections (2D).

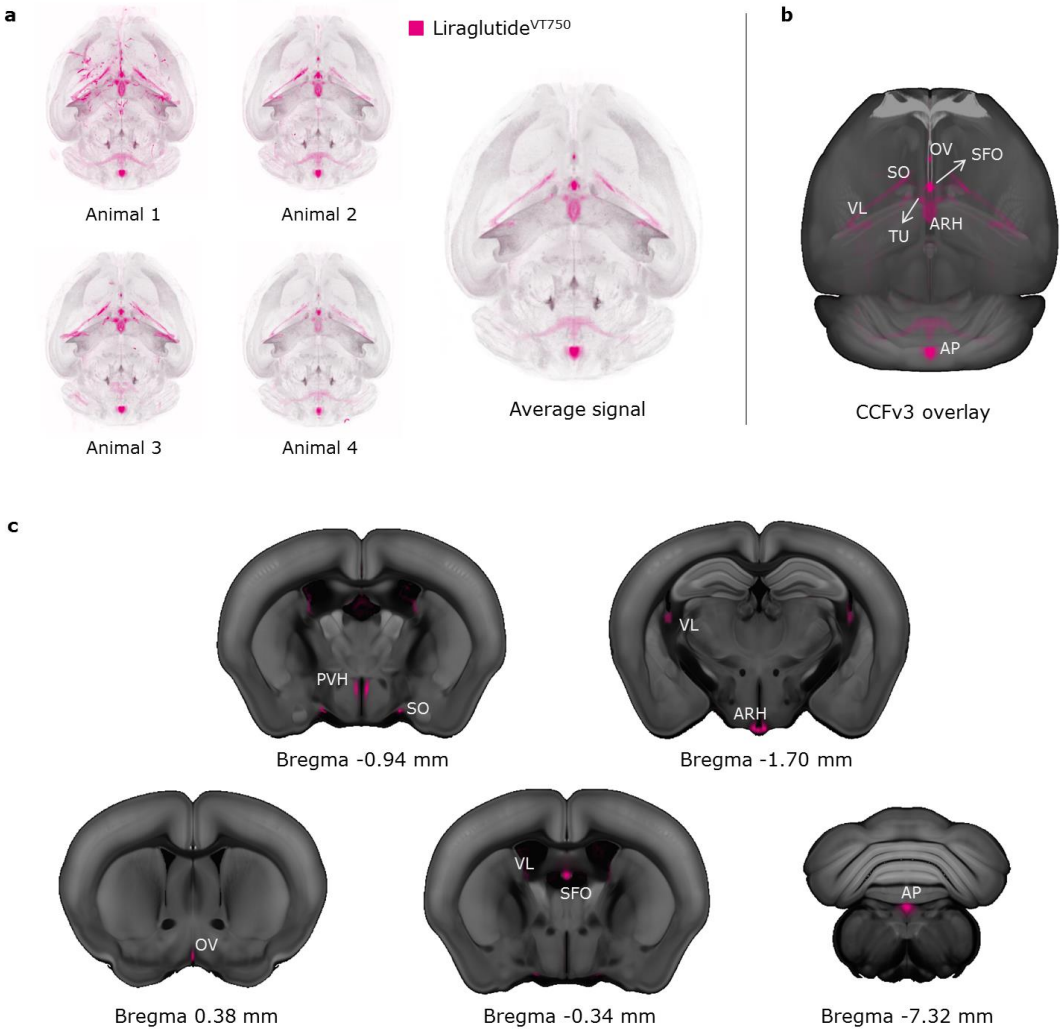

Figure 2 I Average brain signals. (a) Example of maximum intensity projection images created from four individual brains from mice injected I.V. with liraglutide^{VT750}. The brains were registered to the atlas space and a voxel-wise average distribution signal representing the experiment group was computed. (b) The average signal from (a) overlaid onto the CCFv3 template. (c) Coronal projection images constructed from (b). The color map was adjusted by a factor 2.5 in the top row to ease visualization of the lower signals in the non-circumventricular regions compared to the higher signals in the circumventricular regions (bottom row).

Fluorescently labelled liraglutide distributes to regions in hypothalamus and brainstem following peripheral administration. GLP-1 is an incretin hormone, physiologically released from intestinal L-cell in response to food intake, but also produced and released as a neurotransmitter mainly from hindbrain neurons[12]. As the GLP-1R distribution is abundant in the brain[13,14], we first sought to investigate which brain regions had access to the GLP-1RA liraglutide when injected peripherally. VivoTag-S®750 labelled liraglutide (liraglutide^{VT750}) previously used to investigate brain access[2] was administered intravenously in C57BL/6J mice and compared to vehicle dosed controls. The observed liraglutide^{VT750} signals were mapped to the integrated brain atlas, and the total fluorescence signal in selected regions was quantified (Fig. 3c). The analysis was enabled by registration of the auto-fluorescence channel of the LSFM acquisition to the CCFv3 template allowing quantification of the specific liraglutide^{VT750} signal using the atlas annotations (Fig. 3a-b). Using the nomenclature of the AIBS mouse brain atlas, liraglutide^{VT750} was significantly detected in circumventricular organs (CVOs) such as area postrema (AP) and vascular organ of the lamina terminalis (OV), as well as in regions shielded by the blood brain barrier (BBB) such as arcuate hypothalamic nucleus (ARH), paraventricular hypothalamic nucleus (PVH), and Supraoptic nucleus (SO). Liraglutide^{VT750} was also observed in the choroid plexus (chpl), exemplified by the plexus located in the fourth (V4) and lateral (VL) ventricle. To validate the findings another group of C57BL/6J mice were dosed with cy3 labelled liraglutide and the brains were processed for confocal microscopy (Fig. 4). In general there was good agreement of targeted brain regions detected using the two different methods, except in NTS, DMX, and SF, where significantly lower signals were observed with confocal microscopy. To visualize the brain distribution of liraglutide^{VT750} an average distribution signal was computed and imported into the integrated brain atlas (Fig. 3d). It was observed that many regions with liraglutide^{VT750} access were in near proximity of the CVOs which contain fenestrated capillaries allowing free access of blood borne molecules. To elaborate on this, the distance from the CVOs to the complete liraglutide^{VT750} distribution was evaluated. This was performed by peripheral administration of fluorescently labelled MECA-32 antibody, which exclusively labels the fenestrated capillaries[15]. Figure 5 shows a maximum intensity projection of the MECA-32^{VT750} signal in the brain, together with a distance map constructed by computing the distance from any voxel in the integrated brain atlas to the nearest voxels containing MECA-32^{VT750} signal. The distance map was used to quantify the relationship between liraglutide^{VT750} and the fenestrated capillaries. The distances in most regions were small suggesting diffusion or integrated uptake of the labelled liraglutide following access through fenestrated capillaries. However, the distances in PVH, SO, and TU were significantly larger suggesting another mechanism of access to these regions.

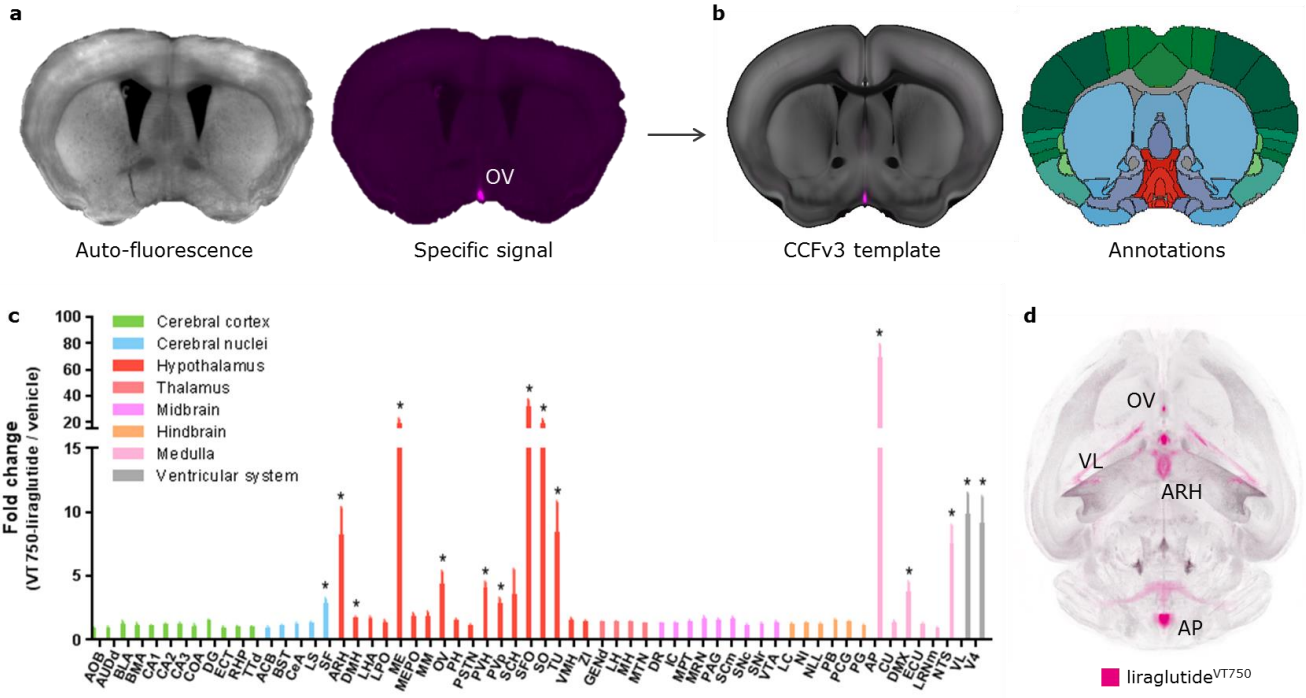

Figure 3 I Brain regions with liraglutide^{VT750} access. (**a**) 2D coronal projections from data acquired with LSFM following liraglutide^{VT750} administration in C57BL/6J mice. The specific signal was mapped to the integrated brain atlas for quantification following auto-fluorescence background reduction by spectral unmixing. (**b**) 2D projection showing a mapped liraglutide^{VT750} signal overlaid onto the CCFv3 atlas template. Automated quantification was achieved using the corresponding annotations. (**c**) Bar graph showing the mean fold change and standard deviation (SD) of the total fluorescence signal in selected brain regions comparing liraglutide^{VT750} and vehicle (n=5). An asterisk marks significant difference between treatments when analyzed in individual brain regions using a false discovery rate value of 5% to correct for multiple comparisons. Note the split y-axis when interpreting results and standard deviations. See Supplementary Table 1 for full brain region names. (**d**) Maximum intensity projection of the average liraglutide^{VT750} signal computed from the individual brains in the study group (n=5).

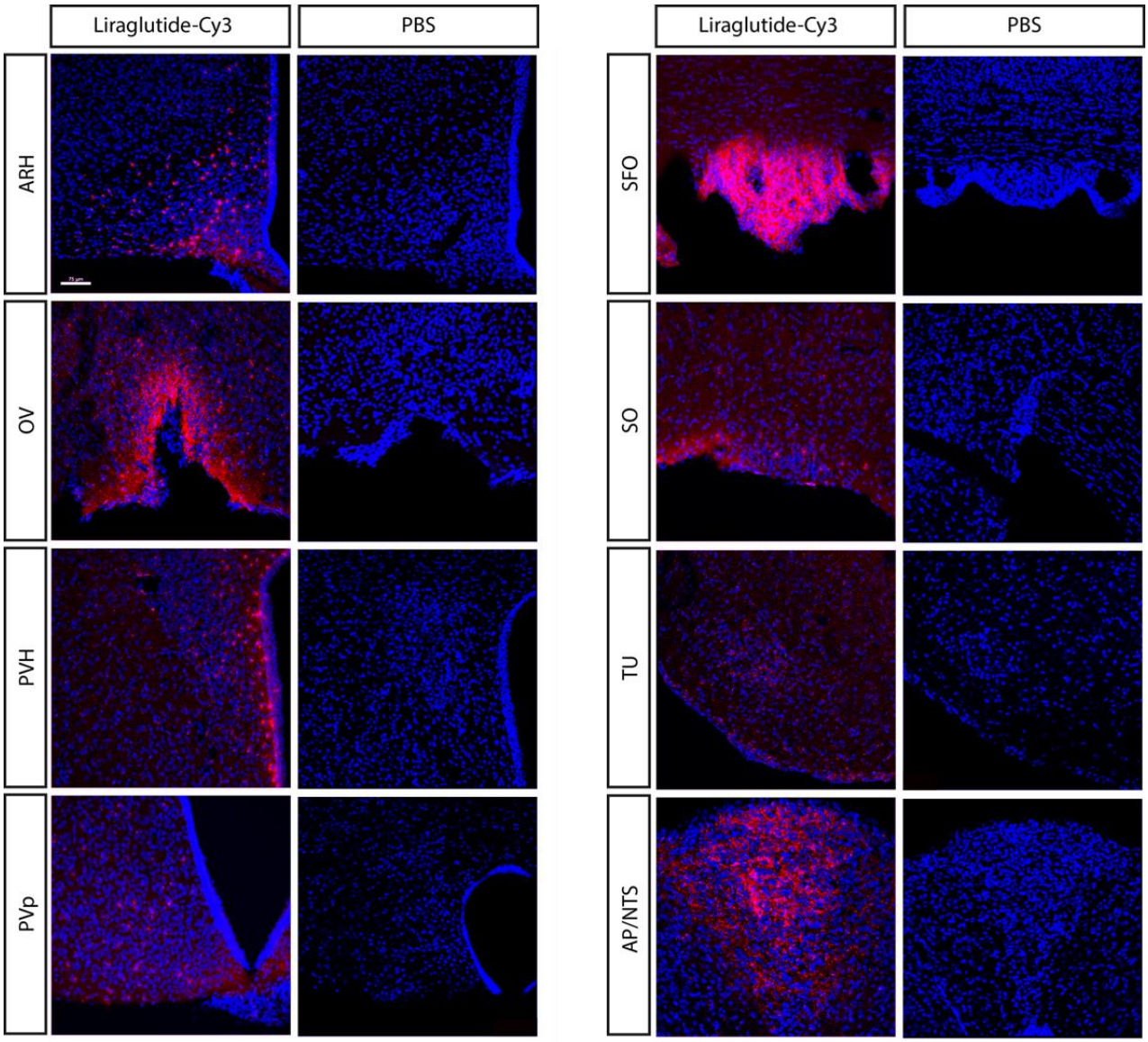

Figure 4 I Confocal images of liraglutide^{Cy3}. Overview of liraglutide^{Cy3} in the mouse brain. High magnification confocal images from mice injected with liraglutide^{Cy3}. Brain regions where liraglutide^{Cy3} (red) stained with DAPI nuclear stain (blue) were observed, compared to the corresponding region from an animal injected with vehicle (PBS).

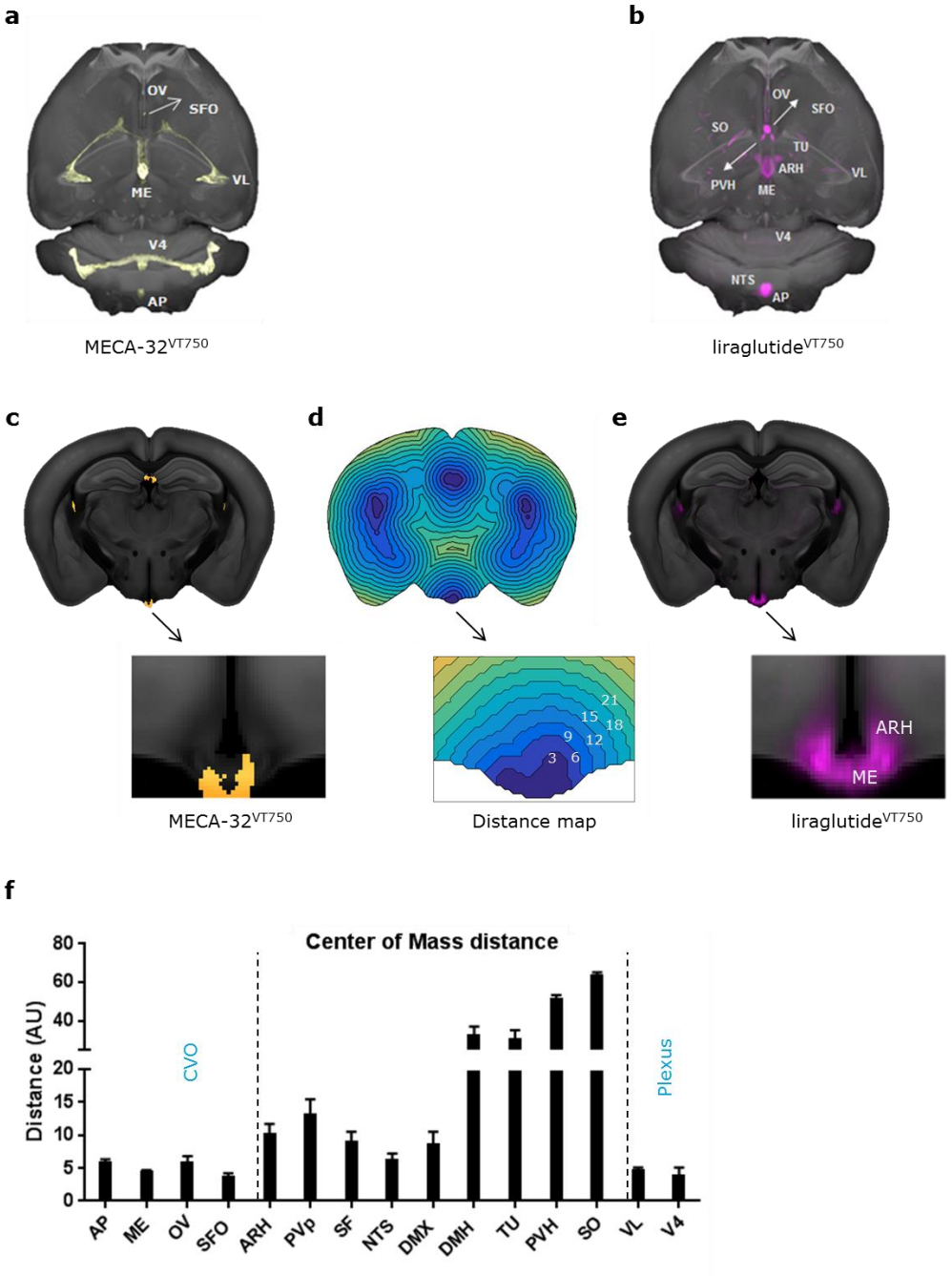

Figure 5 I Distance map calculations. (**a**) Fenestrated capillaries visualized by maximum intensity projection of a MECA-32^{VT750} brain signal overlaid onto the CCFv3 template**.** (**b**) Maximum intensity projection of average liraglutide^{VT750} signal (n=5) overlaid onto the CCFv3 template. (**c**) Coronal projection of the MECA-32^{VT750} signal registered to the atlas space and overlaid onto the CCFv3 template. (**d**) Distance map constructed from the MECA-32^{VT750} signal. The value at a given voxel was assigned as the shortest Euclidian distance to a voxel classified as MECA-32^{VT750} positive. Blue indicate voxels close to fenestrated capillaries, while yellow indicate voxels far from fenestrated capillaries. (**e**) Average liraglutide^{VT750} signal overlaid onto a coronal section of the CCFv3 template. (**f**) Center of mass distances computed for the liraglutide^{VT750} signals described in Fig. 3. The computation was performed in the brain regions marked for discovery in Figure 3c.

Aligning histology and LSFM data highlights possible direct targets of liraglutide. To have a direct brain effect the administered liraglutide must activate its receptor, the GLP-1R. To further elaborate the relevance of the brain distribution of liraglutide^{VT750} a comparison was made between the average distribution signal and cells expressing *glp-1r* mRNA. The ISH platform RNAscope[16,17] was used to map the *glp-1r* mRNA location in a number of coronal slides throughout the C57/BL6 mouse brain. To enable direct comparisons of images from 2D histology with 3D LSFM imaging (Fig. 6a), a heat map was computed from the ISH section to represent the *glp-1r* positive cells. The heat map was aligned to the integrated brain atlas, which enabled direct visual comparison with the average liraglutide^{VT750} distribution from Figure 3d. An example of a mapped *glp-1r* ISH heat map compared to the corresponding anatomical location in the average liraglutide^{VT750} distribution signal is seen in Fig. 6b. In this anatomical location the liraglutide^{VT750} distribution signal overlapped with the *glp-1r* signal in SO and SFO, while a liraglutide^{VT750} signal was also observed in the chpl located in VL where no receptor signal was present. Receptor expression was observed in Lateral septal nucleus (LS), Substantia innominata (SI) and the anterior part of PVH without a corresponding liraglutide^{VT750} signal. More *glp-1r* ISH images were obtained for regions with liraglutide^{VT750} access (Fig. 7). Comparing to the statistical significant brain regions with liraglutide^{VT750} access (Fig. 3c), *glp-1r* was detected in ARH, DMH, PVH, OV, PVp, SO, TU, AP, and NTS providing possible direct targets of liraglutide. To further investigate liraglutide^{VT750} interaction with the GLP-1R a group of *Glp-1r*$^{-/-}$ mice was studied. In parallel to the liraglutide^{VT750} distribution study presented in the previous section, liraglutide^{VT750} was injected in *Glp-1r*$^{-/-}$ mice devoid of a functional GLP-1R. Visual and quantitative comparisons of the distribution signals showed a large decrease of signal in the knockout mice, in all brain regions except for the choroid plexus (Fig. 8). Together with the histology findings, this indicated a specific GLP-1R dependent localization of liraglutide^{VT750} in the brain.

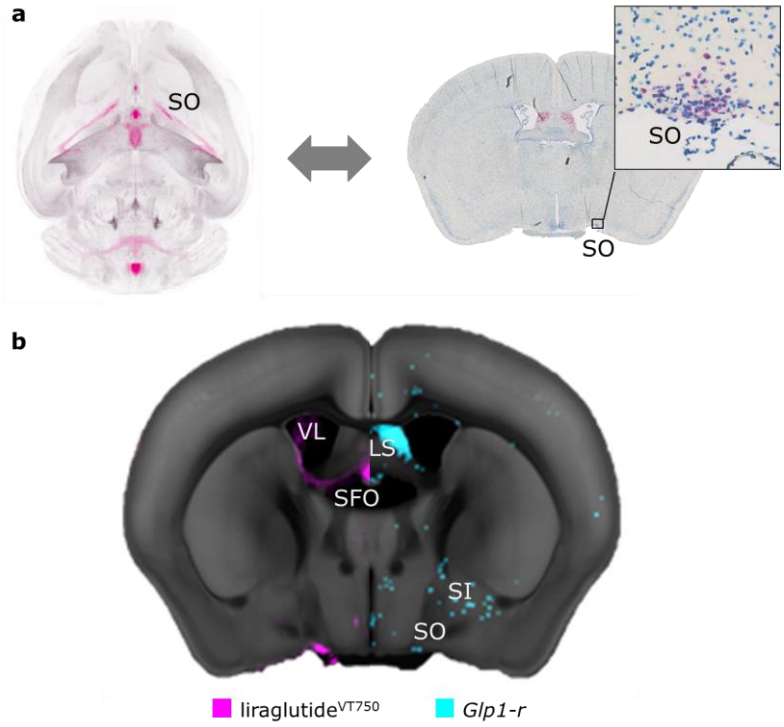

Figure 6 I Comparison of *glp-1r* localization and average liraglutide^{VT750} distribution. (a) Concept behind aligning a 2D histology image (right) with 3D LSFM data (left). A histology image was aligned to an interpolated section of the integrated brain atlas template. Once aligned a similar interpolated projection from the average liraglutide^{VT750} distribution signal could be generated. Example ISH section with zoom panel at SO region. Red color indicates cells positive for *glp-1r*. (b) Heat map (blue) representation of ISH section from Fig. 6a aligned with the average liraglutide^{VT750} signal (pink) from Fig. 3d. The signals are overlaid onto separate halves of the CCFv3 template.

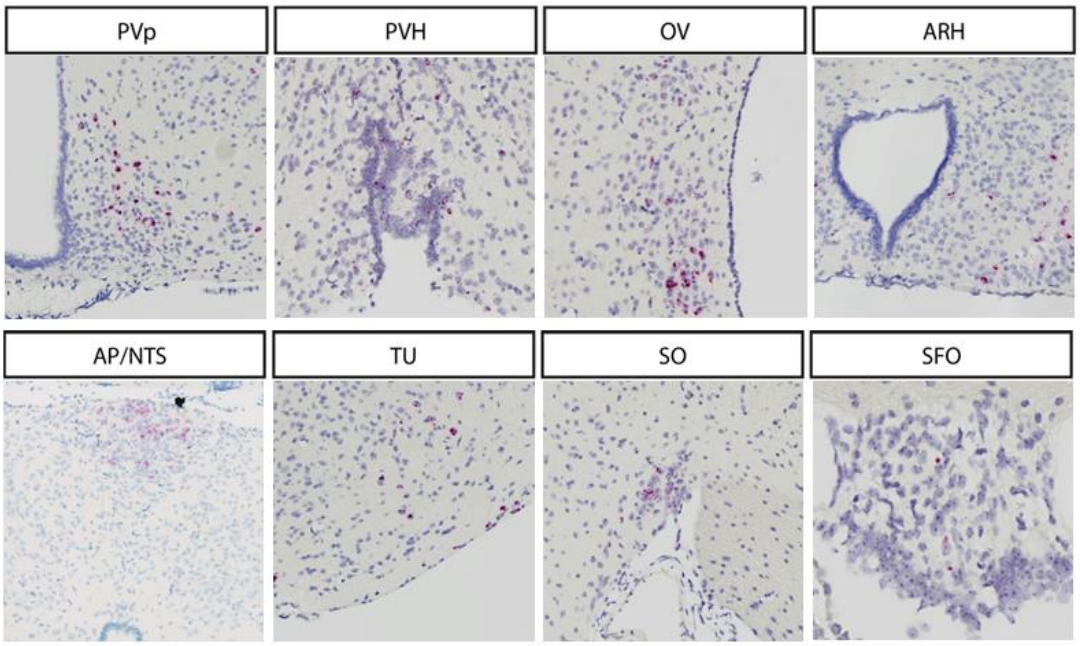

Figure 7 I Enhanced ISH images. Images show glp-1r expression in targeted brain regions. Overview of the glp-1r mRNA localization in a number of coronal sections throughout the C57/BL6 mouse brain. High magnification slide scanner images from untreated mice. Panel shows selected brain regions with glp-1r mRNA (red) counter stained with Mayer's hematoxylin (blue).

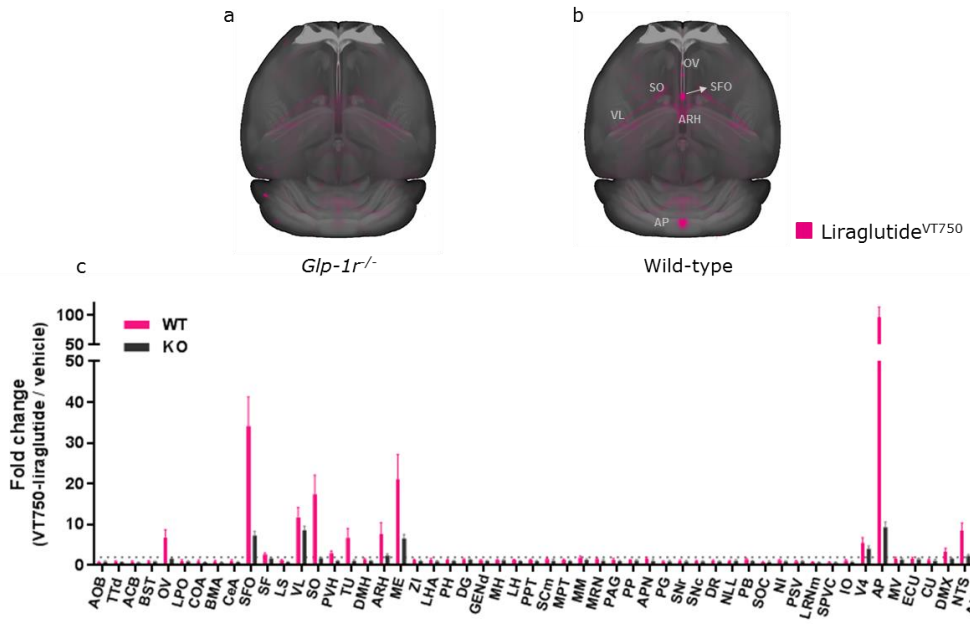

Figure 8 I Liraglutide^{VT750} in wild type vs *Glp-1r*$^{-/-}$ mice. (a) Maximum intensity projection of average liraglutide^{VT750} signal following administration in *Glp-1r*$^{-/-}$ animals overlaid onto the CCfv3 template. (b) Maximum intensity projection of liraglutide^{VT750} signal following administration in wild-type animals overlaid onto the CCfv3 template. (c) Bar graph showing mean fold change and standard deviation of vehicle normalized signals (total fluorescence) from liraglutide^{VT750} injected wild-type (WT) and *Glp-1r*$^{-/-}$ (KO) animals. See Supplementary Table 1 for full brain region names.

Whole brain c-Fos staining shows that liraglutide activates brain regions related to food intake. GLP-1RAs are known to reduce appetite following peripheral administration, and this effect has been linked to both hypothalamic and hindbrain action[2,18]. To investigate changes in brain activity following peripheral administration of liraglutide, C57BL/6J mice were dosed subcutaneously with liraglutide, and the c-Fos response was compared to vehicle dosed controls. c-Fos staining was performed on intact brains using the iDISCO protocol[19], and brains were subsequently scanned using LSFM. The most prominent c-Fos increase following liraglutide injection was seen in Bed nuclei of the stria terminalis (BST), Paraventricular nucleus of the thalamus (PVT), Central amygdala nucleus (CEA), Parabrachial nucleus (PB), and NTS (Fig. 9a). To evaluate the whole brain c-Fos response, heat maps were computed for each individual brain sample based on the amount of c-Fos positive cells, and these heat maps were registered to the integrated brain atlas (Fig. 9b). The heat maps were used to quantify the differences between liraglutide and vehicle dosed animals in select brain regions (Fig. 9c). To investigate whether the observed c-Fos response could be a direct effect of liraglutide interaction with GLP-1R we visually compared the liraglutide specific c-Fos increase with the liraglutide^{VT750} distribution from Fig. 3d. This was enabled by first computing the average c-Fos response from the liraglutide and vehicle group separately (Fig. 9d), followed by voxel wise subtraction of the vehicle response from the liraglutide response. The liraglutide specific c-Fos increase was then imported into the integrated brain atlas to allow direct overlay with the average liraglutide^{VT750} distribution signal (Fig. 9e, Supplementary movie 1). Some overlap was seen, mainly in AP, but also in ARH and OV indicating possible direct activation from liraglutide in these regions. However, the majority of c-Fos increase occurred in regions not directly targeted by liraglutide^{VT750}, indicating secondary activation. Figure 10 shows a rank plot comparing the ranks from lowest to highest fold change of data presented in Fig. 3c and Fig. 9c to give a further overview of brain regions with possible direct and secondary activation. c-Fos increase but no liraglutide^{VT750} signal, indicating secondary activation, was seen in BST, PVT, PB, and CeA which are regions previously described to be related to lowering of food intake[19,21]. Liraglutide specific c-Fos increase was also observed in the motor neurons receiving input from the vagus nerve.

Comparing c-Fos increase with AIBS connectivity maps suggests that activation may involve a common parabrachial pathway. The fact that the majority of induced brain activity seen by c-Fos increase was observed in brain regions not directly targeted by liraglutide^{VT750} likely indicates that neurons in these regions responded as part of larger neural networks. We hypothesized that these regions were part of networks related to appetite regulation and feeding behaviour. To investigate this hypothesis the complete set of grey matter connectivity maps were downloaded from the AIBS data portal (2469 experiments) and mapped together with the liraglutide specific c-Fos increase. The 2469 connectivity maps were automatically ranked by the amount of overlap with the c-Fos increase, taking into account the total overlap of the c-Fos signal and given connectivity signal in relation to the amount of c-Fos signal not overlapping with the given connectivity signal and vice versa (Fig. 11a). Supplementary Table 2 lists the 30 most overlapping connectivity maps compared to the liraglutide specific c-Fos increase. Based on the automated ranking, the most overlapping connectivity map was projections from Rasgrf2 (Rasgrf2-2A-dCre) positive cells in the NTS. In addition, several neuronal subpopulations previously described to decrease food intake were observed among the highest ranking connectivity maps. Projections from proopiomelanocortin (POMC) positive neurons (Pomc-Cre (BL)) in the ARH were ranked as the 29th most overlapping connectivity map, and targeting of this neuronal subpopulation has previously been shown following GLP-1RA stimulation[2]. Projections from PKC-delta+ positive neurons in CEA were ranked as the 15th most overlapping connectivity map. PKC-delta+ is a neuronal subpopulation which has previously been described to influence anorexigenic signals in combination with the lateral PB[21]. Based on the automated ranking, projections from the lateral PB were seen in four of the ten most overlapping connectivity maps compared to the liraglutide specific c-Fos increase. As liraglutide^{VT750} showed no significant access in the PB, this suggests a role of the PB as a relay station of input from other targeted brain regions. Glutamatergic (slc17a6-IRES-Cre) projections from the lateral PB (4th most overlapping connectivity map) and PKC-delta+ (Prkcd-GluCla-CFP-IRES-Cre) projections from the CEA were imported into the integrated brain atlas to visualize how these neurons could be part of the activated c-Fos response following liraglutide treatment (Fig. 11b-d, Supplementary movie 2). This parabrachial pathway has in recent literature been described as a general circuit causing anorexia[18,21,26], and here also appears to be involved in the acute brain activation of liraglutide.

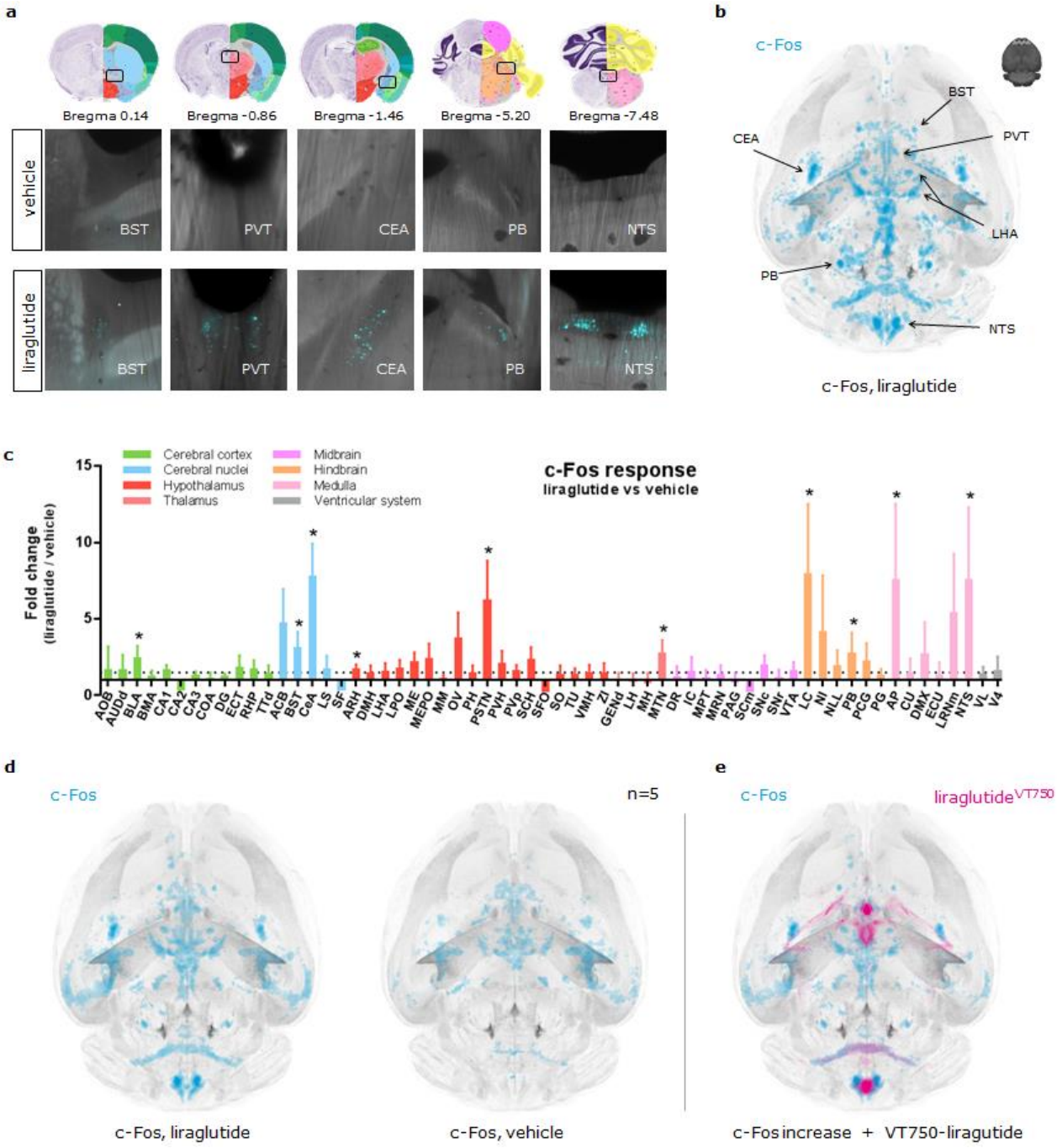

Figure 9 I Neural activation following liraglutide administration. (a) Example images of c-Fos response in liraglutide vs vehicle dosed C57BL/6J mice. Bregma coordinates denote the anatomical location. (b) c-Fos heat map computed from one liraglutide injected mouse. See also Supplementary Figure. 3. (c) Bar graph showing the mean fold change and standard deviation (SD) of total c-Fos heat map signal in selected brain regions comparing liraglutide and vehicle dosed animals. Regions were selected as having either liraglutide^{VT750} access, GLP-1R expression, or c-Fos response. An asterisk marks significant difference between treatments when analyzed in individual brain regions using a false discovery rate value of 20% to correct for multiple comparisons. See Supplementary Table 1 for full brain region names. (d) Computed average c-Fos signal from liraglutide injected animals (left), and vehicle injected animals (right). (e) Liraglutide specific c-Fos increase overlaid with the average liraglutide^{VT750} distribution from Fig. 3d.

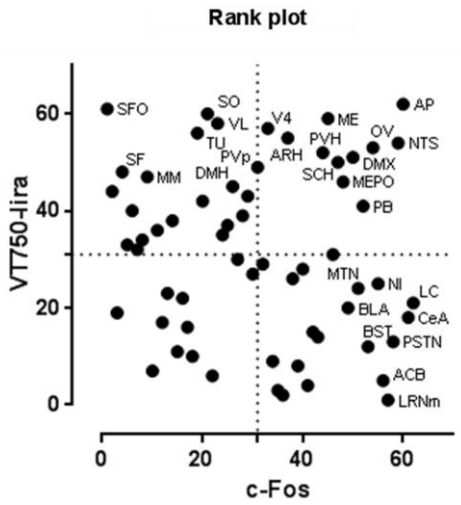

Figure 10 I Rank plot. Rank plot comparing c-Fos activation data from Figure 9c with liraglutide^{VT750} distribution data from Figure 3c. The brain regions were ranked based on their fold change value and these rankings were used as x and y coordinates in the plot. Top right corner contains brain regions where a direct activation from liraglutide is most plausible.

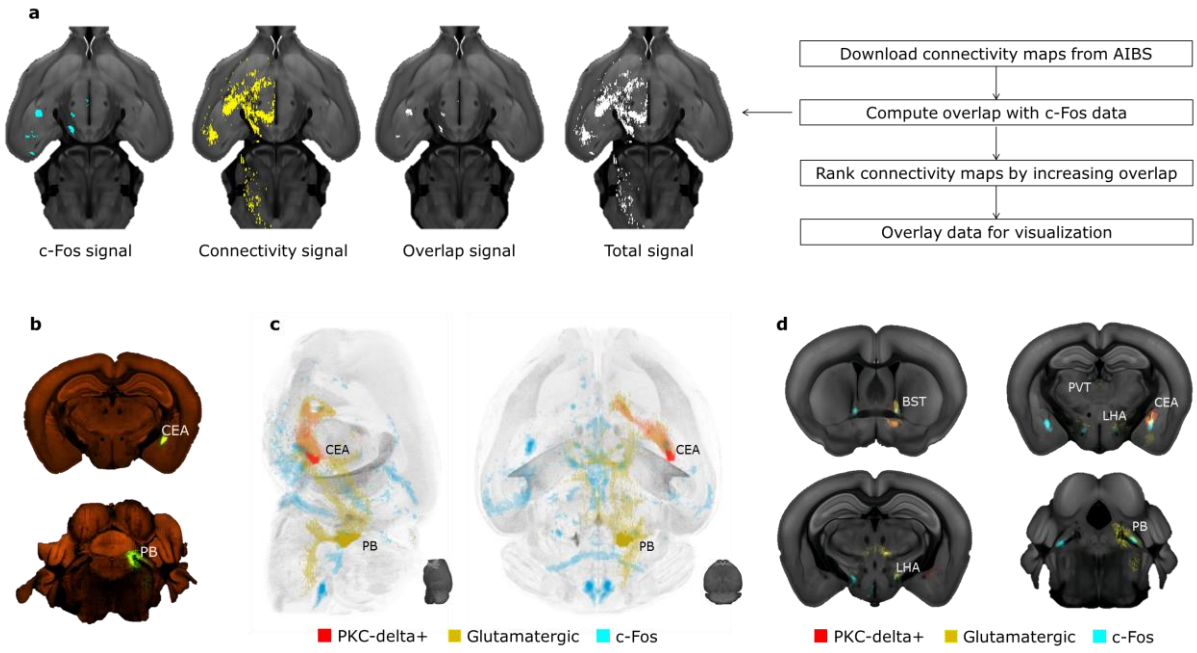

Figure 11 I Comparing brain connectivity maps with whole brain c-Fos data. (a) Left to right: Horizontal projection image of average c-Fos increase following liraglutide administration; example of corresponding horizontal projection of downloaded connectivity map; overlap signal between c-Fos signal and connectivity signal; total signal of c-Fos signal and connectivity signal. (b) Bottom: Part of primary injection site (PB) in a slc17ac cre mouse. Top: part of primary injection site (CEA) in a Prkcd-GluCla-CFP-IRES-Cre mouse. Data was downloaded from the AIBS data portal. (c) Connectivity maps visualized by maximum intensity projection overlaid with the average c-Fos increase following liraglutide administration. Left: sagittal maximum intensity projection; right: horizontal maximum intensity projection. (d) Coronal projection images showing downloaded glutamatergic projections from PB, and PKD-delta+ projections from CEA, together with the average c-Fos increase following liraglutide administration. Signals are overlaid onto the CCFv3 template.

Discussion

In this manuscript a novel analysis approach was presented, combining data from numerous sources in an integrated brain atlas including data from LSFM imaging, histology, and data from AIBS. LSFM imaging is high throughput with data acquisition times in the range of one hour for a whole mouse brain. The automated analysis approach enables the researcher to gain the advantages of this high throughput LSFM imaging system by removing the bottleneck arising from manual analysis of the large data sets. By registering the acquired whole brain data with the CCFv3 atlas from AIBS, the user can additionally align LSFM data with standard histological images, as well as automatically compare LSFM data to connectivity maps from the AIBS data portal. By combining the different imaging technologies the distribution of bioactive peptides can be correlated to the peptide's endogenous receptor, changes in brain activity, and connectivity between relevant brain regions. This provides mechanistic information that would not be afforded by a single technology alone. Furthermore, importing all experiment data to a common reference atlas effectively allows the user to build an anatomical database of information which can be compared to parallel and future studies, thereby increasing the value of each experiment.

To highlight the possibilities with this novel analysis approach the acute brain effect of the GLP-1RA liraglutide was investigated. In agreement with previous observations[2], liraglutide^{VT750} had access to the chpl, the CVOs, and regions shielded by the BBB such as ARH, PVH, SO, and TU. It should be noted that the observed liraglutide^{VT750} signals in regions close to the CVOs may have been overestimated due to the thickness and beam profile of the light sheet in the LSFM system. This was the case for the brain regions NTS, DMX, and SF comparing to detection with confocal microscopy. To minimize this issue work is needed concerning deconvolution algorithms for LSFM systems. The issue was much less pronounced in the c-Fos studies as the fluorescence signals here were much more uniform and confined to the cell bodies. By computing the distance between the fenestrated capillaries and the average liraglutide^{VT750} distribution, it was seen that the peptide likely could access the brain either by diffusion from the CVOs or by uptake through specialized cell structures intercepting the BBB protected brain regions with the CVOs. Examples of such cells are tanycytes which have previously been demonstrated to mediate uptake of other peripheral peptides in the ARH[22]. *Glp-1r* expression was observed in most brain regions with liraglutide^{VT750} access indicating that the observed liraglutide^{VT750} distribution signal was GLP-1R dependent. This was confirmed by a decreased brain distribution signal of liraglutide^{VT750} observed in *Glp-1r*$^{-/-}$ mice. Changes in brain activation following an acute subcutaneous injection of liraglutide were investigated by whole brain c-Fos staining. Visually the most prominent increases were seen in BST, PVT, CEA, PB, and NTS, while quantitative analysis also showed a significant increase in AP and ARH. Comparing the c-Fos increase to the liraglutide^{VT750} distribution it was possible that liraglutide directly activated GLP-1R in AP and ARH. c-Fos signal could not be observed in some regions with strong liraglutide^{VT750} signal such as SO, TU and SFO. Although not demonstrated before, this could be due to time related differences in protein activation of primary versus secondary activation sites or negative activation profiles counteracting the signal. As c-Fos is a marker for increased neuronal activity it is also possible that some of the effect of liraglutide is inhibitory, and hence not detected by the c-Fos analysis. A comparison between the liraglutide^{VT750} distribution signal and the liraglutide specific c-Fos increase showed that the majority of brain activation was likely to be secondary events. To understand the secondary c-Fos activation 2469 connectivity maps from the AIBS data portal were downloaded and added to the integrated brain atlas. Projections from ras-specific guanine-nucleotide releasing factor 2 (Rasgfr2) positive cells in NTS were ranked by automated computations as the most overlapping connectivity map comparing to the liraglutide specific c-Fos increase. Previous work indicates a role for Rasgfr2 in the regulation of mesolimbic dopamine neuron activity[23]. However, to the best of our knowledge no direct links has been established with appetite or body weight regulation. A strong correlation between c-Fos activation and connectivity maps were also seen with projections from the lateral PB exemplified by glutamatergic projections (slc17a6 cre). Recent work[18,24-26] describes the role of the lateral PB as a conduit for visceral signals that cause anorexia. The lateral PB has also been shown to be necessary for the acute reduction in food intake by another GLP-1RA exendin-4 in rats[27]. The lateral PB is a site of integration of satiety signals from the brainstem, but other neurons also projects to this region such as agouti-related protein AGrP and POMC positive neurons from the ARH. This suggests an interconnection between brainstem and hypothalamus input in the control of feeding. Direct projections from POMC positive neurons in the ARH also showed a general overlap with the liraglutide specific c-Fos increase, although to a lesser degree compared to projections from the lateral PB.

As all experiments were registered to a common atlas space the quality of subsequent data analysis was dependent on the registration quality. The 3DISCO clearing protocol[28] was used prior to LSFM imaging which was previously reported to introduce non-uniform tissue shrinkage[3]. To mitigate the effects of the non-uniform tissue shrinkage a registration model which allowed different degrees of shrinkage in each of the larger brain structures was introduced. The registration accuracy was tested by manually placing landmarks in the atlas template and comparing these to corresponding landmarks placed in a test set of registered brain samples. The average error between corresponding landmarks was approximately 5 voxels equal to 100 µm (Supplementary Fig. 2). The LSFM system acquires high resolution images from which lower level representations such as average distribution signals and c-Fos heat maps of brain activity were computed. These representations enabled direct visual and quantitative comparisons of results from parallel experiments. Overall, the developed analysis approach provides a strong foundation for anatomical studies and could be a valuable tool in combination with functional studies going forward. The high throughput approach enables automated analysis of user experiments based on large scale data from AIBS, and by integrating these data the goal is to discover new knowledge otherwise hidden in the large complexity of the brain.

Methods

Animals. All *in vivo* studies were conducted in accordance with approved national regulations in Denmark, which are fully compliant with internationally accepted principles for the care and use of laboratory animals, and with animal experimental licenses granted by the Danish Ministry of Justice. Animals were obtained from Taconic, Denmark and housed in standard, temperature-controlled conditions with a 12-hour-light/dark cycle. The animals had ad libitum access to water and regular chow.

Distribution of liraglutide^{VT750}. Fluorescently labelled liraglutide was synthesized by conjugating VivoTag-S®750 NIR FLUOROCHROME LABEL (Perkin Elmer) to the liraglutide peptide. Liraglutide^{VT750} (30 nmol/kg) or vehicle (PBS) were injected I.V. into male (n=6) C57BL/6J wild type and *Glp-1r*$^{-/-}$ mice, and left to circulate for 6 hours in the animals. The mice were euthanized using cardiac perfusion with 10% neutral buffered formalin (NBF), followed by overnight fixation in NBF at room temperature overnight, and subsequently cleared using the 3DISCO protocol[28].

Distribution of liraglutide^{Cy3}. Fluorescently labelled liraglutide was synthesized by conjugating Cyanine 3 (Cy3) (Lumiprobe) to the liraglutide peptide. Liraglutide^{Cy3} (120 nmol/kg) or vehicle (PBS) were injected I.V. into male (n=3) C57Bl/6J mice and left to circulate for 6 hours in the animals. The mice were anesthetized using isoflurane, and euthanized using cardiac perfusion with first saline followed by 4% paraformaldehyde (PFA), the brains were then collected and post fixated in 4% PFA at room temperature overnight. After post fixation, the brains were transferred to 25% sucrose solution, once the brains had descended to the bottom of the well they were sectioned coronally using a cryostat at 35 µm and collected in 6 series. One series from each mouse was stained with DAPI (1:1000). Confocal images from various brain regions were acquired using a Leica SP8 (Leica DMi8).

Distribution of MECA-32^{VT750}. Fluorescently labelled MECA-32 antibody was synthesized by conjugating VivoTag-S®750 NIR FLUOROCHROME LABEL (Perkin Elmer) to the MECA-32 antibody (BE0200) from BioXCell. MECA-32^{VT750} (0.2 mg/kg) were injected I.V. into male (n=2) C57BL/6J wild type mice, and left to circulate for 6 hours in the animals. The mice were euthanized using cardiac perfusion with 10% NBF, followed by overnight fixation in NBF at room temperature overnight, and subsequently cleared using the 3DISCO protocol[29].

Whole brain c-Fos staining. C57Bl/6J male mice were subcutaneously injected with liraglutide (0.4 mg/kg) or vehicle (n=6). Mice were euthanized 4 hours after injection using isofluorane followed by cardiac perfusion with 4% paraformaldehyde. Brains were excised and post fixed in 4% paraformaldehyde overnight at room temperature and transferred stepwise to 100% methanol using the following protocol. 20% methanol (in ddH2O) for 1h, 40% methanol for 1h, 60% methanol for 1h, 80% methanol for 1h, and 100% methanol for 1h twice. iDISCO staining was performed as described in Renier et al.[19] with one exception. All the washing steps after incubation with primary and secondary antibody were extended from one to three days. Incubation time for primary and secondary antibody was 4 days each. The primary antibody was Rabbit pAb anti c-Fos (Ab-5) (4-17) from Calbiochem (1:10,000 dilution), and the secondary antibody was Cy5-anti rabbit from Jackson Immunoresearch (1:1000 dilution).

Light sheet imaging. Brain samples were scanned using an UltraMicroscope II LSFM system (Lavision Biotec, Bielefeld,

Germany) in 10.32 µm isotropic resolution for the liraglutide^{VT750} distribution study, and 4.06 µm for the c-Fos activation study. For labelled peptides data acquisition was performed using a 620 nm emission filter for imaging auto-fluorescence, and a 710 nm emission filter for imaging specific signals. With whole brain c-Fos staining the auto-fluorescence was recorded at 545 nm, while the c-Fos signal was acquired with a 620 nm emission filter.

RNAscope ISH. C57Bl/6J male mice (n=2) were perfused and post-fixed as described previously[29] and tissues were subsequently paraffin-embedded and sectioned at 5 µm intervals. Automated ISH was performed on a Ventana Discovery ULTRA following the technical bulletin provided by ACD Bio (#322250-USM-ULT). Our assay utilized the Ventana mRNA RED Detection Kit (Roche, #7074654001), RNAscope RED kit (ACD Bio, #322250), and the following oligonucleotide probes from ACD Bio: Mm-Glp1r (#418859), Mm-Polr2a (#312479), Mm-NPY (#313329), and dapB (#312039). Mm-Polr2a and Mm-NPY served as positive controls, and dapB was used as a negative control. ISH sections were subsequently counterstained in 30 dips of Mayer's hematoxylin, coverslipped, and scanned on a Zeiss AxioScan at 40x magnification. To assist in aligning ISH data with the integrated brain atlas, Nissl staining (0.1% w/v cresyl violet with 0.5% v/v glacial acetic acid, 5 minute incubation) was performed on adjacent brain sections from each series of tissue collected for ISH.

Image analysis. Images were registered using the Elastix software library[11]. A source image $I_S(x)$ was registered to a target image $I_T(x)$ by finding a coordinate transformation $T(x)$ that made $I_S(T(x))$ spatially aligned with $I_T(x)$. We used an affine coordinate transformation for initialization followed by non-rigid b-spline coordinate transformation which was iteratively optimized with respect to the mutual information between the source and the target. Registration parameters for mapping of LSFM data were similar to those used in Renier et al.[3]. Parameters for registration of histology sections were similar to those used in Abdelmoula et al.[30]. Spectral unmixing was performed to minimize the contribution of tissue auto-fluorescence in the liraglutide^{VT750} distribution study. The estimated auto-fluorescence contribution in the specific channel was calculated and removed based on ratios of voxel intensities between selected voxels in the unspecific recording and the corresponding voxels in the specific recording. A ratio was computed for 40 sets of voxels selected based on the histogram of the unspecific recording. The unmixing algorithm was written in Matlab (Release 2012b, MathWorks, Natick, Massachusetts, United States) and applied as a XT-plugin in Imaris (Release 7.6.5, Bitplane, Zurich, Switzerland). These software programs were also used to generate all figures in the manuscript, except Supplementary Fig. 1e which was generated using SimpleElastix[31]. The atlas templates and associated ImarisXT plugins are freely available and can be requested by emailing the corresponding author.

Statistical analysis. ROI based analysis of the total fluorescence signal presented in Fig. 3c, and c-Fos heat map intensities in Fig. 9c, were computed using multiple t-tests assuming unequal variance. Statistical significance was determined by correcting for multiple comparisons using a false discovery rate set to 5% for labelled peptides and 20% for c-Fos heat maps. The statistical analysis was performed using Graphpad Prism (Release 6, GraphPad Software, Inc., United States).

References

1. Dodt, Hans-Ulrich, et al. "Ultramicroscopy: three-dimensional visualization of neuronal networks in the whole mouse brain." Nature methods 4.4 (2007): 331-336.

2. Secher, Anna, et al. "The arcuate nucleus mediates GLP-1 receptor agonist liraglutide-dependent weight loss." The Journal of clinical investigation 124.10 (2014): 4473-4488.

3. Renier, Nicolas, et al. "Mapping of Brain Activity by Automated Volume Analysis of Immediate Early Genes." Cell (2016).

4. Jensen, Casper Bo, et al. "Quantification of brain access of exendin-4 in the c57bl mouse model by spim fluorescence imaging and the allen mouse brain reference model." Scandinavian Conference on Image Analysis. Springer International Publishing, 2015.

5. Kim, Yongsoo, et al. "Mapping social behavior-induced brain activation at cellular resolution in the mouse." Cell reports 10.2 (2015): 292-305.

6. Oh, Seung Wook, et al. "A mesoscale connectome of the mouse brain." Nature 508.7495 (2014): 207-214.

7. Lein, Ed S., et al. "Genome-wide atlas of gene expression in the adult mouse brain." Nature 445.7124 (2007): 168-176.

8. Nauck, M. A., et al. "Five weeks of treatment with the GLP-1 analogue liraglutide improves glycaemic control and lowers body weight in subjects with type 2 diabetes." Experimental and clinical endocrinology & diabetes 114.08 (2006): 417-423.

9. O'Neil, Patrick M., et al. "EFFECTS OF LIRAGLUTIDE 3.0 MG ON WEIGHT AND RISK FACTORS IN HISPANIC VERSUS NON-HIPANIC POPULATIONS: SUBGROUP ANALYSIS FROM SCALE RANDOMIZED TRIALS." Endocrine Practice 22.11 (2016): 1277-1287.

10. Sisley, Stephanie, et al. "Neuronal GLP1R mediates liraglutide's anorectic but not glucose-lowering effect." The Journal of clinical investigation 124.6 (2014): 2456-2463.

11. Klein, Stefan, et al. "Elastix: a toolbox for intensity-based medical image registration." IEEE transactions on medical imaging 29.1 (2010): 196-205.

12. Trapp, Stefan, and Simon C. Cork. "PPG neurons of the lower brain stem and their role in brain GLP-1 receptor activation." American Journal of Physiology-Regulatory, Integrative and Comparative Physiology 309.8 (2015): R795-R804.

13. Merchenthaler, Istvan, Malcolm Lane, and Paul Shughrue. "Distribution of pre-pro-glucagon and glucagon-like peptide-1 receptor messenger RNAs in the rat central nervous system." Journal of Comparative Neurology 403.2 (1999): 261-280.

14. Cork, Simon C., et al. "Distribution and characterisation of glucagon-like peptide-1 receptor expressing cells in the mouse brain." Molecular metabolism 4.10 (2015): 718-731.

15. Mullier, Amandine, et al. "Differential distribution of tight junction proteins suggests a role for tanycytes in blood-hypothalamus barrier regulation in the adult mouse brain." Journal of Comparative Neurology 518.7 (2010): 943-962.

16. Wang, Fay, et al. "RNAscope: a novel in situ RNA analysis platform for formalin-fixed, paraffin-embedded tissues." The Journal of Molecular Diagnostics 14.1 (2012): 22-29.

17. Anderson, Courtney M., et al. "Fully Automated RNAscope In Situ Hybridization Assays for Formalin-Fixed Paraffin-Embedded Cells and Tissues." Journal of cellular biochemistry (2016).

18. Carter, Matthew E., et al. "Genetic identification of a neural circuit that suppresses appetite." Nature 503.7474 (2013): 111-114.

19. Renier, Nicolas, et al. "iDISCO: a simple, rapid method to immunolabel large tissue samples for volume imaging." Cell 159.4 (2014): 896-910.

20. Betley, J. Nicholas, et al. "Parallel, redundant circuit organization for homeostatic control of feeding behavior." Cell 155.6 (2013): 1337-1350.

21. Cai, Haijiang, et al. "Central amygdala PKC-[delta]+ neurons mediate the influence of multiple anorexigenic signals." Nature neuroscience 17.9 (2014): 1240-1248.

22. Balland, Eglantine, et al. "Hypothalamic tanycytes are an ERK-gated conduit for leptin into the brain." Cell metabolism 19.2 (2014): 293-301.

23. Stacey, David, et al. "RASGRF2 regulates alcohol-induced reinforcement by influencing mesolimbic dopamine neuron activity and dopamine release." Proceedings of the National Academy of Sciences 109.51 (2012): 21128-21133.

24. Wu, Qi, Maureen P. Boyle, and Richard D. Palmiter. "Loss of GABAergic signaling by AgRP neurons to the parabrachial nucleus leads to starvation." Cell 137.7 (2009): 1225-1234.

25. Roman, Carolyn W., Victor A. Derkach, and Richard D. Palmiter. "Genetically and functionally defined NTS to PBN brain circuits mediating anorexia." Nature Communications 7 (2016).

26. Campos, Carlos A., et al. "Parabrachial CGRP neurons control meal termination." Cell metabolism 23.5 (2016): 811-820.

27. Swick, Jennifer C., et al. "Parabrachial nucleus contributions to glucagon-like peptide-1 receptor agonist-induced hypophagia." Neuropsychopharmacology 40.8 (2015): 2001-2014.

28. Ertürk, Ali, et al. "Three-dimensional imaging of solvent-cleared organs using 3DISCO." Nature protocols 7.11 (2012): 1983-1995.

29. Mercer, Aaron J., et al. "Temporal changes in nutritional state affect hypothalamic POMC peptide levels independently of leptin in adult male mice." American Journal of Physiology-Endocrinology and Metabolism 306.8 (2014): E904-E915.

30. Abdelmoula, Walid M., et al. "Automatic registration of mass spectrometry imaging data sets to the Allen brain atlas." Analytical chemistry 86.8 (2014): 3947-3954.

31. Marstal, Kasper, et al. "SimpleElastix: A user-friendly, multi-lingual library for medical image registration." Proceedings of the IEEE Conference on Computer Vision and Pattern Recognition Workshops. 2016.

Acknowledgements

CJ is funded by Innovation Fund Denmark and Novo Nordisk A/S. KM is supported by The Dutch Technology Foundation (Stichting Technische Wetenschappen), grant number 13351, and the Netherlands Organisation for Scientific Research NWO, grant number 184033111. All other work was fully funded by Novo Nordisk A/S.

Author contributions

CJ, TL, SG, JH, and AS designed the research. AC, KC, JH, AD, AS, and LK supervised the research. CJ, TL, AM, KM, and SG performed the research. CJ and TL analyzed the data. CJ wrote the manuscript.

Competing financial interests

Novo Nordisk markets liraglutide for the treatment of diabetes and weight management. CJ, TL, SG, TA, AM, AC, JH, LK, and AS are all full time employees of Novo Nordisk, and hold minor share portions as part of their employment.

Supplementary Information

The Supplementary Information contains:

Supplementary Figures

Integrated Brain Atlas for Unbiased Mapping of Nervous System Effects Following Liraglutide Treatment

- S1. **Image registration**
- S2. **Accuracy of image registration**
- S3. **c-Fos heat maps**

S1. **Image registration**

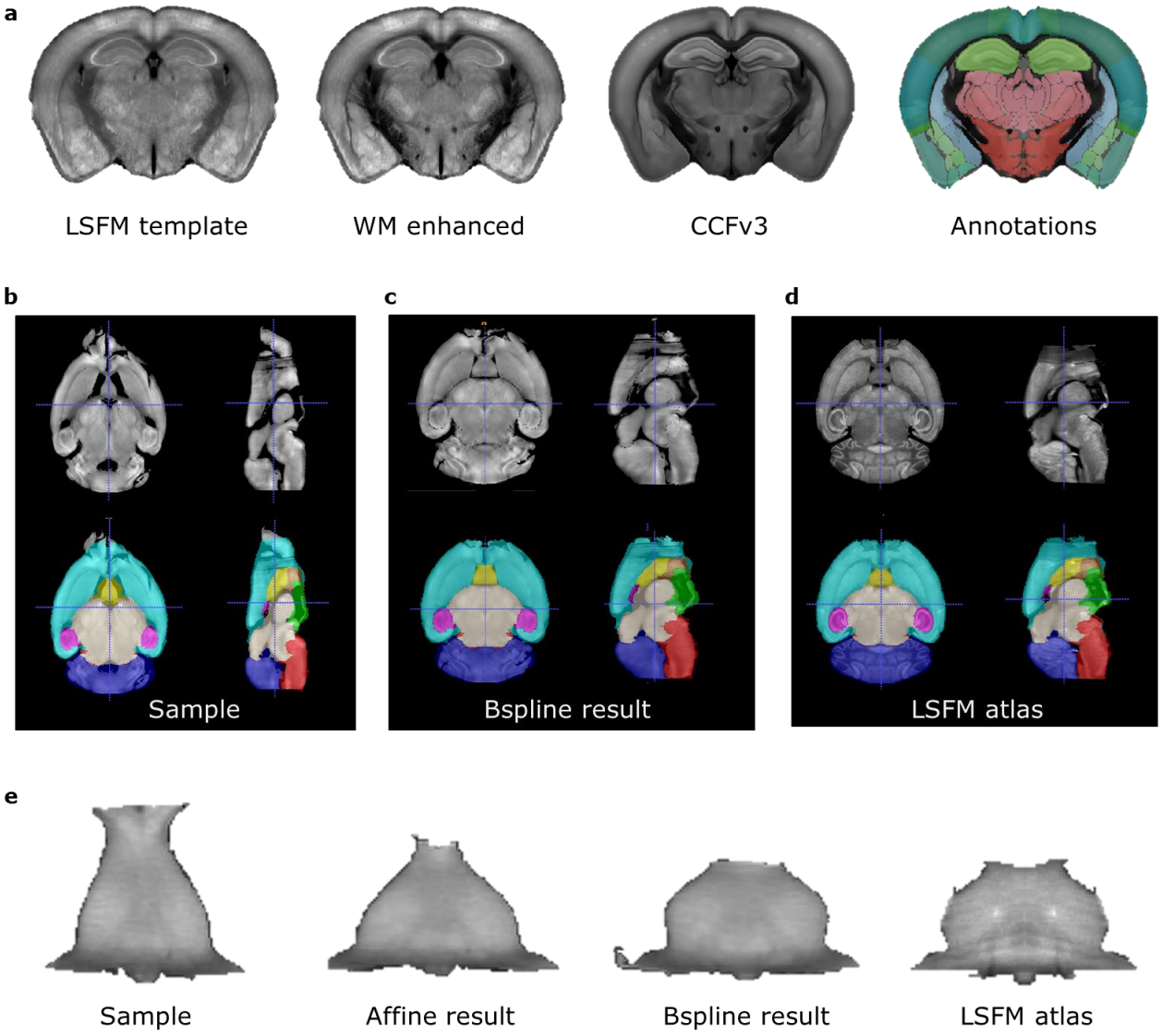

Supplement Figure 1 I Image registration. (**a**) A LSFM template was constructed from a representative C57Bl/6J male mouse by registration of the brain to the CCFv3 atlas from AIBS. A white matter (WM) enhanced version of the LSFM template was constructed to increase the alignment quality. (**b**) Example of a brain sample to be registered to the LSFM template of the integrated brain atlas. Large deformations have occurred during the tissue processing prior to imaging. (**c**) The result of aligning the sample to the LSFM atlas. The registration was performed in separate parts to mitigate the large deformations. Separate affine and b-spline registration was performed for ten larger structures, here visualized by the overlay colours in the lower part of the figure. (**d**) LSFM atlas to which the brain sample was aligned. (**e**) Example of the registration performed for one of the larger structures in the alignment between the brain sample and LSFM atlas. Images are taken from the yellow structure shown in the lower part of (**b**)-(**d**).

S2. **Accuracy of image registration**

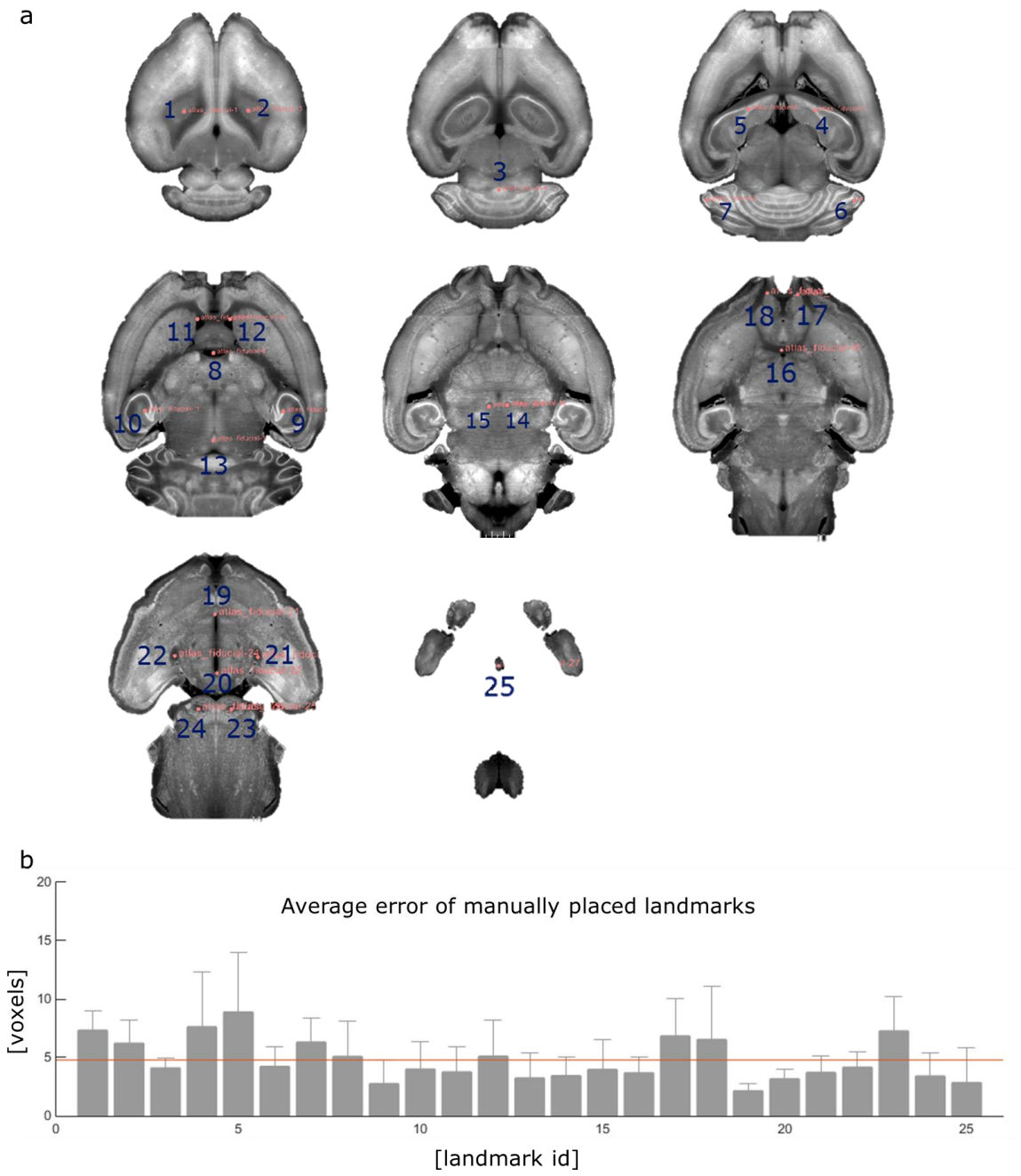

Supplement Figure 2 I Accuracy of image registration. (**a**) The accuracy of the image registration for LSFM data was evaluated by manually placing 25 landmarks distributed throughout the LSFM template and comparing to corresponding landmarks placed in five brain samples after they had been registered to the LSFM template. Bar graph showing the mean error and standard deviation (n=5). The average error between the corresponding landmarks in samples and LSFM template was approximately 5 voxels corresponding to 100 µm.

S3. **c-Fos heat maps**

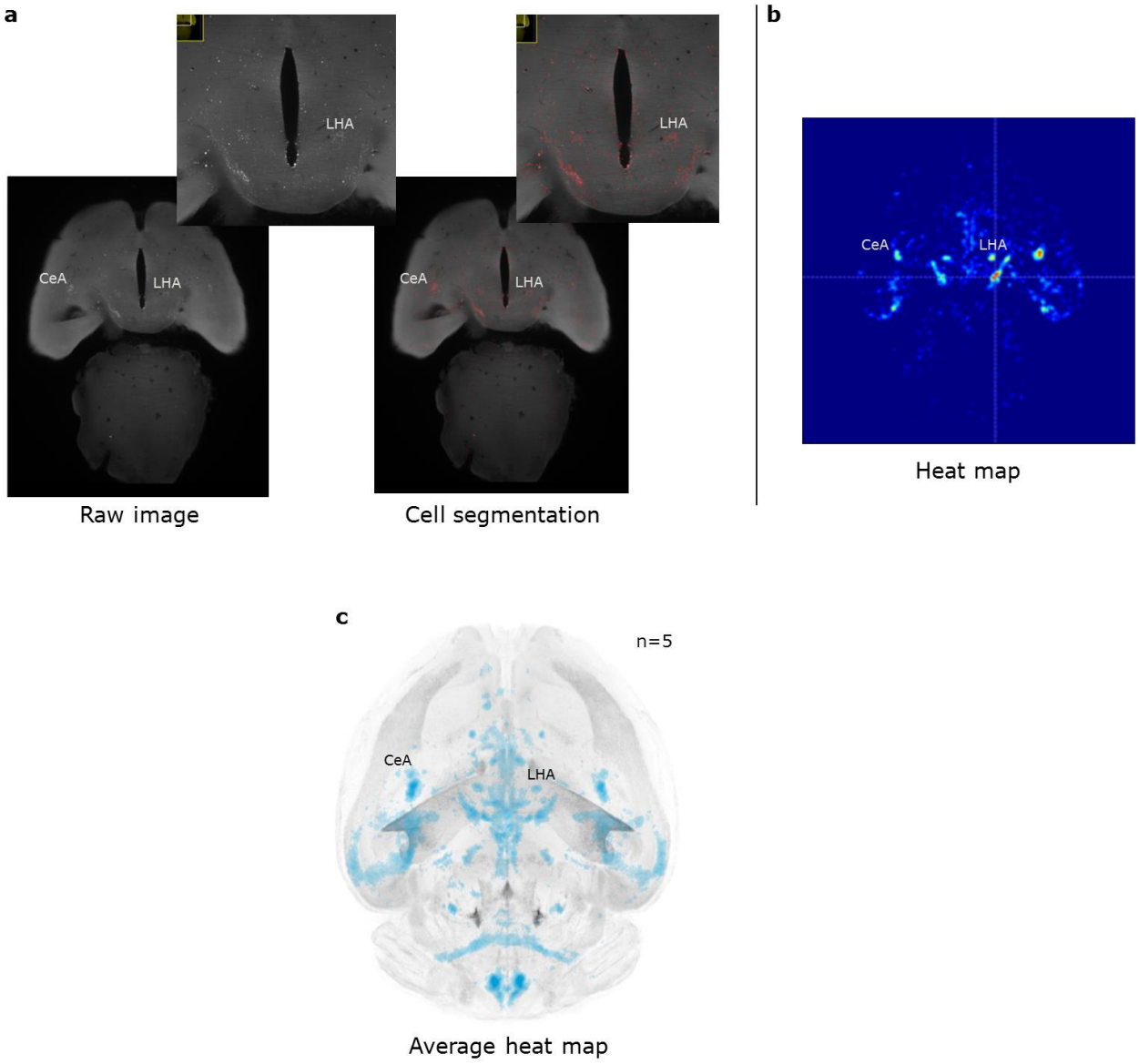

Supplement Figure 3 I c-Fos heat maps. (**a**) Raw LSFM image from a liraglutide injected mouse. The whole brain was stained for c-Fos prior to LSFM imaging. The red overlay shows the result of classifying cells positive for c-Fos. (**b**) c-Fos heatmap constructed from the image seen in (a). Red color indicates high density of c-Fos positive cells. (**c**) Maximum intensity projection image of average c-Fos signal from five animals injected with liraglutide.

Supplementary Tables

Integrated Brain Atlas for Unbiased Mapping of Nervous System Effects Following Liraglutide Treatment

- T1. **Brain region abbreviations**
- T2. **Most overlapping connectivity maps from AIBS**

T1. **Brain region abbreviations**

Abbreviation	Full name	Abbreviation	Full name
ACB	Nucleus accumbens	MM	Medial mammillary nucleus
AHN	Anterior hypothalamic nucleus	MPT	Medial pretectal area
AOB	Accessory olfactory bulb	MRN	Midbrain reticular nucleus
AP	Area postrema	MTN	Midline group of the dorsal thalamus
ARH	Arcuate hypothalamic nucleus	NI	Nucleus incertus
AUDd	Dorsal auditory area	NLL	Nucleus of the lateral lemniscus
BLA	Basolateral amygdalar nucleus	NTS	Nucleus of the solitary tract
BMA	Basomedial amygdalar nucleus	OV	Vascular organ of the lamina terminalis
BST	Bed nuclei of the stria terminalis	PAG	Periaqueductal gray
CA1	Field CA1	PB	Parabrachial nucleus
CA2	Field CA2	PCG	Pontine central gray
CA3	Field CA3	PG	Pontine gray
CEA	Central amygdalar nucleus	PH	Posterior hypothalamic nucleus
COA	Cortical amygdalar area	PSTN	Parasubthalamic nucleus
CU	Cuneate nucleus	PVH	Paraventricular hypothalamic nucleus
DG	Dentate gyrus	PVp	Periventricular hypothalamic nucleus, posterior part
DMH	Dorsomedial nucleus of the hypothalamus	PVT	Paraventricular nucleus of the thalamus
DMX	Dorsal motor nucleus of the vagus nerve	RE	Nucleus of reunions
DR	Dorsal nucleus raphe	RHP	Retrohippocampal region
ECT	Ectorhinal area	SCH	Suprachiasmatic nucleus
ECU	External cuneate nucleus	SCm	Superior colliculus, motor related
GENd	Geniculate group, dorsal thalamus	SF	Septofimbrial nucleus
GR	Gracile nucleus	SFO	Subfornical organ
IC	Inferior colliculus	SNc	Substantia nigra, compact part
LC	Locus ceruleus	SNr	Substantia nigra, reticular part
LH	Lateral habenula	SO	Supraoptic nucleus
LHA	Lateral hypothalamic area	TTd	Taenia tecta, dorsal part
LPO	Lateral preoptic area	TU	Tuberal nucleus
LRNm	Lateral reticular nucleus, magnocellular part	V4	fourth ventricle
LS	Lateral septal nucleus	VL	lateral ventricle
ME	Median eminence	VMH	Ventromedial hypothalamic nucleus
MEA	Medial amygdalar nucleus	VTA	Ventral tegmental area
MEPO	Median preoptic nucleus	ZI	Zona incerta
MH	Medial habenula		

Supplementary Table 1 I Brain region abbreviations. Full name of brain region abbreviations used in this manuscript. Brain region names follow the nomenclature of the AIBS CCFv3 atlas.

T2. **Most overlapping connectivity maps from AIBS**

Rank	Structure	Mouse line	Experiment id
1	NTS/DMX	Rasgrf2-T2A-dCre	310853453
2	CEA	C57BL/6J	112459547
3	PB	Calb2-IRES-Cre	183284388
4	PB	Slc17a6-IRES-Cre	305404551
5	GR/NTS	Gal-Cre_KI87	175816975
6	PB	Npr3-IRES2-Cre	545427588
7	PAG	Gad2-IRES-Cre	302053755
8	PB	Chat-IRES-Cre-neo	264565965
9	GR/NTS	C57BL/6J	159648854
10	AHN	Slc18a2-Cre_OZ14	301673462
11	PVT	Ntrk1-IRES-Cre	263106751
12	PB	Chat-IRES-Cre-neo	183901489
13	NTS/DMX	Pnmt-Cre	155735108
14	VMH/TU	C57BL/6J	112228391
15	CEA	Prkcd-GluCla-CFP-IRES-Cre	265945645
16	PVH	Tac1-IRES2-Cre	300888673
17	MEA	C57BL/6J	157550122
18	BST	Ppp1r17-Cre_NL146	267764292
19	NTS/DMX	Ppp1r17-Cre_NL146	268323342
20	NTS/DMX	Tac1-IRES2-Cre	180525136
21	DMH	Sim1-Cre	159222295
22	PVT	C57BL/6J	120875111
23	VMH/LHA	Erbb4-T2A-CreERT2	277854916
24	MEA	Adcyap1-2A-Cre	272819994
25	BLA/MEA	Crh-IRES-Cre_BL	277856332
26	AHN/LHA	Nos1-CreERT2	304998039
27	PVT	Grm2-Cre_MR90	183225830
28	CEA/MEA	Crh-IRES-Cre_ZJH	267152406
29	ARH	Pomc-Cre_BL	263369222
30	RE/PVH	Rasgrf2-T2A-dCre	310976160

Supplementary Table 2 I Most overlapping connectivity maps from AIBS. (**a**) List of the 30 most overlapping connectivity maps from AIBS compared to the liraglutide specific c-Fos increase following acute administration. The "Structure" column indicates the primary injection site where the virus used to trace the connections were injected. The "Mouse line" column indicates the mouse line used for the specific tracing experiment. The "Experiment id" column shows a unique AIBS id number for each experiment. All connectivity maps[6] were downloaded from the AIBS data portal.

Appendix B

Characterization of the glucagon-like peptide-1 receptor in mouse brain using a novel antibody and *in situ* hybridization

Characterization of the glucagon-like peptide-1 receptor in mouse brain using a novel antibody and *in situ* hybridization

Casper Bo Jensen[1,2], Charles Pyke[1], Morten Grønbech Rasch[1], Anders Bjorholm Dahl[2], Lotte Bjerre Knudsen[1], Anna Secher[1]

[1]Global Research, Novo Nordisk A/S, Maaloev, Denmark;

[2]Image Analysis & Computer Graphics, Department of Applied Mathematics and Computer Science , Technical University of Denmark, Kgs. Lyngby, Denmark;

Glucagon-like peptide-1 (GLP-1) is a physiological regulator of appetite and long-acting GLP-1 receptor agonists (GLP-1RA) lower food intake and bodyweight in both human and animal studies. The effects are mediated through brain GLP-1Rs, and several brain nuclei expressing the GLP-1R may be involved. To date, mapping the complete location of GLP-1R protein in the brain has been challenged by lack of good antibodies and the discrepancy between mRNA and protein especially relevant in neuronal axonal processes. Here, we present a novel and specific monoclonal GLP-1R antibody for immunohistochemistry with murine tissue and show detailed distribution of GLP-1R expression as well as mapping of GLP-1R mRNA by non-radioactive *in situ* hybridization. Semi-automated image analysis was performed to map the GLP-1R distribution to atlas plates from the Allen Institute of Brain Science (AIBS). The GLP-1R was abundantly expressed in numerous regions including the septal nucleus, the hypothalamus and the brain stem. GLP-1R protein expression was also observed on neuronal projections in brain regions devoid of any mRNA which has not been observed in earlier reports. Taken together, these findings provide new knowledge on GLP-1R expression in neuronal cell bodies and neuronal projections.

GLP-1 is a neurotransmitter produced in the brain stem, and an incretin hormone released from gut endocrine L-cells. GLP-1 was shown to have a role in central regulating of feeding in rats and in humans GLP-1 activated brain areas known to regulate food intake. (1). GLP-1 also has an important role in regulating insulin release through activation of the GLP-1R expressed on pancreatic beta cells thereby lowering blood glucose levels (2). The GLP-1R is a G_s protein–coupled receptor (GPCR) (3), and mRNA coding for the receptor is widely expressed in both rodents (4) and humans (5). Longer acting GLP-1RAs lower overall appetite (6) and bodyweight (7) through mechanisms in the brain (8, 9). In rodent models, GLP-1RAs also affect other central functions such as neuroprotection, learning and memory and has been shown to relieve symptoms in Alzheimer and Parkinson's disease models (10). A complete characterization of the localization of GLP-1Rs throughout the brain will aid to delineate GLP-1R signaling in the brain potentially involved in these functions. Although extensive mapping of the receptor mRNA has previously been conducted (11), the mapping of GLP-1R protein distribution by immunohistochemistry (IHC) has been challenged by the lack of specific GLP-1R antibodies (12). Recently, the GLP-1R distribution in the brain was characterized by use of GLP-1R reporter mice (13). Albeit extensive, potential overestimation was emphasized due to the nature of the transgene being expressed at any time in development. Using the primate specific GLP-1R monoclonal antibody (MAb 3F52) (14) we have previously described the GLP-1R distribution in the non-human primate brain (15). Here, we present an additional specific monoclonal GLP-1R antibody (MAb 7F38A2) for the use with murine tissue and show the detailed distribution of GLP-1R immunoreactivity in combination with a mapping of GLP-1R mRNA by non-radioactive *in situ* hybridization (ISH). Both antibodies have been made available through the Developmental Studies Hybridoma Bank (Department of Biology, University of Iowa, Iowa City, IA).The GLP-1R distribution was mapped by image segmentation following semi-automatic registration of the scanned histological slides to digital atlas plates from the AIBS mouse brain reference model (16, 17). IHC was performed on brain tissue derived from mice with a complete knock out of the GLP-1R (*Glp-1r*$^{-/-}$) to further validate the antibody.

Materials and Methods:

Generation of anti-mouse GLP-1 receptor antibody

GLP-1R monoclonal antibody (7F38A2 3,6mg/ml) was generated at Novo Nordisk A/S. *Glp-1r*$^{-/-}$ mice were immunized with baby hamster kidney (BHK) cells stably transfected with the mouse GLP-1R and antibodies were generated using standard hybridoma technology. The *Glp-1r*$^{-/-}$ mice were on a C57BL background and were derived from the previously described *Glp-1r*$^{-/-}$ strain (18) custom bred by Novo Nordisk A/S at Taconic. The strain is not commercially available. GLP-1R specific antibodies were identified by image based screening (ImageXpress, Molecular Devices, CA) using the BHK-mouse GLP-1R (mGLP-1R) cells used for immunization and a mock transfected BHK cell-line for counter screen. Following isolation of the 7F38A2 clone and purification of the antibody, binding to mGLP-1R was validated in a flow cytometry experiment using transiently transfected HEK-mGLP-1R and HEK mock cells. Detection was done using an allophycocyanin-labelled anti-mouse antibody (#115-136-071, Jackson Immunoresearch, PA) diluted 1:500. The 7F38A2 antibody is a mouse IgG2aκ and anti-TNP is an isotype control. For the immunostaining experiments the antibody was biotinylated using NHS-biotin (#H1759, Sigma) following the manufacturer's instructions.

The antibody is now available at http://dshb.biology.uiowa.edu/Mab-7F38?sc=9&category=-109

Animals

Male mice (C57BL/6J, and *Glp1r*$^{-/-}$) and rats (Sprague Dawley) were obtained from Taconic, Denmark and housed 5 per cage in standard, temperature controlled conditions with a 12-hour light/dark cycle. The animals had ad libitum access to water and regular chow (no. 1324, Altromin, Brogaarden) unless otherwise stated. Handling and housing of the animals were conducted in accordance with approved national regulations in Denmark which are fully compliant with internationally accepted principles for the care and use of laboratory animals, and with animal experimental licenses granted by the Danish Ministry of Justice.

Tissue preparation and sectioning

The animals were anesthetized with isoflurane and transcardially perfused with heparinized (10U/ml) saline (10 ml) followed by 10 % neutral buffered formalin (NBF) (10 ml). Brains were removed, immersed into 10 % NBF and stored at room temperature for 24 hours before being embedded into paraffin. For whole brain receptor mapping one male mouse was used, and the entire brain was sectioned at 4.5 µm intervals and all sections were collected. Additionally, two male mice (one C57BL/6J, one *Glp-1r-/-*) and one male rat (Sprague Dawley) were used for a follow up study. Section thickness was 4.5 µm.

Immunohistochemistry

For whole brain receptor mapping every 20th section was used for IHC. Paraffin sections were dewaxed and rehydrated in double distilled water. Sections were treated with 0.1 % pronase in PBS at 37°C for 10 minutes and rinsed in Tris-buffered saline (TBS). Sections were then treated with 1 % H_2O_2 in TBS for 15 minutes, washed in TBS with 0.05 % Tween (TBS-T), blocked with avidin for 10 minutes (Dako, Glostrup, Denmark), washed with TBS-T, blocked with biotin for 10 minutes (Dako, Glostrup, Denmark), washed with TBS-T, and pre-incubated with 3.2 mg/mL Poly L-Lysine, 3 % BSA bovine serum albumin, 7 % donkey serum and 3 % skimmed milk (Dako, Glostrup, Denmark) for 30 minutes. Sections were incubated overnight with primary biotinylated mouse GLP-1R antibody (MAb 7F38A2, Novo Nordisk, Måløv, Denmark) then washed three times for 10 minutes each in TBS-T, followed by treatment with Vectastain ABComplexHRP in TBS for 30 minutes and washed again three times for 10 minutes each. Sections were developed with diaminobenzidine **(**DAB^{+}) (Dako, Glostrup, Denmark) and counterstained with hematoxylin, rinsed in water, dehydrated and mounted. Sections for the follow up study were stained with similar protocol with the exception of an additional Tyramide Signal Amplification (TSA) step and treatment with Vectastain ABComplexHRP, following primary antibody incubation which this time was reduced to two hours. All images were obtained using Hamamatsu NanoZoomer-XR. In addition, the staining protocol has been optimized for automatic staining applying the Ventana Discovery Ultra staining module. For details on this protocol please refer to the supplementary material.

***In situ* hybridization**

ISH was performed using the RNAscope platform (19, 20) on neighboring sections to the sections used for whole brain IHC mapping. The staining was performed using a Ventana Discovery XT system (Ventana MedicalSystems, Inc., Tucson, AZ) with RNAscope VS FFPE RED reagent kit (cat# 320610 from Advanced Cell Diagnostics, Hayward, CA). Briefly, the VS RNAscope protocol was used with the following pretreatment conditions: boiling for 2 minutes and pretreatment 2+3 steps for 4 minutes each with probes for bacterial DapB (negative control, cat. no. 310048), and mouse GLP-1R (cat. no. 415896). Images were obtained using Hamamatsu NanoZoomer-XR.

To validate the signal obtained for GLP-1R mRNA, another mouse GLP-1R probe (no. 415906) non-overlapping in sequence with probe no. 415896 was used on adjacent sagittal mouse brain sections. The signals obtained with both probes showed a complete overlap (data not shown).

Image analysis and atlas plate generation

Image segmentation of the IHC and ISH slide scanner images were performed using a multinomial regression classifier trained on a constructed mosaic image for each staining type. The r,g,b values of the images were used as input features. Prior to segmentation each IHC/ISH image pair was registered to a digital atlas plate obtained from the AIBS mouse brain reference model (16, 17). The specific atlas plates were manually selected from a collection of 528 plates. The image registration was performed in a coarse to fine manner with an affine transformation followed by non-linear b-spline transformation using sum of squared difference as similarity measure. All registrations were computed using Elastix (21). The final atlas plates were constructed by summing segmented signal inside a square mask moving across the registered images. A blue circle (IHC) or a red square (ISH) was drawn on the atlas plate if positive signal was detected. The diameter of the marker was based on the signal count applying a logarithmic scale to show both weak and strong signals. Following the automatic atlas plate generation manual corrections were performed in regions where the automatic image registration was not sufficiently accurate.

Table 1. Antibodies used

Peptide/Protein Target	Manufacturer, Catalog #, and/or Name of Individual Providing the Antibody	Species Raised in; Monoclonal or Polyclonal	Dilution Used	RRID
GLP-1R	Developmental Studies Hybridoma Bank, Mab 7F38	Mouse, Monoclonal	1:720	AB_2618101

Results

Antibody specificity

IHC staining with the GLP-1R antibody revealed high intensity staining with good resolution and low background (Figure 1). The antibody was specific for GLP-1Rs expressed in peripheral organs such as the Brunner's gland (Figure 1, A-B) and further for mouse (Figure 1, C-F) and rat (Figure 1, G-H) brain. The expressional profile of GLP-1R was evaluated throughout the entire mouse brain, and this expression was confirmed in select regions in the rat brain in hypothalamus and brain stem showing correspondence between the two species in the regions investigated. However, some discrepancies existed between mouse and rat where GLP-1R expression could be observed in mouse lateral habenula, nucleus accumbens and in the nucleus of the lateral olfactory tract/cortical amygdalar area which was absent in rat brain (data not shown). Validation of the antibody has further been performed for GLP-1Rs in pancreas (22), kidney (23) and other peripheral GLP-1R expressing organs such as GI tract, lung and thyroid (data not shown).

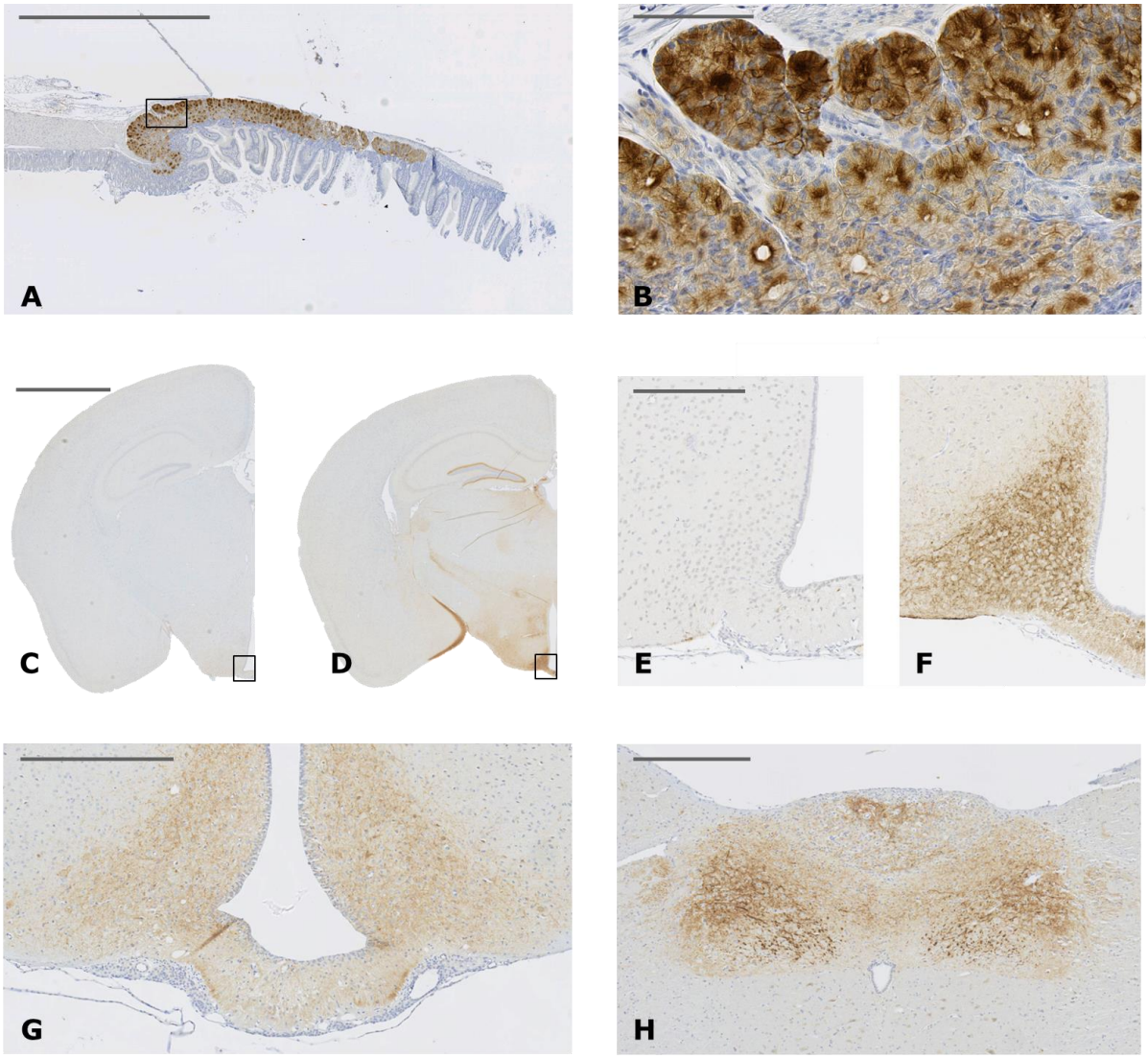

Figure 1. GLP-1R IHC with antibody Mab 7F38A2 on paraffin-embedded mouse Brunner's Gland (A–B) and mouse brain (C-F). B, High magnification of the solid-line box in A. E and F, Magnifications of solid-line boxed areas in C and D, respectively. C and E are from a *Glp-1r*$^{-/-}$ mouse while D and F are from a C57BL/6J mouse. GLP-1R IHC with antibody Mab 7F38A2 on paraffin-embedded rat brain (G–H). G, High magnification image of the hypothalamus showing positive staining in arcuate hypothalamic nucleus and median eminence. H, High magnification image showing positive staining in area postrema, dorsal motor nucleus of the vagus nerve and nucleus of the solitary tract. Scale bar in A corresponds to 2000 um. Scale bar in B corresponds to 100 um. Scale bar in C-D corresponds to 2000 um. Scale bar in E-F corresponds to 250 um. Scale bar in G corresponds to 500 um. Scale bar in H corresponds to 500 um.

Distribution of GLP-1R

Overall, GLP-1R protein and mRNA co-localized in most regions, however, some discrepancies was found such as in the posterior hippocampus, median eminence and terminal field of accessory olfactory bulb projections. The findings are summarized in Table 2 and on the atlas plate overlays (Figure 2).

Telencephalon. In agreement with previous reports, GLP-1R protein positive cells were identified in the olfactory bulb, amygdala, dentate gyrus, septal nucleus, preoptic area, septofimbrial nucleus, triangular nucleus of septum, tenia tecta, vascular organ of the laminae terminalis, nucleus accumbens and bed nucleus of stria terminalis. Furthermore, protein was observed in the subfornical organ and in the terminal field of accessory olfactory bulb projections (the latter is included in the cortical amygdalar area in Table 2) where mRNA expression was absent (Table 2). Especially in those regions where protein expression differed from mRNA expression, the specificity of the antibody was further validated by antibody staining on brain sections from *Glp-1r* $^{-/-}$ mice. The data from the *Glp-1r*$^{-/-}$ mice showed complete absence of GLP-1R immunoreactivity, further establishing this antibody as specific towards the GLP-1R and confirming the presence of GLP-1R protein in these regions (Figure 3).

Diencephalon. In the diencephalon GLP-1R protein and mRNA was observed in cells in zona incerta, tuberal nucleus, peripeduncular nucleus, and in hypothalamus in the arcuate nucleus, dorsomedial hypothalamic nucleus, lateral hypothalamic nucleus, paraventricular hypothalamic nucleus and supraoptic nucleus. Furthermore, GLP-1R protein was observed in median eminence as fibers only with no mRNA expression. The same pattern of presence of GLP-1R protein in the absence of mRNA expression was observed in the geniculate group of thalamus, posterior hypothalamic nucleus, habenula, and retrochiasmatic area (Table 2). When comparing mRNA expression reported by AIBS (http://www.brain-map.org/) with data obtained in the present study several areas expressing GLP-1R mRNA in the AIBS atlas were negative in the present study (Table 2).

Mesencephalon. GLP-1R was observed in the anterior pretectal nucleus, medial and posterior pretectal area, the periaqueductal gray, and in the substantia nigra. GLP-1R protein was also observed in the motor related part of superior colliculus whereas mRNA expression could be observed in both the motor related and the sensory related part of superior colliculus. Further discrepancies were observed in the dorsal raphe, the medial mammillary nucleus, the midbrain reticular nucleus and the ventral spinocerebellar tract where receptor was observed as protein on fibers only, lacking mRNA expression.

Pons. In pons, GLP-1R protein and mRNA expression could be observed in the pontine grey, the parabrachial nucleus and the principal sensory nucleus of the trigeminal. Very few brain regions were positive for both protein and mRNA and only protein was observed in the nucleus incertus, nucleus of the lateral lemniscus, and the superior olivary complex whereas only mRNA was observed in the pontine reticular nucleus.

Medulla. In Medulla, GLP-1R was observed in the area postrema, cuneate nucleus, inferior olivary complex, lateral reticular nucleus, nucleus tractus solitarus, medial vestibular nucleus, and the spinal nucleus of the trigeminal. GLP-1R protein but not mRNA was observed in the dorsal motor nucleus of the vagus nerve and in flocculus, residing in cerebellum, whereas mRNA was evident in nucleus ambiguus, and in the reticular nucleus.

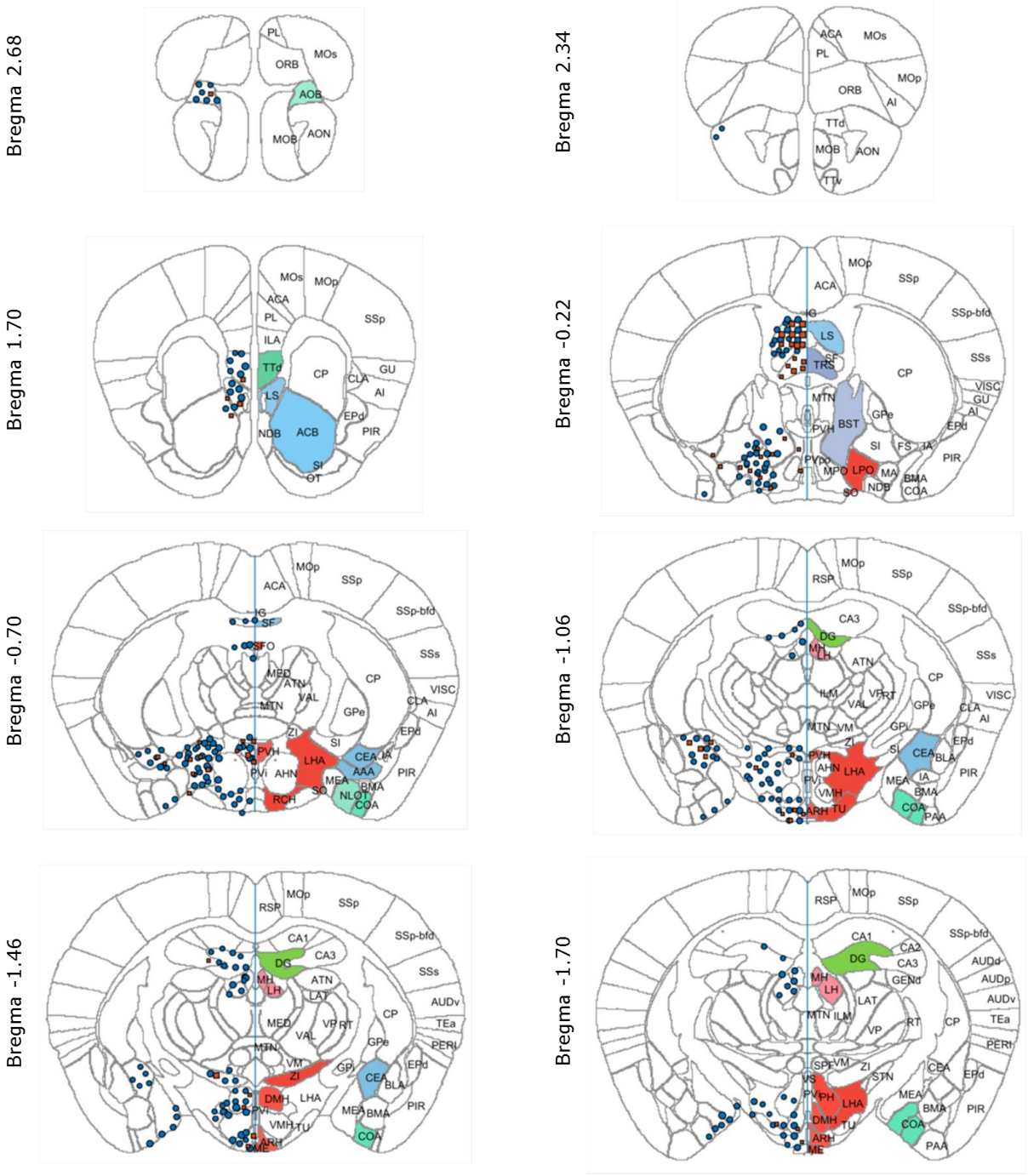

Figure 2. Atlas plates showing distribution of signals for mouse GLP-1R *ISH* (red squares) and GLP-1R IHC (blue circles). The distribution is overlaid onto digital atlas plates constructed from the AIBS mouse brain atlas. The distribution of GLP-1R mRNA and protein are indicated on the left half of the atlas plates and brain regions with positive staining for either GLP-1R mRNA or protein are highlighted with a solid color on the right half of the atlas plates. Brain region abbreviations follow the nomenclature of the AIBS mouse brain reference atlas which can be found at: http://atlas.brain-map.org/

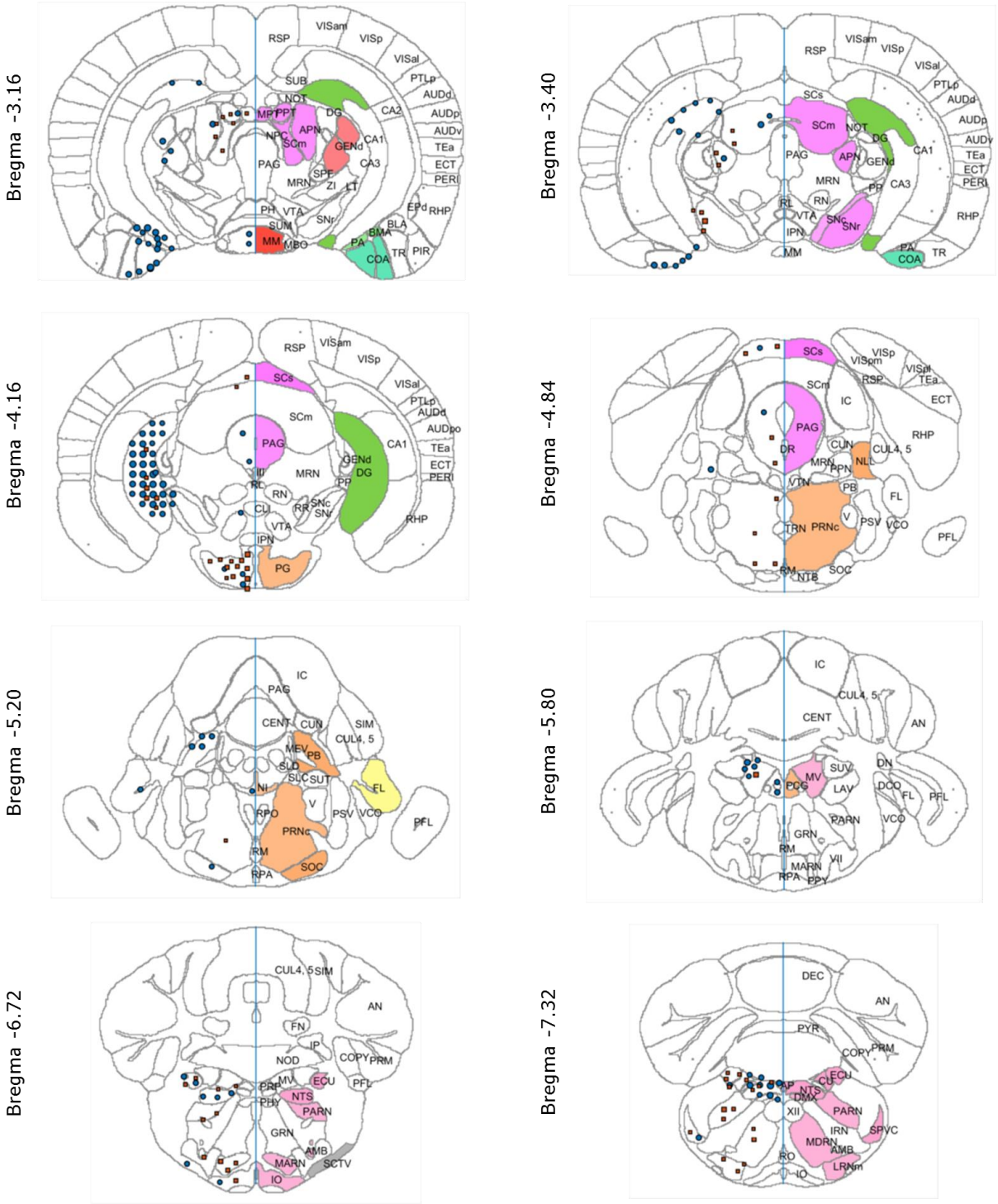

Figure 2 (continued). Atlas plates showing distribution of signals for mouse GLP-1R *ISH* (red squares) and GLP-1R IHC (blue circles). The distribution is overlaid onto digital atlas plates constructed from the AIBS mouse brain atlas. The distribution of GLP-1R mRNA and protein are indicated on the left half of the atlas plates and brain regions with positive staining for either GLP-1R mRNA or protein are highlighted with a solid color on the right half of the atlas plates. Brain region abbreviations follow the nomenclature of the AIBS mouse brain reference atlas which can be found at: http://atlas.brain-map.org/

Table 2. Summary of GLP-1R (IHC and ISH) location in C57BL/6J mouse brain and comparison to external references

Structure		Area	Protein	mRNA	Cork et al (13) (protein)	AIBS (mRNA)
Telencephalon	AOB	Accessory olfactory bulb	+	+	+	+
	BMA	Basomedial amygdalar nucleus	+	-	+	+
	CeA	Central amygdala	+	+	+	+
	CeA/AAA	Central amygdala/Anterior amygdalar area	+	+	+	+
	COA	Cortical amygdalar area	+	-	+	+
	DG	Dentate gurys	+	+	+	+
	LPO	Lateral preoptic area	+	+	+	+
	LS	Lateral septal nucleus	+	+	+	+
	NLOT/COA	Nucleus of the lateral olfactory tract/Cortical amygdalar area	+	-	+	+
	PA	Posterior amygdalar nucleus	+	-	+	+
	SF	Septofimbrial nucleus	+	+	NA	+
	SFO	Subfornical organ	+	+	+	+
	TRS	Triangular nucleus of septum	-	+	NA	+
	TT	Tenia tecta	+	+	+	+
	OV	Vascular organ of the laminae terminalis	+	NA	+	NA
	ACB	Nucleus accumbens	+	+	+	+
	BST	Bed nucleus of stria terminalis	+	+	+	+
Diencephalon	ARH	Arcuate hypothalamic nucleus	+	+	+	+
	DMH	Dorsomedial hypothalamic nucleus	+	+	+	+
	GENd	Geniculate group, dorsal thalamus	+	-	+	+
	Hb	Habenula	+	-	+	+
	LHA	Lateral hypothalamic nucleus	+	+	+	+
	ME	Median eminence	+	-	NA	+
	PH	Posterior hypothalamic nucleus	+	-	+	+
	PP	Peripeduncular nucleus	+	+	NA	+
	PVH	Paraventricular hypothalamic nucleus	+	+	+	+
	RCH	Retrochiasmatic area	+	-	+	+
	SO	Supraoptic nucleus	+	+	NA	+
	TU	Tuberal nucleus	+	+	NA	+
	ZI	Zona incerta	+	+	+	+
Mesencephalon	APN	Anterior pretectal nucleus	+	+	+	+
	DR	Dorsal raphe	+	-	NA	+
	MM	Medial mammillary nucleus	+	-	+	+
	MPT	Medial pretectal area	+	+	+	+
	MRN	Midbrain reticular nucleus	+	-	NA	+
	PAG	Periaqueductal gray	+	+	+	+
	PPT	Posterior pretectal area	+	+	+	+
	SCs	Superior colliculus, sensory related	-	+	NA	+
	SCm	Superior colliculus, motor related	+	+	NA	+
	SCTV	ventral spinocerebellar tract	+	-	NA	+

	SNr	Substantia nigra, reticular part	+	+	NA	+
	SNc	Substantia nigra, compact part	+	+	NA	+
Pons	NI	Nucleus incertus	+	-	NA	+
	NLL	Nucleus of the lateral lemniscus	+	-	NA	+
	PB	Parabrachial nucleus	+	+	NA	+
	PCG	Pontine central gray	+	-	NA	+
	PG	Pontine gray	+	+	NA	+
	PRNc	Pontine reticular nucleus, caudal part	-	+	NA	+
	PRNr	Pontine reticular nucleus	-	+	NA	+
	PSV	Principal sensory nucleus of the trigeminal	+	+	NA	+
	SOC	Superior olivary complex	+	-	NA	+
Medulla	AMB	Nucleus ambiguus	-	+	NA	+
	AP	Area postrema	+	+	+	+
	CU	Cuneate nucleus	+	+	NA	+
	DMX	Dorsal motor nucleus of the vagus nerve	+	-	NA	+
	ECU	External cuneate nucleus	+	+	NA	+
	FL	Flocculus (cerebellum)	+	-	NA	+
	IO	Inferior olivary complex	+	+	+	+
	LRNm	Lateral reticular nucleus, magnocellular part	+	+	NA	+
	MARN	Magnocellular reticular nucleus	-	+	NA	+
	MDRN	Medullary reticular nucleus	-	+	NA	+
	MV	Medial vestibular nucleus	+	+	NA	+
	NTS	Nucleus tractus solitarus	+	+	+	+
	PARN	Parvicellular reticular nucleus	-	+	NA	+
	SPVC	Spinal nucleus of the trigeminal, caudal part	+	+	NA	+

Presence (+) or absence (-) of GLP-1R protein and mRNA in mouse brain. The two right columns indicate whether GLP-1R was observed as protein (Cork et al) or mRNA (AIBS). NA: not assessed/reported.

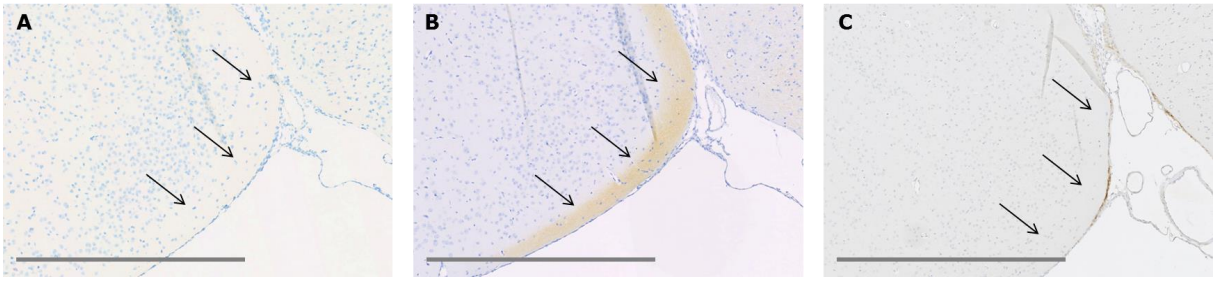

Figure 3. High magnification images of adjacent sections of C57BL/6J mouse brain tissue focusing on terminal field of accessory olfactory bulb projections (A-B). A, Mouse GLP-1R *ISH* showing lack of signal. B, GLP-1R IHC with antibody Mab 7F38A2 showing positive staining. C, GLP-1R IHC with antibody Mab 7F38A2 on a corresponding section from a *Glp1r*$^{-/-}$ mouse brain showing negative staining. Scale bars correspond to 400 um.

Discussion

The reliable detection of the GLP-1R expression in tissues using IHC has been hampered by a lack of specific antibodies thus limiting well validated histological mapping studies to the detection of GLP-1R mRNA using ISH (12, 24, 25) and protein using *in situ* ligand binding with low spatial resolution (26). In this study an extensive mapping of GLP-1R mRNA and protein expression in the mouse brain is reported. For localization of GLP-1R protein a monoclonal GLP-1R antibody was used which is highly specific for murine GLP-1R as demonstrated by the complete absence of reactivity in mice lacking the GLP-1R. The localization of GLP-1R protein was combined with detection of GLP-1R mRNA on adjacent sections using non-radioactive ISH, enabling a higher accuracy for anatomical localization compared to a radioactivity based approach. The expression patterns observed showed good alignment between protein and mRNA expression but also revealed some regions only positive for GLP-1R protein and encompassing axonal projections. This is a well described phenomenon in the brain where protein and gene expression do not always correlate (27, 28, 29), possibly in situations where protein can be transported away from the nuclear processing site along the axonal processes. This phenomenon necessitates caution when interpreting potential GLP-1 interacting brain regions and neurons based on receptor mRNA expression alone, as such data will underestimate the number of GLP-1 binding sites. The distribution of GLP-1R protein in the mouse brain has previously been described using a transgene *Glp-1r* reporter mouse (13). When comparing GLP-1R protein expression detected using the antibody in the present study with the study by Cork et al (13) there is a high level of agreement with a few exceptions where some positive regions were seen using IHC but not reported by Cork et al. Of note, several of these regions were regions lacking mRNA expression, indicating the presence of protein exclusively on projections and terminals. Thus, compared to the transgene *Glp-1r* reporter mouse model, antibody detection with IHC represents a superior method to visualize axonal projection throughout the brain. Interestingly, the concern for artefactual overexpression of GLP-1R in the *Glp-1r* reporter mouse as a result of accumulated gene transcription during embryogenesis does not seem to be a problem in the case of the GLP-1R, as all regions reported positive in the reporter mouse were also seen with antibody staining.

Comparing mRNA expression in the present study to that reported by AIBS revealed several areas where mRNA was reported to be present by AIBS (e.g. nucleus of the trapezoid body, septohippocampal nucleus, dorsal peduncular area, and tegmental reticular nucleus) but not observed in our study (and hence not included in Table 2). These inconsistencies are likely due to a higher specificity of the RNAscope ISH platform used here as demonstrated by the full overlap of signals obtained with two non-overlapping probes for GLP-1R. Another explanation could be the more extensive sampling of the mouse brain in studies reported by AIBS potentially revealing sub nuclei with limited GLP-1R expression that was not picked up in this study.

To verify that the antibody could also be applied to rat tissue, select sections from rat brain were stained and examined. Although there was a good agreement with respect to localization of the GLP-1R between mouse and rat on sections with hypothalamus and brain stem, it must be emphasized that the entire rat brain was not analyzed and a discrepancy between mouse and rat in GLP-1R localization in the brain was detected in some regions. In general more GLP-1R protein was observed in the mouse brain compared to the rat brain. A large part of the additional GLP-1R protein was seen in mouse axonal processes such as in medial habenula and cortical amygdalar area which were absent in the rat. Thus, to fully characterize the GLP-1R in rat brain a full mapping is needed rather than assuming complete correspondence between species.

Considering the relative small fraction of neurons in the hindbrain that produce GLP-1, a remarkable abundance of GLP-1Rs were found to be expressed throughout the brain indicating potential diverse actions of this neurotransmitter. Indeed, central GLP-1 activity has been reported to affect functions such as feeding behavior, body weight and temperature, malaise, fluid homeostasis, stress response, and learning and memory (30, 31). One of the most abundant GLP-1R populations was found in the caudal division of the lateral septal nucleus a population that is little understood with respect to GLP-1 actions. The caudal part of lateral septal nucleus has been characterized as

abundant in somatostatin neurons which has been shown to act inhibitory in septal nucleus (32, 33). Further building on this inhibitory mechanism, other studies have suggested that GLP-1R expressing neurons in LS are GABA'ergic and connected to GLP-1 actions on behaviors associated with reward (34, 35). Septal projections are extensive and include innervation of hypothalamus, supramammilary nucleus, hippocampus, thalamus, and ventral tegmental area (36). Thus the involvement in reward signaling may only be a one GLP-1 mediated behavior initialized from this area.

Another area with high expression of GLP-1R positive fibers was in the dentate gyrus which is the principal input to the rest of the hippocampus forming the "tri-synaptic hippocampal circuit" associated with episodic memory consolidation and formation (37). The dentate gyrus is capable of generating new granule cells in the adult brain (38, 39), which has been linked to memory formation and maintenance as well as neuroprotection (40, 41). Hence, GLP-1R expression in this area could be coupled to some of the beneficial effects reported with GLP-1 regulation of memory and Alzheimer's disease (42) and neuroprotection (31).

A high expression of GLP-1R was also identified on fibers projecting to the median eminence. The median eminence is usually associated with the integration of the hypothalamic pituitary axis serving as an area of release from paraventricular hypothalamic neurons to the bloodstream. On top of this, literature suggests the median eminence to be a site for uptake of peripheral peptides such as leptin and ghrelin from the blood (43, 44) through receptor specific uptake; this could be extended to include GLP-1RAs. Indeed all circumventricular organs including the median eminence have a high expression of GLP-1R suggesting interaction with peripheral GLP-1 in these regions.

In summary, we report here a full mapping of GLP-1R protein and mRNA in the mouse brain using IHC with a specific monoclonal antibody and ISH, respectively. The strength of using a fully validated and specific antibody is emphasized by the ability to detect GLP-1R protein in regions devoid of mRNA and in neuronal projections where it was not observed using a transgenic reporter system.

Acknowledgements

The technical assistance of Pia G. Mortensen, Bettina Brandrup and Suzanne K. Møller is gratefully acknowledged.

Address all correspondence and requests for reprints to: Lotte Bjerre Knudsen, Novo Nordisk, Novo Nordisk Park, DK-2760 Maaloev, Denmark. E-mail: lbkn@novonordisk.com.

Disclosure Summary: C.J, C.P, M.G, L.B.K and A.S are full-time employees of Novo Nordisk A/S, which markets liraglutide for the treatment of diabetes and weight management, and hold minor stock portions as part of an employee offering program. A.B.D has nothing to disclose.

References

1. Turton, M. D., et al. "A role for glucagon-like peptide-1 in the central regulation of feeding." Nature 379.6560 (1996): 69.

2. Zander, Mette, et al. "Effect of 6-week course of glucagon-like peptide 1 on glycaemic control, insulin sensitivity, and β-cell function in type 2 diabetes: a parallel-group study." The Lancet 359.9309 (2002): 824-830.

3. Brubaker, P. L., and D. J. Drucker. "Structure-function of the glucagon receptor family of G protein-coupled receptors: the glucagon, GIP, GLP-1, and GLP-2 receptors." Receptors and Channels 8.3-4 (2002): 179-188.

4. Campos, ROBERT V., YING C. Lee, and D. J. Drucker. "Divergent tissue-specific and developmental expression of receptors for glucagon and glucagon-like peptide-1 in the mouse." Endocrinology 134.5 (1994): 2156-2164.

5. Wei, Yang, and Svetlana Mojsov. "Tissue-specific expression of the human receptor for glucagon-like peptide-I: brain, heart and pancreatic forms have the same deduced amino acid sequences." FEBS letters 358.3 (1995): 219-224.

6. Van Can, J., et al. "Effects of the once-daily GLP-1 analog liraglutide on gastric emptying, glycemic parameters, appetite and energy metabolism in obese, non-diabetic adults." International Journal of Obesity 38.6 (2014): 784-793.

7. O'Neil, Patrick M., et al. "EFFECTS OF LIRAGLUTIDE 3.0 MG ON WEIGHT AND RISK FACTORS IN HISPANIC VERSUS NON-HIPANIC POPULATIONS: SUBGROUP ANALYSIS FROM SCALE RANDOMIZED TRIALS." Endocrine Practice 22.11 (2016): 1277-1287.

8. Secher, Anna, et al. "The arcuate nucleus mediates GLP-1 receptor agonist liraglutide-dependent weight loss." The Journal of clinical investigation 124.10 (2014): 4473-4488.

9. Sisley, Stephanie, et al. "Neuronal GLP1R mediates liraglutide's anorectic but not glucose-lowering effect." The Journal of clinical investigation 124.6 (2014): 2456-2463.

10. McClean, Paula L., et al. "The diabetes drug liraglutide prevents degenerative processes in a mouse model of Alzheimer's disease." Journal of Neuroscience 31.17 (2011): 6587-6594.

11. Merchenthaler, Istvan, Malcolm Lane, and Paul Shughrue. "Distribution of pre-pro-glucagon and glucagon-like peptide-1 receptor messenger RNAs in the rat central nervous system." Journal of Comparative Neurology 403.2 (1999): 261-280.

12. Pyke, Charles, and Lotte Bjerre Knudsen. "The glucagon-like peptide-1 receptor—or not?" (2013): 4-8.

13. Cork, Simon C., et al. "Distribution and characterisation of glucagon-like peptide-1 receptor expressing cells in the mouse brain." Molecular metabolism 4.10 (2015): 718-731.

14. Pyke, Charles, et al. "GLP-1 receptor localization in monkey and human tissue: novel distribution revealed with extensively validated monoclonal antibody." Endocrinology 155.4 (2014): 1280-1290.

15. Heppner, Kristy M., et al. "Expression and distribution of glucagon-like peptide-1 receptor mRNA, protein and binding in the male nonhuman primate (Macaca mulatta) brain." Endocrinology 156.1 (2014): 255-267.

16. Oh, Seung Wook, et al. "A mesoscale connectome of the mouse brain." Nature 508.7495 (2014): 207-214.

17. Lein, Ed S., et al. "Genome-wide atlas of gene expression in the adult mouse brain." Nature 445.7124 (2007): 168-176.

18. Scrocchi, L. A., et al. "Glucose intolerance but normal satiety in mice with a null mutation in the glucagon-like peptide 1 receptor gene." Nature medicine 2.11 (1996): 1254-1258.

19. Wang, Fay, et al. "RNAscope: a novel in situ RNA analysis platform for formalin-fixed, paraffin-embedded tissues." The Journal of Molecular Diagnostics 14.1 (2012): 22-29.

20. Anderson, Courtney M., et al. "Fully Automated RNAscope In Situ Hybridization Assays for Formalin-Fixed Paraffin-Embedded Cells and Tissues." Journal of cellular biochemistry (2016).

21. Klein, Stefan, et al. "Elastix: a toolbox for intensity-based medical image registration." IEEE transactions on medical imaging 29.1 (2010): 196-205.

22. Lehtonen, Janne, et al. "Beta cell specific probing with fluorescent exendin-4 is progressively reduced in type 2 diabetic mouse models." Islets 7.6 (2015): e1137415.

23. Jensen, Elisa P., et al. "Activation of GLP-1 receptors on vascular smooth muscle cells reduces the autoregulatory response in afferent arterioles and increases renal blood flow." American Journal of Physiology-Renal Physiology 308.8 (2015): F867-F877.

24. Panjwani, Naim, et al. "GLP-1 receptor activation indirectly reduces hepatic lipid accumulation but does not attenuate development of atherosclerosis in diabetic male ApoE−/− mice." Endocrinology 154.1 (2013): 127-139.

25. Drucker, Daniel J. "Never waste a good crisis: confronting reproducibility in translational research." Cell metabolism 24.3 (2016): 348-360.

26. Göke, Rüdiger, et al. "Distribution of GLP-1 binding sites in the rat brain: evidence that exendin-4 is a ligand of brain GLP-1 binding sites." European Journal of Neuroscience 7.11 (1995): 2294-2300.

27. Komorowski, A., et al. "Association of Protein Distribution and Gene Expression Revealed by PET and Post-Mortem Quantification in the Serotonergic System of the Human Brain." Cerebral Cortex 27.1 (2017): 117-130.

28. Fortelny, Nikolaus, et al. "Can we predict protein from mRNA levels?." Nature 547.7664 (2017): E19.

29. Liu, Yansheng, Andreas Beyer, and Ruedi Aebersold. "On the dependency of cellular protein levels on mRNA abundance." Cell 165.3 (2016): 535-550.

30. Vrang, Niels, and Philip Just Larsen. "Preproglucagon derived peptides GLP-1, GLP-2 and oxyntomodulin in the CNS: role of peripherally secreted and centrally produced peptides." Progress in neurobiology 92.3 (2010): 442-462.

31. During, Matthew J., et al. "Glucagon-like peptide-1 receptor is involved in learning and neuroprotection." Nature medicine 9.9 (2003): 1173-1179.

32. Risold, P. Y., and L. W. Swanson. "Chemoarchitecture of the rat lateral septal nucleus." Brain research reviews 24.2 (1997): 91-113.

33. Twery, Michael J., and Joel P. Gallagher. "Somatostatin hyperpolarizes neurons and inhibits spontaneous activity in the rat dorsolateral septal nucleus." Brain research 497.2 (1989): 315-324.

34. Harasta, Anne E., et al. "Septal glucagon-like peptide 1 receptor expression determines suppression of cocaine-induced behavior." Neuropsychopharmacology 40.8 (2015): 1969-1978.

35. Reddy, I. A., et al. "Glucagon-like peptide 1 receptor activation regulates cocaine actions and dopamine homeostasis in the lateral septum by decreasing arachidonic acid levels." Translational psychiatry 6.5 (2016): e809.

36. Risold, P. Y., and L. W. Swanson. "Connections of the rat lateral septal complex." Brain research reviews 24.2 (1997): 115-195.

37. Amaral, D. G., and M. P. Witter. "The three-dimensional organization of the hippocampal formation: a review of anatomical data." Neuroscience 31.3 (1989): 571-591.

38. Ming, Guo-li, and Hongjun Song. "Adult neurogenesis in the mammalian central nervous system." Annu. Rev. Neurosci. 28 (2005): 223-250.

39. Cameron, Heather A., and Ronald DG Mckay. "Adult neurogenesis produces a large pool of new granule cells in the dentate gyrus." Journal of Comparative Neurology 435.4 (2001): 406-417.

40. Kitamura, Takashi, et al. "Adult neurogenesis modulates the hippocampus-dependent period of associative fear memory." Cell 139.4 (2009): 814-827.

41. Madroñal, Noelia, et al. "Rapid erasure of hippocampal memory following inhibition of dentate gyrus granule cells." Nature communications 7 (2016).

42. McClean, Paula L., et al. "The diabetes drug liraglutide prevents degenerative processes in a mouse model of Alzheimer's disease." Journal of Neuroscience 31.17 (2011): 6587-6594.

43. Schaeffer, Marie, et al. "Rapid sensing of circulating ghrelin by hypothalamic appetite-modifying neurons." Proceedings of the National Academy of Sciences 110.4 (2013): 1512-1517.

44. Balland, Eglantine, et al. "Hypothalamic tanycytes are an ERK-gated conduit for leptin into the brain." Cell metabolism 19.2 (2014): 293-301.

Supplementary material – Automated (Ventana) protocol for IHC detection with MAb clone 7F38

Name	Code no.	Firma
Reaction buffer	05353955001	Roche
Discovery wash	07311079001	Roche
LCS ultra	05424534001	Roche
Discovery Inhibitor	760-4840	Roche
Discovery CC1	950-224	Roche
Protease 3	760-2020	Roche
Rb-Glp1r-7f38	0180-0000-0233-1B	Novo Nordisk A/S
Chromogene Purple	760-229	Roche
Hematoxylin	790-2208	Roche
Blueing reagent	760-2037	Roche
Rb-HQ	760-4818	Roche
Cromomap DAB	760-159	Roche
a-HQ_HRP	760-4820	Roche
TNB(blocking reagent)	FP1012	Perkin Elmer
TBS-buffer 10X pH 7,4	AMPQ40829.5000	Ampliqon

Deparaffinization 70°C, 3 cycles of 8 min each.
Pretreatment, enzyme, Protease 3 at 37°C for 16min.
Inhibitor, Discovery Inhibitor for 12 min.
Antibodyblocking, 0,5% TNB for 28 min.
Antibody, GLP1R 7F38 1µg/ml in TBS-buffer at 37°C for 60min.
Linking Antibody (2.nd ab) , Anti-RabbitHQ, at 37°C for 24min.
Enzyme Conjugate, Anti-HQ HRP, 16 min.
DAB, time pre-set by roche-not adjustible.
Counterstain, Hematoxylin II, for 8 min.
Bluing reagent, for 4 min.

Protocol Summary

Procedure: RUO DISCOVERY Universal (v0.00.0320)

Discovery ULTRA Staining Module

Ventana Medical Systems, Inc., 1910 Innovation Park Drive Tucson, Arizona USA

Protocol No	Protocol Name	Creation Date
9	Rb-GLP1r-7f38 ab#7	06/13/2017

1 First Sequence [Selected]
2 Deparaffinization [Selected]
3 Warmup Slide to [70 Deg C], and Incubate for [8 Minutes] (Cycle 1)
4 Incubate for [8 Minutes] (Cycle 2)
5 Incubate for [8 Minutes] (Cycle 3)
6 Pretreatment [Selected]
7 Enzyme [Selected]
8 Use RB for Enzyme [Selected]
9 Warmup Slide to [37 Deg C], and Incubate for 4 Minutes (Enzyme Temp RB)
10 Apply One Drop of [PROTEASE 3] (Enzyme), and Incubate for [0 Hr 16 Min]
11 Inhibitor [Selected]
12 DISCOVERY Inhibitor [Selected]
13 Apply One Drop of DISC Inhibitor, and Incubate for [12 Minutes]
14 Antibody [Selected]
15 Antibody Blocking [Selected]
16 Apply One Drop of [Blocker 2] (Antibody Blocking #1), and Incubate for [28 Minutes]
17 Warmup Slide to [37 Deg C] from Very Low Temperatures (Primary Antibody)
18 Apply One Drop of [ANTIBODY 7] (Antibody), and Incubate for [60 Minutes]
19 Linking Antibody [Selected]
20 2nd Antibody [Selected]
21 Warmup Slide to [37 Deg C] from Very Low Temperatures (2nd Antibody)
22 Apply One Drop of [Anti-Rabbit HQ] (Detection #1), and Incubate for [0 Hr 24 Min]
23 Enzyme conjugate [Selected]
24 Apply One Drop of [Anti-HQ HRP] (Conjugate #1), and Incubate for [16 Minutes]
25 DISCOVERY Purple [Selected]
26 Apply One Drop of DISC H2O2 P, and Incubate for [0 Hr 32 Min]
27 Counterstain [Selected]
28 Use RB for Counterstain [Selected]
29 Apply One Drop of [HEMATOXYLIN II] (Counterstain), and Incubate for [8 Minutes]
30 Post Counterstain [Selected]
31 Use RB for Post Counterstain [Selected]
32 Apply One Drop of [BLUING REAGENT] (Post Counterstain), and Incubate for [4 Minutes]

Appendix C

Quantification of Brain Access of Exendin-4 in the C57BL Mouse Model by SPIM Fluorescence Imaging and the Allen Mouse Brain Reference Model

Quantification of Brain Access of Exendin-4 in the C57BL Mouse Model by SPIM Fluorescence Imaging and the Allen Mouse Brain Reference Model

Casper Bo Jensen[1], Anna Secher[2], Jacob Hecksher-Sørensen[2], Knut Conradsen[1], and Rasmus Larsen[1]

[1] Technical University of Denmark, Department of Applied Mathematics and Computer Science, Kgs. Lyngby, Denmark
[2] Novo Nordisk, Global Research, Måløv, Denmark
{cboa, knco, rl}@dtu.dk
{aasc, jhes}@novonordisk.com

Abstract. With the recent advance in 3D microscopy such as Single Plane Illumination Microscopy (SPIM) it is possible to obtain high resolution image volumes of the entire mouse brain. These data can be used to study the access of several peptides such as the glucagon-like peptide-1 (GLP-1) analogue Exendin-4, into the brain with the aim of developing medication for obesity. To investigate mode of action of the medication it is important to identify the specific anatomical brain nuclei that are targeted by the compound. Such segmentations can be obtained using an annotated digital brain atlas. We construct a SPIM brain atlas based on the Allen mouse brain 3D reference model and use it to analyze the access of peripherally injected Exendin-4 into the brain compared to a negative control group. The constructed atlas consists of an average SPIM volume obtained from eight C57BL mouse brains using group-wise registration. A cross-modality registration is performed between the constructed average volume and the Allen mouse brain reference model to allow propagation of annotations to the SPIM average brain. Finally, manual corrections of the annotations are performed and validated by visual inspection. The study shows that Exendin-4 have access to brain regions such as the arcuate hypothalamic nucleus and the nucleus of the solitary tract, which are areas involved in regulating food intake.

Keywords: Mouse brain ·Allen mouse brain 3D reference model ·Digital atlas ·Atlas segmentation ·Image registration

1 Introduction

Obesity is a disease, which has become a worldwide epidemic growing at an alarming rate. For the individual the consequence of obesity is an increased risk of acquiring metabolic disorders like type 2 diabetes and cardiovascular diseases.

Glucagon-like peptide-1 (GLP-1) analogues such as Exendin-4 have shown a positive effect on weight loss and thus belongs to a class of peptides which might be used for tomorrow's obesity medication. A way to study the distribution of GLP-1 analogues in the brain after administration is using histology, [3]. Due to the numerous histological slides that need to be produced, these types of studies are expensive and time consuming. Additionally, it is difficult to compare results across studies due to the difficulty of precisely denoting anatomical structures in the data.

One technique that might overcome these limitations is the new imaging modality Single Plane Illumination Microscopy (SPIM), which is a non-destructive method to produce well-registered optical sections suitable for 3D reconstruction [7]. SPIM is a type of fluorescence microscopy with the ability to produce 3D data of macroscopic objects in cellular resolution, e.g. of the mouse brain [5].

A popular segmentation strategy in neuro-imaging is the use of computational atlases, used in various imaging modalities both in human and animal models [4]. An atlas typically consists of a reference volume with accompanied annotations. The reference volume can be produced by computation of averages of ensembles of segmented images after image registration, [2]. A new image can then be segmented by image registration to the atlas volume and superimposition of the segmented structures from the atlas. For common imaging modalities some computational atlases of the mouse brain are available, e.g. [6], [9]. To the authors' knowledge no SPIM brain atlases have been published.

We construct a SPIM atlas by group-wise registration of recorded mouse brains. A good initial guess of the annotations are obtained by cross-modality registration to an existing atlas, and finally manual corrections are performed to complete the atlas. The Allen mouse brain reference model, [9], is used as the source of the annotations due to the model's high quality and detailed annotations.

We use the constructed atlas to investigate the access of peripherally injected Exendin-4 into the C57BL mouse brain based on quantification inside the segmented brain structures.

2 Method

2.1 Allen mouse brain reference model

A 3-D reference model, [9], is available for download using the API of the Allen Brain Atlas Data Portal [1]. The model is based on 132 annotated coronal plates of the adult mouse brain. Annotations are transferred from this reference model onto the constructed SPIM brain atlas.

Reference volume. The Allen 3-D brain volume was reconstructed from annotated plates using a combination of high frequency section-to-section histology registration with low-frequency histology to (ex-cranio) MRI registration. The reference volume was constructed in 2006, [15], and later updated in 2011. The

volume is based on Nissl stains that highlights brain regions of high nuclei concentration. The volume is available for download in 25 μm isotropic resolution. Prior to usage a smoothing of the reference volume and removal of the outer part of the olfactory bulb were performed.

Reference annotations. The full Allen atlas consists of 1204 symmetric 3-D structures, which are more than needed in this study. For the study of GLP-1 analogues 56 structures were chosen, with the highest concentration of structures in regions relevant for appetite control and obesity such as the hypothalamus. Each structure is color-coded to visually show the hierarchical position in the brain.

2.2 SPIM brains

In total 16 mice brains were recorded using SPIM. Eight brains were used for atlas construction and eight brains were used to quantify the access of Exendin-4 into the brain.

Tissue preparation and data recording. The conditions of housing and care of the animals as well as performance of the experiments are in agreement with the Danish law of animal experimentation. After sedation the mice were euthanized by cardiac perfusion with heparinized saline followed by neutral buffered formalin. The brains were removed and cleared for SPIM by a stepwise dehydration and clearing process using tetra hydro-flurane and di-benzyl-ether (DBE), respectively.
Data were recorded with a dual side illumination Lavision system utilizing a SuperK white light laser, a 620-nm emission filter, a 700-nm excitation filter, an Olympus microscope, and an Andor Neo sCMOS camera. The brain samples were immersed in a DBE bath during recording to minimize the difference in refractive index. The recordings were performed in 5.16 μm isotropic resolution.

2.3 Atlas construction

The constructed atlas contains 56 brain structures. Using the naming convention of the Allen reference model, [9], the structures are: Isocortex, AOB, AON, MOB, HPF, CA1, CA2, CA3, DG, BLA, ACB, CEA, CP, LSc, LSr, LSv, MS, SF, SH, TH, PVH, PVHd, ARH, SO, Pvi, PVa, Pvpo, OV, SFO, DMH, SCH, PVp, PH, VMH, LHA, ZI, ME, CLI, DR, IF, SNc, SNr, IPN, RL, VTA, PBl, PBm, AP, NTS, CB, ts, VL, AQ, c, V3, and V4. Two additional annotations are included consisting of other tissue and background, respectively.

Pre-processing. Following an initial cropping, the brain volumes were down sampled to 15 μm isotropic resolution and the axes were reordered to match the orientation of the Allen reference model with the first axis being dorsal-ventral, the second axis being lateral-medial, and the third axis being rostral-caudal. The data recording process deformed the structure of the olfactory bulb. Therefore this structure was cropped from the data along with the medulla oblongata, which is not part of the Allen reference model. The background voxels were set to zero and additional zero-padding was performed to center the brain inside the volume. Data obtained with the SPIM modality contains a bias field due to continuos attenuation of the laser sheet by the tissue sample, as well as a non-uniform intensity profile in the generated laser sheet depending on the microscope construction. Bias field correction was applied using a toolbox developed in [8]. Outliers originating from air bubbles trapped in the ventricular system during the tissue preparation process were removed.
After the individual pre-processing of the brains, intensity normalization was performed based on matching the median value of the brains. This was done to avoid creating an average volume biased towards scans with higher intensities caused by different microscope settings rather than on real biological differences.

Creation of SPIM atlas. Creation of the SPIM atlas was based on image registration between recorded SPIM data and the Allen reference model. The main registrations used in this work are based on a hierarchical transformation model, introduced in [11], which captures the global and local deformations of the tissue,

$$\mathbf{T}(x, y, z) = \mathbf{T}_{global}(x, y, z) + \mathbf{T}_{local}(x, y, z) \tag{1}$$

where the global transformation is a standard affine transformation. The local transformation model, a Free Form Deformation (FFD), is in 3D defined by an $n_x \times n_y \times n_z$ mesh of control points $\mathbf{\Phi}$ with spacing (δ_x,δ_y,δ_z). The underlying image is then deformed by manipulating the mesh of control points based on B-splines.
A fast way to regularize the deformation is to apply multi-level B-splines [12]; i.e. given control point resolutions $\Phi_1 ... \Phi_H$, at levels $1, ..., H$, the final local transformation is the sum of the transformations at each level,

$$T_{local} = \sum_{h=1}^{H} T_{local}^{h} \tag{2}$$

All transformations were calculated and applied using the Image Registration Toolkit, which was used under Licence from Ixico Ltd. [11], [12], [14].
The constructed SPIM atlas, based on the eight recorded SPIM scans, was created based on the following algorithm,

Algorithm 1 SPIM atlas construction

1: Register (rigid) all mouse brains to Allen reference model
2: Template = Intensity average of all registered mouse brains
3: **Repeat**
4: Register (FFD) all mouse brains to template
5: Template = Intensity average of all registered mouse brains
6: **Until** template stops changing
7: Register (FFD) Allen reference model (volume data + annotation data) to SPIM template

In line 1, using normalized mutual information, all scans were linearly (3 degrees of freedom for rotations, 3 degrees of freedom for translations) registered towards a pre-existing atlas, namely the Allen reference model. All scans were then averaged to create the first population atlas, representing the average anatomy of the study samples. An iterative 3 generation multi scale non-linear alignment procedure was then begun, registering each mouse towards the atlas of the previous non-linear generation using cross correlation as similarity measure. In line 6, the root-mean-square error between the voxel intensities of the current atlas and the previous atlas was calculated and an appropriate threshold value chosen to define the state where the atlas stopped changing. In line 7, the FFD transformation was calculated again based on the volume data of the Allen reference model. The calculated transformation was then applied to the annotation data of the model to bring these into alignment with the SPIM atlas volume. The last step in completing the SPIM atlas was manual correction of the computed annotations.

2.4 Exendin-4 study

A concentration of 240 nmol/kg Exendin-4 was fluorescently labelled with VivoTag-S 750 (Perkin Elmer) and injected into 6-8 weeks old male C57BL mice (Taconic) two hours prior to euthanization.
A two channel SPIM scan was performed of the brains with one channel recording the auto-fluorescence of the tissue, and the other channel recording the specific signal of the labelled Exendin-4. Similarly, four negative control brains were scanned following vehicle injection using the same data recording protocol. Segmentations of the brains were obtained by non-linear registration to the constructed atlas and propagation of the annotations. Detection of signal in the statistical analysis was performed by observing the 95th percentile inside each segmented brain area after removal of any bleed-through signal from the auto-fluorescence channel. The 95th percentile was used to eliminate outliers caused by small air bubbles typically situated on the surface of the tissue.

3 Results

3.1 Overview of constructed atlas

A mid-coronal (a-b), mid-transverse (c-d), and mid-sagtial (e-f) view of the constructed SPIM atlas is seen in Figure 1. The left column of images shows the reference volume, and the right column shows the annotations overlaid onto the reference volume.

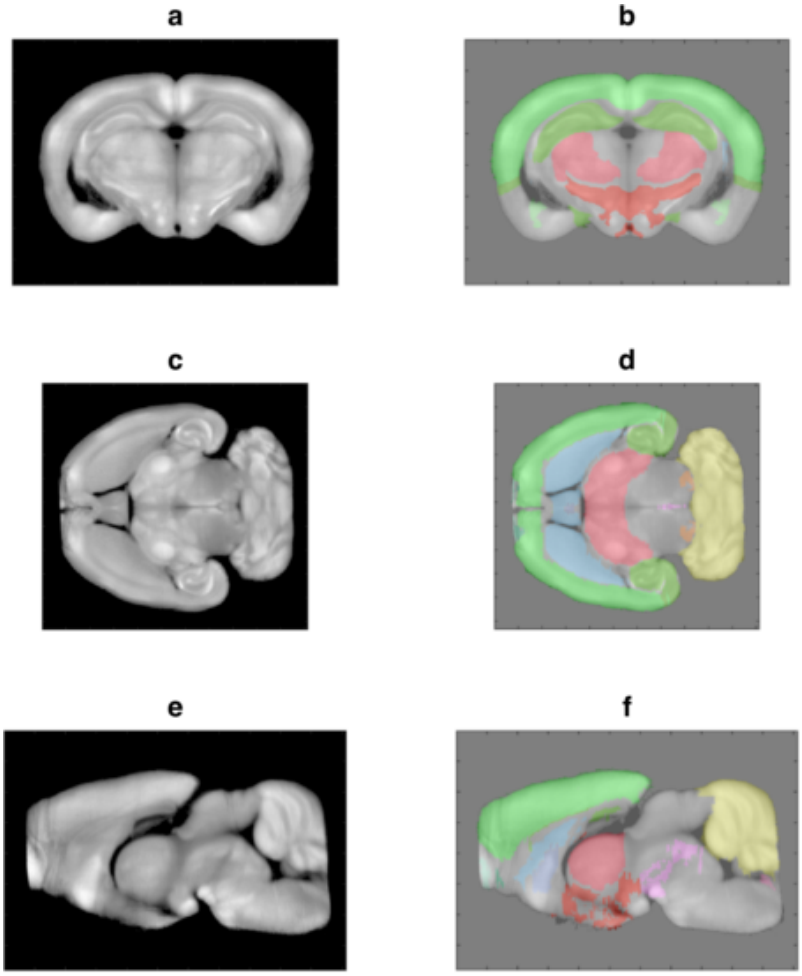

Fig. 1. Overview of constructed atlas. Left column (a,c,e) shows the atlas volume and the right column (b,d,f) shows the atlas with overlaid annotations. Green denotes the isocortex, red colors are part of the hypothalamus and thalamus, yellow is the cerebellum, blue structures belong to cerebral nuclei, and purple denotes midbrain structures.

3.2 Segmentation example

An example of an automatic segmentation performed using the constructed atlas is seen in Figure 2. The left image shows an example of an auto-fluorescence channel recorded as part of the Exendin-4 study, and the right image shows the corresponding specific channel overlaid with calculated annotations. Strong signals are seen ventrally in the hypothalamic structures and caudally near the hindbrain structures.

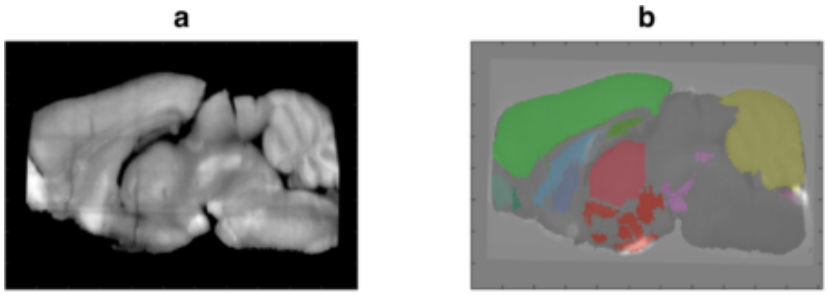

Fig. 2. Example of segmentation of a mouse brain following injection of fluorescent labelled Exendin-4. (a): Auto-fluorescence channel of the recording. (b): Specific fluorescence channel overlaid with calculated segmentaiton. High intensity (white) corresponds to a high fluorescence signal. Green denotes the isocortex, red colors are part of the hypothalamus and thalamus, yellow is the cerebellum, blue structures belong to cerebral nuclei, and purple denotes midbrain structures.

3.3 Quantification results

Quantification results inside segmented brain regions for the Exendin-4 study are seen in Figure 3. The bar height for each structure corresponds to the mean value of the 95th percentile detected inside that structure in the four mouse brains. The error bars show the standard deviation. Signal is detected inside Nucleus of the solitary tract (NTS), Area postrema (AP), Median eminence (ME), Periventricular hypothalamic nucleus - posterior part (PVp), Vascular organ of the lamina terminalis (OV), Periventricular hypothalamic nucleus - anterior part (PVa), Arcuate hypothalamic nucleus (ARH), Septofimbrial nucleus (SF), Lateral septal nucleus, caudal part (LSc). Signal is defined as a p-value less than 0.05 when performing a two sample t-test between the Exendin-4 group and the negative control group, with the null hypothesis of equal means in the groups, and the alternative hypothesis being the Exendin-4 group having a larger mean value than the negative control group. The sample size is four mice in each group. The scale of the x-axis on the plot is in arbitrary unit.

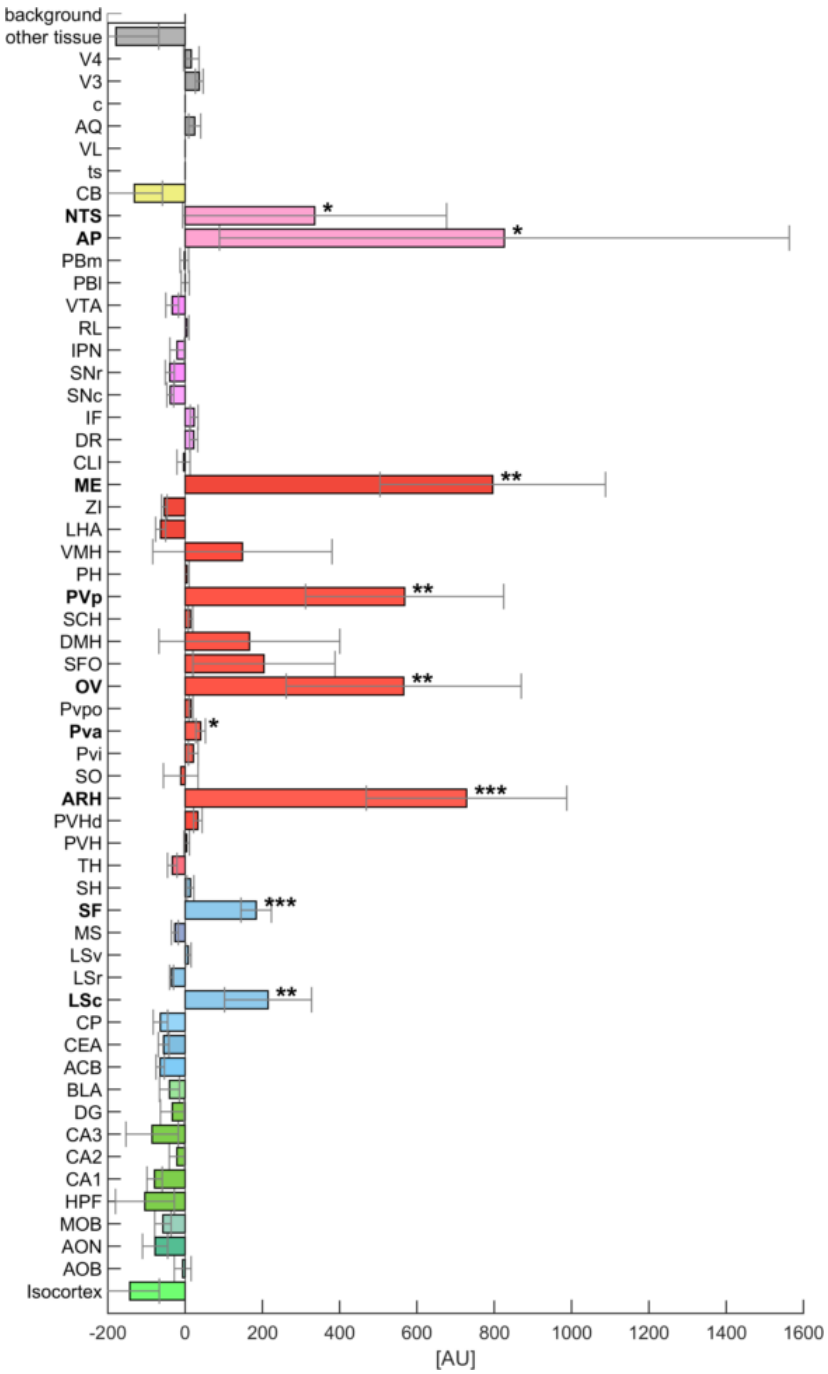

Fig. 3. Signal detection inside the automatically segmented brain regions following injection of Exendin-4. *p<0.05; **p<0.01; ***p<0.001 in a right tailed two sample t-test between the Exendin-4 group and the negative control group. Colors and acronyms follow the convention of the Allen 3D reference model.

4 Discussion

Access of Exendin-4 is seen in circumventricular structures such as ME, OV, and AP, which are brain areas not protected by the blood-brain-barrier and therefore expected to show a signal if any GLP-1 receptors are present. Access is also observed in other areas known to contain GLP-1 receptors such as the ARH and NTS. These areas have previously been identified as being part of the complex system that regulates food intake [13].
Observing the quantitative results in Figure 3, it is seen that some bars have a negative value. This is not expected in a scan setup where the value zero corresponds to no measured signal. The negative values appear due to the method of subtracting bleed-through signal of the auto-fluorescence channel. In future studies this can be avoided by using a better algorithm to remove the bleed-through signal. Although 58 t-test were made, no correction for multiple comparisons has been applied since the nature of the study was explorative.
Due to the lack of a ground truth a measure such as the Dice score can not be computed to evaluate the quality of the atlas, but by visually comparing the constructed atlas to other resources such as [10] the annotations of the structures appear to be correct. Basing a new atlas on a well established resource such as the Allen reference model has shown to reduce the dependency on neuro-anatomical expertise in order to construct the atlas. This is useful when working with a new image modality such as the SPIM system, and a similar approach can also be useful for constructing atlases for tomorrow's imaging systems.
Required manual corrections, and the overall quality of the atlas, is heavily influenced by the registration between the Allen reference model and the constructed SPIM average brain. The registration is challenging since it is both cross-modality and cross-subject. We have obtained a satisfactory result by varying registration parameters, but improvements can be obtained by manually adding landmarks. This could especially be useful around the ventricular system where the largest differences are observed between the reference model and the SPIM scans.

5 Conclusion

Access of Exendin-4 in brain structures known to regulate food intake is successfully demonstrated. Based on visual inspection the constructed brain atlas contains correct annotations of the included structures. Evaluating brain access of GLP-1 analogues, such as Exendin-4, will be important to investigate mode of action of the analogues with hope of developing future obesity medication. Since the constructed atlas is based on the Allen mouse brain reference model additional brain structures can easily be added if found relevant for study of other substances than GLP-1-analogues.

References

1. Allen institute for brain science. allen brain atlas [internet], http://www.brain-map.org
2. Balci, S.K., Golland, P., Shenton, M., Wells, W.M.: Free-form b-spline deformation model for groupwise registration. In: MICCAI... International Conference on Medical Image Computing and Computer-Assisted Intervention. vol. 10, p. 23. NIH Public Access (2007)
3. Balland, E., Dam, J., Langlet, F., Caron, E., Steculorum, S., Messina, A., Rasika, S., Falluel-Morel, A., Anouar, Y., Dehouck, B., et al.: Hypothalamic tanycytes are an erk-gated conduit for leptin into the brain. Cell metabolism 19(2), 293–301 (2014)
4. Castro-González, C., Ledesma-Carbayo, M.J., Peyriéras, N., Santos, A.: Assembling models of embryo development: Image analysis and the construction of digital atlases. Birth Defects Research Part C: Embryo Today 96(2), 109–120 (2012)
5. Dodt, H.U., Leischner, U., Schierloh, A., Jährling, N., Mauch, C.P., Deininger, K., Deussing, J.M., Eder, M., Zieglgänsberger, W., Becker, K.: Ultramicroscopy: three-dimensional visualization of neuronal networks in the whole mouse brain. Nature methods 4(4), 331–336 (2007)
6. Dorr, A., Lerch, J.P., Spring, S., Kabani, N., Henkelman, R.M.: High resolution three-dimensional brain atlas using an average magnetic resonance image of 40 adult c57bl/6j mice. Neuroimage 42(1), 60–69 (2008)
7. Greger, K., Swoger, J., Stelzer, E.: Basic building units and properties of a fluorescence single plane illumination microscope. Review of scientific instruments 78(2), 023705 (2007)
8. Larsen, C.T., Iglesias, J.E., Van Leemput, K.: N3 bias field correction explained as a bayesian modeling method. In: Bayesian and grAphical Models for Biomedical Imaging, pp. 1–12. Springer (2014)
9. Lein, E.S., Hawrylycz, M.J., Ao, N., Ayres, M., Bensinger, A., Bernard, A., Boe, A.F., Boguski, M.S., Brockway, K.S., Byrnes, E.J., et al.: Genome-wide atlas of gene expression in the adult mouse brain. Nature 445(7124), 168–176 (2006)
10. Paxinos, G., Watson, C.: The rat brain in stereotaxic coordinates: hard cover edition. Academic press (2006)
11. Rueckert, D., Sonoda, L.I., Hayes, C., Hill, D.L.G., Leach, M.O., Hawkes, D.J.: Non-rigid registration using free-form deformations: Application to breast mr images. IEEE Transactions on Medical Imaging 18, 712–721 (1999)
12. Schnabel, J.A., Rueckert, D., Quist, M., Blackall, J.M., Castellano-Smith, A.D., Hartkens, T., Penney, G.P., Hall, W.A., Liu, H., Truwit, C.L., et al.: A generic framework for non-rigid registration based on non-uniform multi-level free-form deformations. In: Medical Image Computing and Computer-Assisted Intervention–MICCAI 2001. pp. 573–581. Springer (2001)
13. Secher, A., Jelsing, J., Baquero, A.F., Hecksher-Sørensen, J., Cowley, M.A., Dalbøge, L.S., Hansen, G., Grove, K.L., Pyke, C., Raun, K., et al.: The arcuate nucleus mediates glp-1 receptor agonist liraglutide-dependent weight loss. The Journal of clinical investigation 124(10), 4473 (2014)
14. Studholme, C., Hill, D.L., Hawkes, D.J.: An overlap invariant entropy measure of 3d medical image alignment. Pattern recognition 32(1), 71–86 (1999)
15. Yushkevich, P.A., Avants, B.B., Ng, L., Hawrylycz, M., Burstein, P.D., Zhang, H., Gee, J.C.: 3d mouse brain reconstruction from histology using a coarse-to-fine approach. In: Biomedical Image Registration, pp. 230–237. Springer (2006)

Appendix D

Whole brain pStat3 activation: Why leptin is not a good obesity treatment

Whole brain pStat3 response: Why leptin is not a good obesity treatment

Casper Bo Jensen[1,2], Tomas Alanentalo[1], Knut Conradsen[2], Anders Bjorholm Dahl[2], Jacob Hecksher-Sørensen[1], Anna Secher[1]

[1]Global Research, Novo Nordisk A/S, Måløv, Denmark;

[2]Image Analysis & Computer Graphics, Department of Applied Mathematics and Computer Science , Technical University of Denmark, Kgs. Lyngby, Denmark;

Leptin was once thought a promising treatment for obesity but failed as the weight loss experienced by lean individuals was not transferrable to obese individuals. Leptin resistance has since been debated in the scientific community. In this paper we apply 3D imaging and analysis techniques to show why exogenous leptin administration is ineffective as an obesity treatment. We first mapped the leptin receptor location in the full mouse brain to identify possible direct targets of circulating leptin. Next, a time course study was performed to learn which time points different brain regions were activated following a peripheral leptin dose. Most pStat3 activation peak between 60 minutes and 120 minutes after leptin administration. Lastly, the pStat3 response to exogenous leptin was compared in lean mice, DIO mice, and *db/db* mice. The dynamics of the pStat3 response was significantly reduced in DIO mice compared to lean mice. No response was seen in the *db/db* model. In summary, this work provides a comprehensive 3D map on the pStat3 response in both lean and obese mice and demonstrates that the pStat3 signalling pathway is constitutively active in the brain of obese animals. We speculate that the high levels of leptin in the plasma leads to constant activation of pStat3 signalling in the neurons responsible for controlling appetite and food intake thus preventing exogenous leptin to add any additional information.

Introduction

Over the past decades the increase in individuals with obesity has reached epidemic proportion, posing a huge challenge on societies and healthcare budgets [1]. For the affected individual the consequence of obesity increased risk of metabolic diseases like type II diabetes and cardiovascular disease [2]. The obesity prevalence is attributed to the combined impact of increased high-energy food consumption and decreased physical activity. Throughout evolution complex physiological systems have evolved to regulate energy homeostasis. Leptin, a hormone secreted by adipose tissue, and its receptor are an integral component of this system [3, 4]. The leptin receptor (LepRb) is abundantly expressed throughout the mouse brain, with the largest concentrations of LepRb positive neurons found in the hypothalamus [5]. In the hypothalamus leptin has been shown to activate neurons expressing pro-opiommelanocortin (POMC) and inhibit neurons that co-express neuropeptide Y (NPY) and agouti-related peptide (AgRP) to decrease feeding [6,7]. In the hindbrain Leptin has been shown to act synergistically with the vagal actions of gut released anorexigenic peptides such as GLP-1 [8]. Several types of neurons in the LHA also respond to leptin and have been shown to interact with the mesolimbic system to regulate motivation and reward, including food reward [9-11]. Thus, Leptin have multiple ways to affect feeding and appetite via the brain.

An obese phenotype is seen when the leptin system is attenuated or fully disrupted. Recessive mutations in either the ob gene, encoding functional Leptin, or the db gene encoding the receptor, result in obesity and diabetes in a state resembling human obesity [12, 13]. While these genetic alterations are occasionally seen in humans it appears that the changed environment, not altered genetics, underlies the ongoing obesity epidemic [14]. An often used research model of obesity is the diet-induced obesity (DIO) model which mirrors the high availability of highly palatable calorie-dense foods in modern societies. In this model, animals remain lean when maintained on standard chow, but increase their caloric intake and rapidly gain adipose mass when given a calorically dense diet [14]. The high-fat diet and related obesity are associated with increased serum leptin levels and leptin resistance [15].

As leptin is important for controlling energy balance it is attractive to imagine leptin as a pharmaceutical treatment option for people with obesity. In lean mice administration of leptin by injection or constant subcutaneous infusion results in a dose-dependent decrease in body weight within the physiological range of leptin levels [16,17]. Treatment with leptin is however ineffective as a way to decrease food intake and body weight in obese individuals [18]. To investigate why exogenous leptin treatment does not have the same effect in the obese individuals as in lean individual we in this paper focus on brain activation in response to leptin treatment. The brain activation was studied based on detection of pSTAT3 which is commonly used as a marker of LepRb signalling [19] as it is part of the intercellular signalling occurring in response to activation of LepRb.

Previous work has shown that high fat diet attenuates leptin signalling in the brain [20, 21]. In this paper we pursue this hypothesis using novel techniques within imaging and automated quantification. Whole mouse brains were stained to visualize LepRb or pStat3 and subsequently scanned using Light Sheet Fluorescence Microscopy (LSFM). Automated quantification was performed using a digital brain atlas based on the Common Coordinate Framework version 3 (CCFv3) of the Allen Institute of Brain Science. We used these tools to evaluate the LepRb location, the time cause of pStat3 activation to exogenous leptin, as well as changes in pStat3 response to exogenous leptin in lean mice, DIO mice, and *db/db* mice. No activation was seen in the *db/db* mice, while the dynamic in brain activation with exogenous leptin was lost in the DIO model. The difference in dynamic between lean and DIO was partly explained by a stronger response to exogenous leptin in lean mice, but also by larger baseline activation from endogenous leptin in the DIO model.

Results

The leptin receptor is distributed widely throughout the mouse brain. To investigate the range of brain regions where leptin can have a direct effect we generated a 3D map of LepRb expression in the entire mouse brain We used the genetic model described by Patterson et al [5], as no sensitive method for LepRb detection by immunohistochemistry (IHC) is currently available. The model expresses cre recombinase from the LepRb-specific mRNA in combination with a cre-inducible enhanced green fluorescent protein (EGFP) to detect the soma of cells expressing LepRb mRNA. The $LepRb^{EGFP}$ mouse brain was scanned using LSFM to image the whole brain in 3D. The leptin receptor distribution was broad and scattered throughout the mouse brain (Fig. 1a-b). Higher concentrations of receptor were seen in cortical regions, hypothalamic regions, midbrain regions and hindbrain regions. Cortical regions included Dorsal auditory area (AUDd), Supplemental somatosensory area (SSs), and Ectorhinal area (ECT). Hypothalamic regions included Arcuate hypothalamic nucleus (ARH), Dorsomedial nucleus of the hypothalamus (DMH), and Lateral hypothalamic area (LHA). Midbrain regions included dorsal nucleus raphe (DR), Periaqueductal gray (PAG), and Ventral tegmental area (VTA). Hindbrain regions included Parabrachial nucleus (PB), Nucleus of the solitary tract (NTS), and Dorsal motor nucleus of the vagus nerve (DMX). In total 49 brain regions were chosen for further studies of pStat3 response (Table 1).

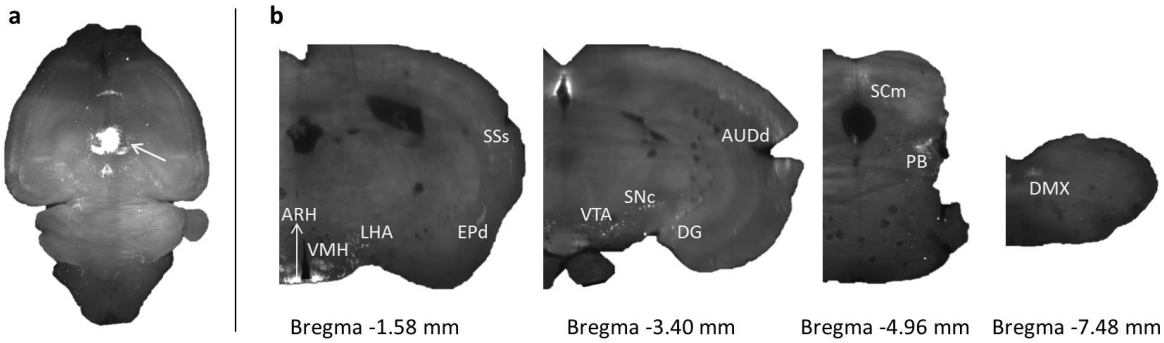

Figure 1 I Brain regions expressing LepRb. (**a**) Maximum intensity projection of $LepRb^{EGFP}$ mouse brain. Stongest LepRb expression was seen in the hypothalamus (white arrow). (**b**) Selected 2D coronal projections from (a) showing LepRb in ARH, VMH, LHA, EPd, SSs, VTA, SNc, DG, AUDd, SCm, PB, and DMX.

Table 1. Selected brain regions with leptin receptor expression

ACB	AI	ARH	AUDd	BMA	BST	CLA	CLI	CUN	DG	DMH	DMX	DR	ECT
EPd	IC	IPN	LH	LHA	LPO	LRNm	LS	MEA	MEPO	MM	MPN	MTN	NTS
PAG	PB	PH	PMv	PRC	PRNr	PSTN	PVH	PVp	RN	SCH	SCs	SNc	SNr
SSs	SUM	TEa	TU	VMH	VTA	ZI							

The pStat3 response following peripheral leptin dose in general peaks after 1-2 hours. Before evaluating the differences between pStat3 activation in disease models, it was important to establish the time lines of such activation. Following peripheral administration of leptin animals were euthanized after 10 minutes, 30 minutes, 60 minutes, 120 minutes, and 240 minutes. The brains were extracted and imaged using LSFM following IHC staining for pStast3 (Fig 2a). Heat maps representing the number of cells positive for pStat3 was created and quantified using a digital brain atlas based on the mouse brain atlas of the Allen Institute of Brain Science (Fig 2b-c). It was observed that the pStat3 response peaked at different time points in different brain regions, although most activation peaked between 60 minutes and 120 minutes (Fig 3.a). The earliest peaks (30 minutes) were seen with ARH and Periventricular hypothalamic nucleus, posterior part (Pvp) (Fig 3.b). The activation of most other hypothalamic nuclei peaked between 60 minutes and 120 minutes (Fig. 3c-d). Activation in the hindbrain peaked between 30 minutes and 60 minutes, while activation in VTA peaked at 240 minutes. pStat3 activation in brain regions associated with the limbic system such as the VTA, SNc, and NAc was in general low or undetectable.

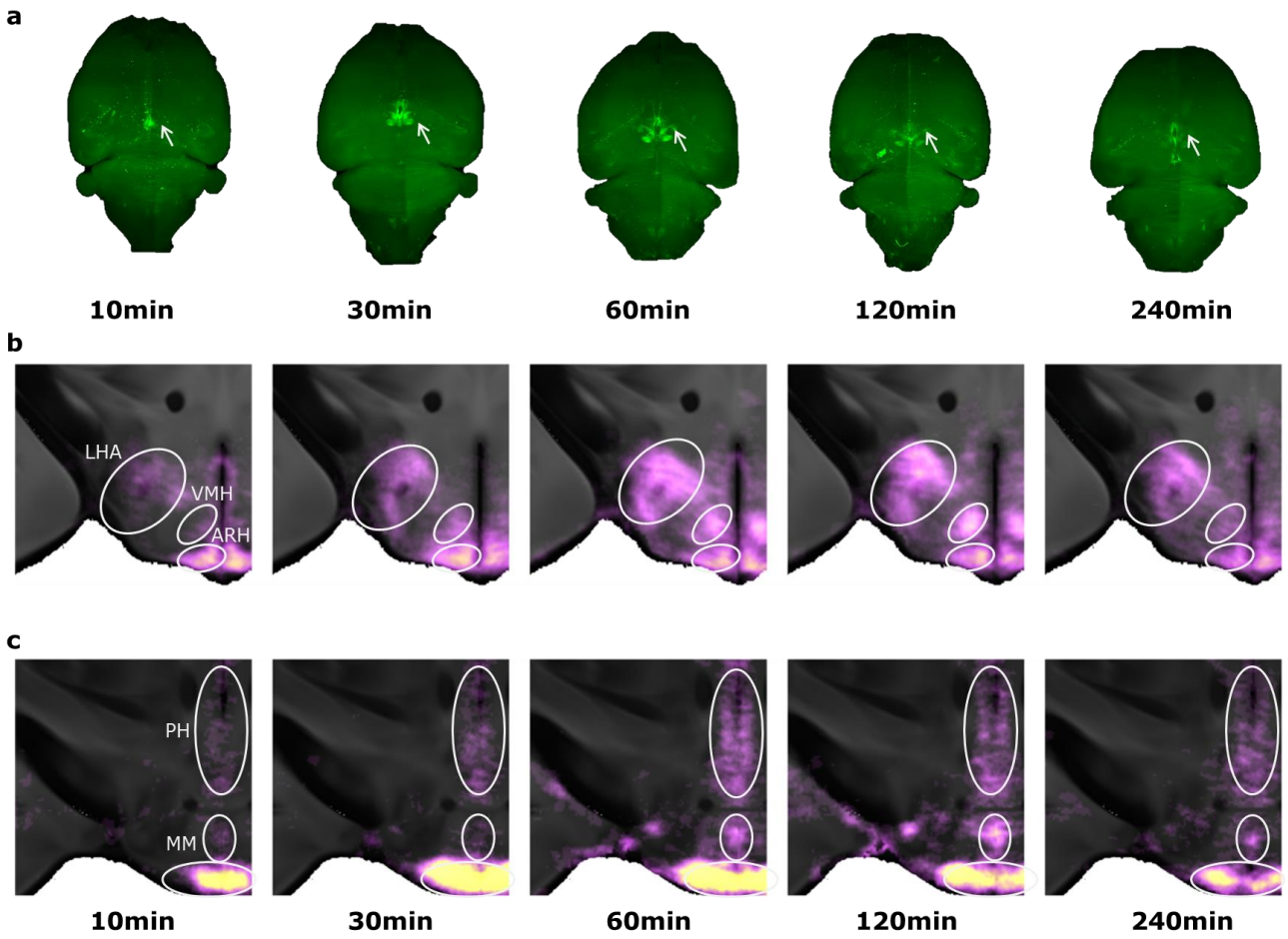

Figure 2 I Time course of pStat3 activation following leptin dose. (**a**) Maximum intensity projections of raw pStat3 data in mouse brains at different time point after subcutaneous leptin dose. Arrow indicates the hypothalamus. (**b-c**) Heat map indicating number of positive pStat3 cells overlaid onto 2D projections of the Allen mouse brain atlas. Selected brain regions are highlighted to show change in activation over the time points.

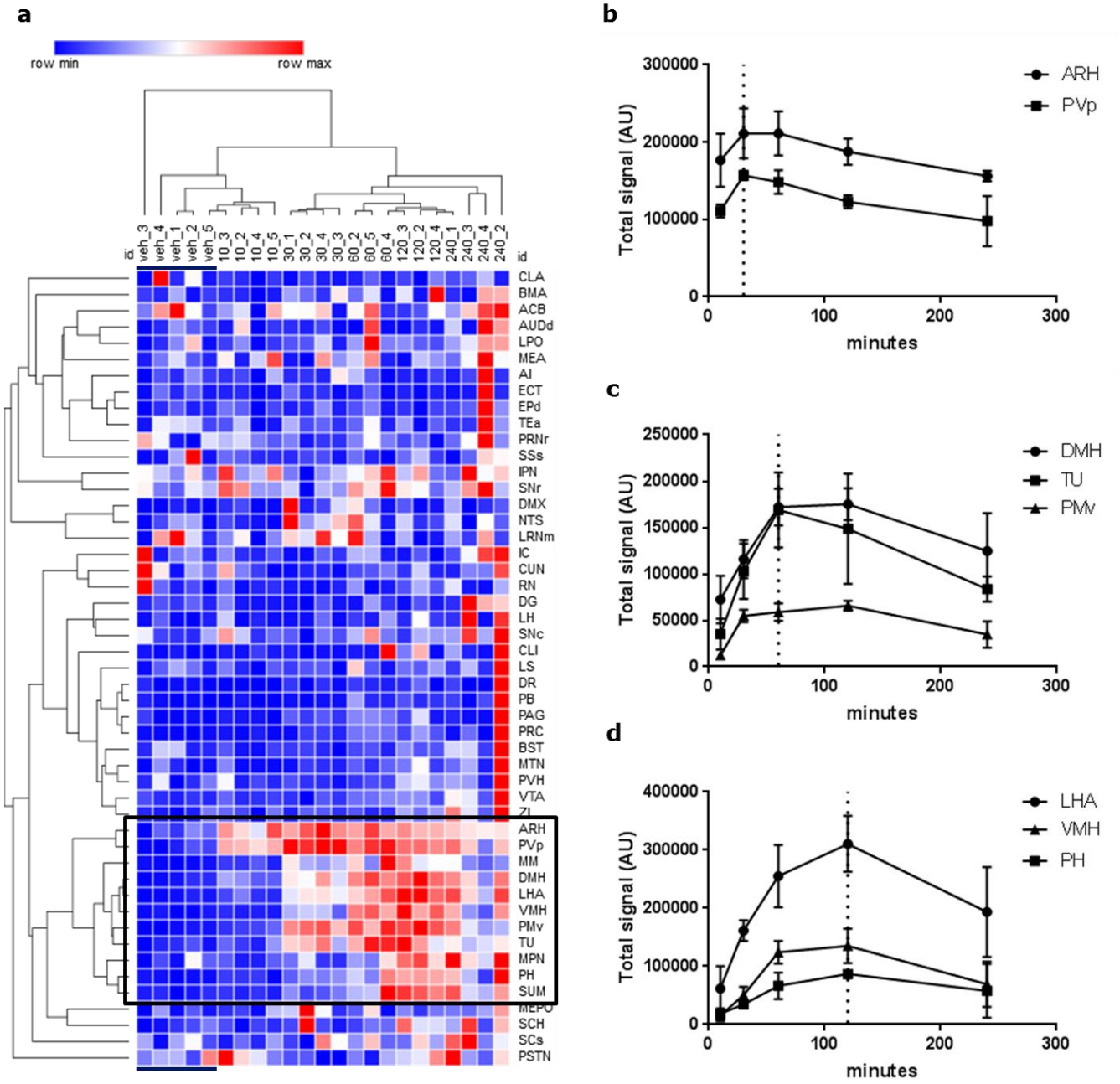

Figure 3 I Time course quantification. (**a**) Heat map showing the level of pStat3 activation in 49 brain regions with LepRb expression. The columns represent mouse brains with pStat3 activity measured at different time points after subcutaneous leptin dose. Heat map is clustered by rows and columns using a one minus Pearson correlation metric. Baseline pStat3 activation is displayed by including vehicle injected animals (columns marked by black line in top and bottom of heat map). The largest cluster of regions are hypothalamic nuclei (marked by black box) displaying peak activation from 30 minutes to 120 minutes. (**b-d**) Graph showing the mean fold change and standard deviation (SD) of the total fluorescence from pStat3 activation as a function of time since leptin dose, n=3-5. ARH and PVp activation peaks 30 minutes after leptin dose.

The pStat3 dynamic to peripheral leptin dose is lost in DIO mice compared to lean mice. We next sought to investigate potential differences in brain activation to exogenous leptin in normal mice compared to disease models. *db/db* mice were included as these lacks a functional LepRb and should thus show no activation when visualized by pStat3. DIO mice were included as this model shows a degree of leptin resistance and best mimics the human obesity epidemic partly driven by easy access to highly palatable foods. Brain activation by pStat3 was evaluated 60 minutes after subcutaneous leptin injection. Vehicle injections were included to show the pStat3 activation by endogenous leptin levels. As expected no pStat3 activation was observed in *db/db* following either leptin or vehicle injection (Fig. 4a). The only exception was signal in Nucleus ambiguus which was seen in all experiment groups. The lean mice showed strong brain activation following leptin injection and low activation following vehicle injection. The activation was most prominent in the hypothalamic regions. The DIO mice showed an attenuated response to leptin and higher baseline activation compared to lean mice. Average heat maps representing the number of cells positive for pStat3 was computed to visualize the difference between DIO and lean (Fig. 4b). Quantification of the pStat3 response in eight hypothalamic regions showed a large dynamic in the lean model with fold changes ranging from 6.35 (ARH) to 285.06 (LHA) (Fig. 5a). This increase in brain activation from exogenous leptin was not seen in the DIO model where the largest fold change was modest 2.66 (PH) (Fig. 5b). The difference in pStat3 dynamics between lean and DIO was partly explained by a stronger response to exogenous leptin in lean mice (Fig. 5c), but also by a larger activation from endogenous leptin in the DIO model (Fig. 5d).

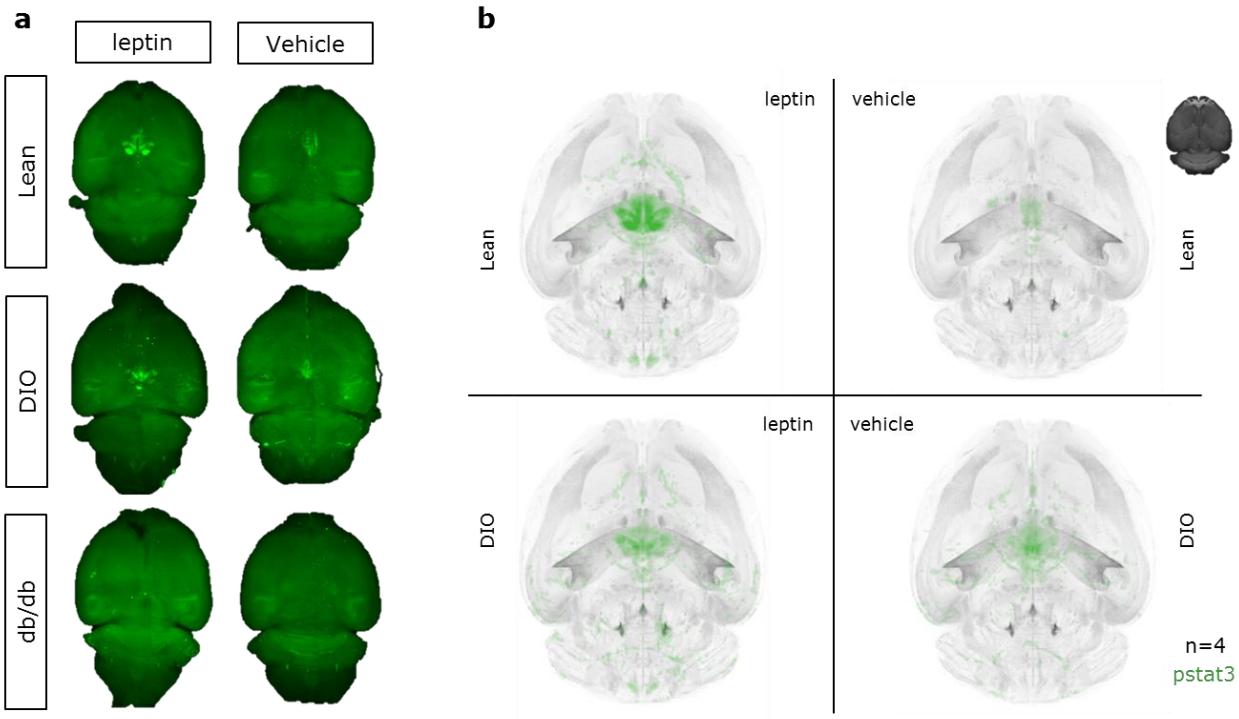

Figure 4 I Comparison of pStat3 activation following leptin dose in different animal models. (**a**) Maximum intensity projection of pStat3 activation in mouse brains following leptin or vehicle dose. (**b**) Maximum intensity projection of heat maps of average pStat3 activation in lean and DIO mice following leptin or vehicle dose, n=4. Heat maps are overlaid onto an auto-fluorescence based mouse brain template.

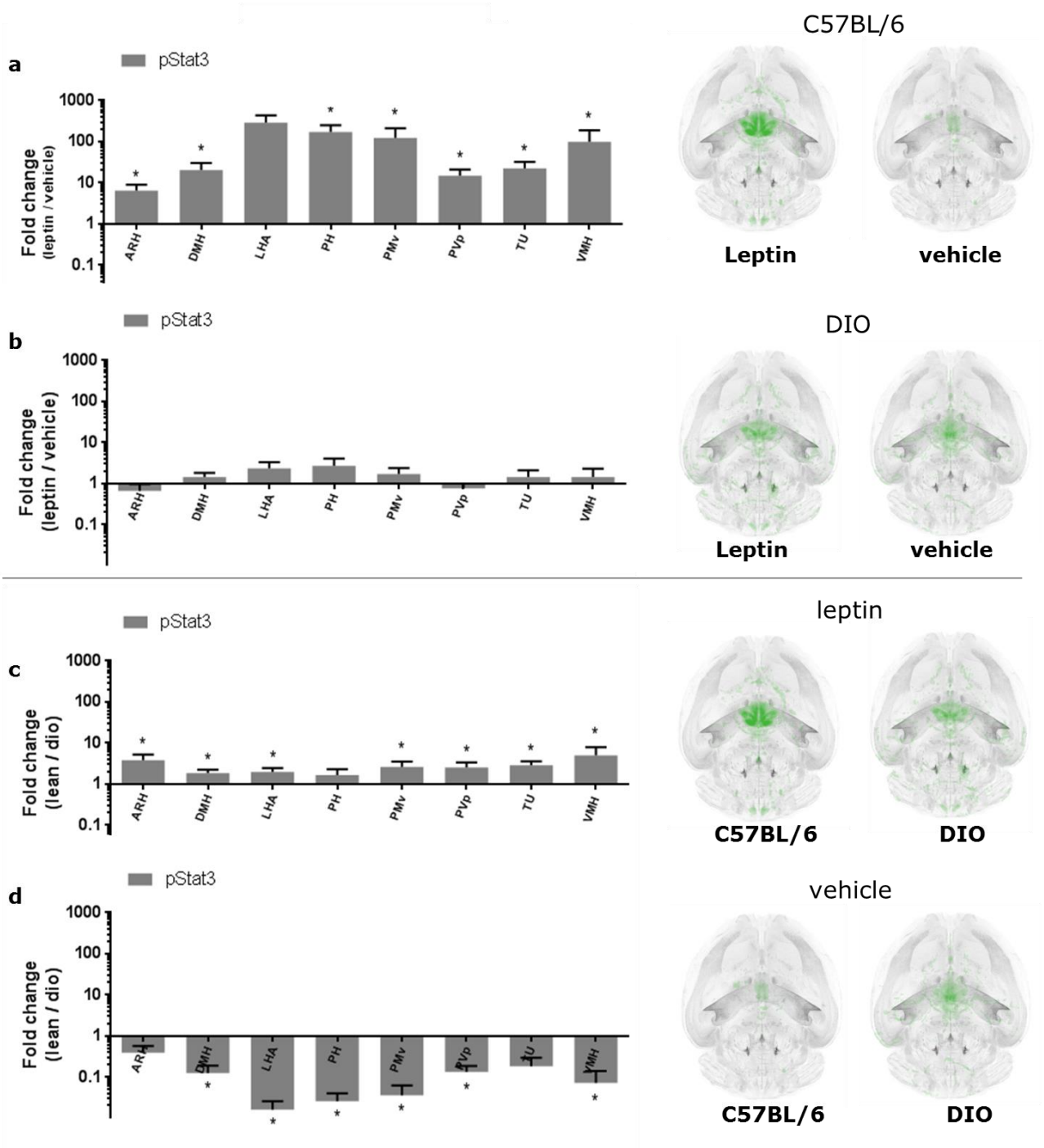

Figure 5 I Quantification of hypothalamic pStat3 response (**a**) Bar graph showing the mean fold change and SD between pStat3 activation following leptin vs vehicle dose in lean mice. Note the log scale on the y-axis. An asterisk marks significant difference between treatments when analyzed in individual brain regions using a false discovery rate value of 5% to correct for multiple comparisons. (**b**) Fold change between pStat3 activation following leptin vs vehicle dose in DIO mice. **(c)** Fold change between pStat3 activation following leptin dose in lean vs DIO mice. **(d)** Fold change between pStat3 activation following vehicle dose in lean vs DIO mice.

Discussion

LepRb expression was detected in various regions throughout the mouse brain with the highest concentration in the hypothalamus. Based on the receptor mapping leptin has the ability to directly affect both homeostatic feeding, meal generated signals, and reward driven feeding as LepRb was detected in regions such as ARH, LHA, VTA, PB, DMX, and NST. The receptor mapping was performed using a genetic model expressing EGFP driven by LepRb-specific mRNA. The EGFP accumulates in the cytoplasm and hence show the soma of the neurons containing LepRb mRNA serving as a good indicator of where the final receptor is expressed. However, when detecting the receptor based on mRNA it is possible that the receptor is expressed on additional cells or on axons or synaptic cliffs. This was e.g. recently showed in connection with GLP-1R [paper under submission / Paper B of thesis]. Better antibodies against the LepRb are needed to further clarify this potential issue.

pStat3 is a commonly used marker for LepRb activation and a time course study was performed to investigate the activation following a subcutaneous leptin dose. After 10 minutes, the earliest time point studied, the most significant pStat3 activation was seen in the ARH and PVp. This result fits with observations made by Ballard et al [22] describing tanycytes in the median eminance as the earliest access point of peripheral leptin to the brain. From ME leptin could reach the ARH and other hypothalamic regions. In this study we also observed increased pStat3 activation in DMX after 10 minutes suggesting signalling through the vagal nerve. After 30 minutes pStat3 activation was seen wide spread, including deeper regions such as LHA and PB. In general the pStat3 activation was strongest at the 60 minutes and 120 minutes time point which can be concluded to be suitable for studying activation of peripheral administrated leptin. Looking across the time points not all regions with LepRB was activated. As an example no activation was detected in the cerebral cortex, but also regions connected to the limbic system such as VTA, SNr and NAc showed at best very sparse signalling. This suggests that the effects of peripheral administered leptin mostly occur through the hypothalamus and hindbrain, but could also be through midbrain regions such as DR, PAG, and SCm which also displayed prominent pStat3 response. Concerning the methodology applied in these studies we utilized LSFM in combination with whole brain IHC staining using the iDISCO protocol [23]. With this system different positively stained cells may have different levels of intensity. The heat maps computed for the individual brains only reflect the number of positively stained cells, but not the absolute intensities of these cells. An example of this is seen in figure 2a where the absolute intensities are in general stronger after 60 minutes compared to 120 minutes. However, in regions where the number of positively stained cells is slightly higher after 120 minutes the computed heat maps are also more intense at the 120 minute time point. A 60 minute time point was chosen to study the pStat3 response in lean versus obese animal models.

pStat3 activation was next compared after leptin or vehicle dosing in different animal models to investigate why exogenous leptin has not shown to be an efficient treatment for obesity. No activation was seen in the obese *db/db* phenotype as expected since the mice lack a functional LepRb. Pstat3 activation in lean mice showed a large response to exogenous leptin, and could explain why administration of leptin by injection results in decrease in body weight as previously reported [16,17]. On the contrary pStat3 activation in the hypothalamus of DIO mice showed no increase of pStat3 activation in leptin versus vehicle dosed animals. In essence this means that the leptin injection was redundant as it did not change the brain activation compared to the baseline condition probably driven by high levels of endogenous circulating leptin. A similar picture was seen in the DMX and NTS of the hindbrain. Similar findings were reported by Morabito et. al. [20] comparing the dynamic of the pStat3 response in mice on low fat or high fat diet. In that study some of the mice on high fat diet was later switched to low fat diet after which they returned to a body weight comparable to the original low fat group. Following this intervention the pStat3 dynamic in the NTS was recovered, but not the dynamic in ARH and DMH. Pablo et al. [21] studied the effects of leptin on AgRP and NPY secretion comparing lean and DIO mice. Incubation with leptin caused dose-dependent inhibition of AgRP and NPY in lean mice but not in DIO. Similar results were

obtained looking at the sensitivity of POMC neurons by measuring levels of α-MSH. Again the sensitivity to leptin was lost in the DIO group. This could suggest that while pStat3 activation was still seen in ARH of the DIO mice in our study the downstream effects from the LepRb activation could still be lost. In the study by Pablo et al. [21] the sensitivity to leptin was restored after switching the mice from high fat diet to chow and allowing them to return to a body weight comparable to the original lean group. In general DIO animals tend to reduce their food intake and body weight when switched to a less palatable diet and this suggests that the DIO mice do not eat to defend a new homeostatic set point, but rather they eat because of the pleasure from the reward associated with a calorie-dense diet. Part of the explanation why high levels of circulating leptin do not mitigate the high calorie intake could be that the leptin effect on the limbic system is low. In our study the direct activation based on pStat3 was low in the limbic system. The limbic system could however still be activated as secondary effects of e.g. the LHA as discussed in the review by Myers et. al [24]. Despite what the underlying mechanisms are, either way leptin is not a good treatment for obesity as it provides little additional information to the brain compared to baseline conditions.

Methods

Animals. All *in vivo* studies were conducted in accordance with approved national regulations in Denmark, which are fully compliant with internationally accepted principles for the care and use of laboratory animals, and with animal experimental licenses granted by the Danish Ministry of Justice. Animals were obtained from Taconic, Denmark and housed in standard, temperature-controlled conditions with a 12-hour-light/dark cycle. The animals had ad libitum access to water and regular chow.

Whole brain pStat3 staining. C57Bl/6J male mice were subcutaneously injected with leptin (3 mg/kg) or vehicle (n=5). Mice were euthanized 60 min. (disease model study) or 10 min., 30 min., 60 min. 120 min., 240 min. (time course study) after injection using isofluorane followed by cardiac perfusion with 4% paraformaldehyde. Brains were excised and post fixed in 4% paraformaldehyde overnight at room temperature and transferred stepwise to 100% methanol using the following protocol. 20% methanol (in ddH2O) for 1h, 40% methanol for 1h, 60% methanol for 1h, 80% methanol for 1h, and 100% methanol for 1h twice. iDISCO staining was performed as described in Renier et al.[19] with one exception. All the washing steps after incubation with primary and secondary antibody were extended from one to three days. Incubation time for primary and secondary antibody was 4 days each. The primary antibody was Rabbit-a-pSTAT3 (#9145) from Cell Signaling (1:500 dilution), and the secondary antibody was Cy5-anti rabbit from Jackson Immunoresearch (1:1000 dilution).

Light sheet imaging. Brain samples were scanned using an UltraMicroscope II LSFM system (Lavision Biotec, Bielefeld, Germany) in 4.06 µm isotropic resolution. Data acquisition was performed using a 545 nm emission filter for imaging auto-fluorescence, and a 620 nm emission filter for imaging specific signals.

Image analysis. Images were registered to the digital brain atlas using the Elastix software library [25]. A source image $I_S(x)$ was registered to a target image $I_T(x)$ by finding a coordinate transformation $T(x)$ that made $I_S(T(x))$ spatially aligned with $I_T(x)$. We used an affine coordinate transformation for initialization followed by non-rigid b-spline coordinate transformation which was iteratively optimized with respect to the mutual information between the source and the target. Registration parameters for mapping of LSFM data were similar to those used in Renier et al.[3]. Cells segmentation of cells positive for pStat3 was performed using a combination of blob filtering and morphological operations. Heat maps were created by summing uniform intensity discs with diameter of 20 um placed on each voxel representing a cell. The algorithms were written in Matlab (Release 2012b, MathWorks, Natick, Massachusetts, United States) and applied as a XT-

plugin in Imaris (Release 7.6.5, Bitplane, Zurich, Switzerland). These software programs were also used to generate all figures in the manuscript.

Statistical analysis. ROI based analyses of the total fluorescence signal presented in Fig. 5a-d were computed using multiple t-tests assuming unequal variance. Statistical significance was determined by correcting for multiple comparisons using a false discovery rate set to 5%. The statistical analysis was performed using Graphpad Prism (Release 6, GraphPad Software, Inc., United States).

References

1. Cawley, John, and Chad Meyerhoefer. "The medical care costs of obesity: an instrumental variables approach." Journal of health economics 31.1 (2012): 219-230.

2. Prospective Studies Collaboration. "Body-mass index and cause-specific mortality in 900 000 adults: collaborative analyses of 57 prospective studies." The Lancet 373.9669 (2009): 1083-1096.

3. Friedman, Jeffrey M., and Jeffrey L. Halaas. "Leptin and the regulation of body weight in mammals." Nature 395.6704 (1998): 763-770.

4. Bates, Sarah H., et al. "STAT3 signalling is required for leptin regulation of energy balance but not reproduction." Nature 421.6925 (2003): 856-859.

5. Patterson, Christa M., et al. "Molecular mapping of mouse brain regions innervated by leptin receptor-expressing cells." Brain research 1378 (2011): 18-28.

6. Elmquist, Joel K., et al. "Identifying hypothalamic pathways controlling food intake, body weight, and glucose homeostasis." Journal of Comparative Neurology 493.1 (2005): 63-71.

7. Morton, G. J., et al. "Central nervous system control of food intake and body weight." Nature 443.7109 (2006): 289-295.

8. Huo, Lihong, et al. "Leptin and the control of food intake: neurons in the nucleus of the solitary tract are activated by both gastric distension and leptin." Endocrinology 148.5 (2007): 2189-2197.

9. Fulton, S. "Modulation of brain reward circuitry by leptin (vol 287, pg 125, 2000)." Science 287.5460 (2000): 1931-1931.

10. Kelley, Ann E., Brian A. Baldo, and Wayne E. Pratt. "A proposed hypothalamic–thalamic–striatal axis for the integration of energy balance, arousal, and food reward." Journal of Comparative Neurology 493.1 (2005): 72-85.

11. DiLeone, Ralph J., Dan Georgescu, and Eric J. Nestler. "Lateral hypothalamic neuropeptides in reward and drug addiction." Life sciences 73.6 (2003): 759-768.

12. Coleman, Douglas L. "Obese and diabetes: two mutant genes causing diabetes-obesity syndromes in mice." Diabetologia 14.3 (1978): 141-148.

13. Chen, Hong, et al. "Evidence that the diabetes gene encodes the leptin receptor: identification of a mutation in the leptin receptor gene in db/db mice." Cell 84.3 (1996): 491-495.

14. Myers, Martin G., et al. "Obesity and leptin resistance: distinguishing cause from effect." Trends in Endocrinology & Metabolism 21.11 (2010): 643-651.

15. El-Haschimi, Karim, et al. "Two defects contribute to hypothalamic leptin resistance in mice with diet-induced obesity." Journal of Clinical Investigation 105.12 (2000): 1827.

16. Halaas, Jeffrey L., et al. "Physiological response to long-term peripheral and central leptin infusion in lean and obese mice." Proceedings of the National Academy of Sciences 94.16 (1997): 8878-8883.

17. Halaas, Jeffrey L., et al. "Weight-reducing effects of the plasma protein encoded by the obese gene." Science-AAAS-Weekly Paper Edition 269.5223 (1995): 543-545.

18. Blüher, Susann, and Christos S. Mantzoros. "Leptin in humans: lessons from translational research." The American journal of clinical nutrition 89.3 (2009): 991S-997S.

19. Münzberg, Heike, Jeffrey S. Flier, and Christian Bjørbæk. "Region-specific leptin resistance within the hypothalamus of diet-induced obese mice." Endocrinology 145.11 (2004): 4880-4889.

20. Morabito, Michael V., et al. "Weight Perturbation Alters Leptin Signal Transduction in a Region-Specific Manner throughout the Brain." PloS one 12.1 (2017): e0168226.

21. Enriori, Pablo J., et al. "Diet-induced obesity causes severe but reversible leptin resistance in arcuate melanocortin neurons." Cell metabolism 5.3 (2007): 181-194.

22. Balland, Eglantine, et al. "Hypothalamic tanycytes are an ERK-gated conduit for leptin into the brain." Cell metabolism 19.2 (2014): 293-301.

23. Renier, Nicolas, et al. "iDISCO: a simple, rapid method to immunolabel large tissue samples for volume imaging." Cell 159.4 (2014): 896-910.

24. Myers, Martin G., et al. "The geometry of leptin action in the brain: more complicated than a simple ARC." Cell metabolism 9.2 (2009): 117-123.

25. Klein, Stefan, et al. "Elastix: a toolbox for intensity-based medical image registration." IEEE transactions on medical imaging 29.1 (2010): 196-205.

Appendix E

Active appearance segmentation for intensity inhomogeneity in light sheet fluorescence microscopy

ACTIVE APPEARANCE SEGMENTATION FOR INTENSITY INHOMOGENEITY IN LIGHT SHEET FLUORESCENCE MICROSCOPY

C.B. Jensen[⋆†], *M. Lyksborg*[⋆], *J. Hecksher-Sørensen*[†], *A. Secher* [†], *K. Conradsen*[⋆], *A.B. Dahl*[⋆]

[⋆] Technical University of Denmark (DTU), DTU Compute, Kgs. Lyngby, Denmark
[†] Novo Nordisk, Global Research, Måløv, Denmark

ABSTRACT

Active Appearance Models (AAM) are used for annotating or segmenting shapes in biomedical images. Performance relies heavily on the image data used to train the AAM. In this paper we improve the generalization properties of the model by making it robust to slowly varying spatial intensity inhomogeneities which are often seen in Light Sheet Fluorescence Microscopy (LSFM) images. This robustness is achieved by modelling the appearance of an image as a regularized Normalized Gradient Field (rNGF). We perform two experiments to challenge the model. First it is tested using a repeated leave-one-out approach on images with minimal imperfections where the left out images are corrupted by a simulated bias field and segmented using the AAM. Secondly we test the model on LSFM images with common acquisition problems. In both experiments the proposed approach outperforms the often used AAM implementation based on Sum of Squared Differences.

Index Terms— Active Appearance Model, regularized Normalized Gradient Field, Light Sheet Fluorescence Microscopy, Segmentation

1. INTRODUCTION

Light Sheet Fluorescence Microscopy (LSFM) is an imaging technology for studying biology on a microscopic scale. The technology has for instance been used to image whole mice brains with micrometer resolution [1]. A scan sequence can acquire multiple contrasts, recording auto-fluorescence of the tissue in one channel and specific fluorescently labelled proteins in an other. With auto-fluorescence providing anatomical information, and the labelled protein revealing function, LSFM is of broad interest for mode of action studies both in basic as well as applied research.

To fully utilize the potential of the modality requires a segmentation of anatomical regions which is particularly challenging due to image distortions affecting both intensities and shape anatomy. In animal studies the anatomic distortions may be caused by brain extraction and chemical tissue clearing, which are performed prior to scanning and allows the light sheet to penetrate with minimal scattering and absorption [2]. The tissue clearing procedure also introduces unwanted intensity distortions since the efficiency varies between subjects. The optical elements inside the LSFM system also causes intensity distortions which may appear differently across subjects but generally appear as slowly varying spatial inhomogeneities of the intensities.

These distortions pose a challenge to image segmentation methods. The most common form of LSFM-related segmentation concerns the identification of highly local intensity build ups [3], used to investigate cellular morphologies within anatomical regions of interest. For high-throughput studies, manually delineating anatomic regions becomes in-feasible. Recent work in mice has used atlas-based segmentation methods to address this issue. For instance, we [4] previously performed segmentation using image registration to transform labels from a digital mouse brain atlas towards an individual mouse.

In this work we developed a model for segmentation based on the Active Appearance Model (AAM) [5], a model known to have problems dealing with varying illuminations across an image population [6]. Within the area of face recognition, robustness against illumination is typically achieved by normalizing intensity appearance [7],[8]. In our approach, this normalization is achieved by extending the AAM to model the textural appearance given as a regularized Normalized Gradient Field (rNGF) [9]. The idea is similar to using that of [7] aimed at facial recognition. Instead of a simple gradient field, we use a regularized version combined with a different optimization strategy for fitting the model to new images. It leads to a model that is robust to noise and has invariance with respect to the slowly varying intensity distortions present in the LSFM modality. To our knowledge it is the first time the AAM has been adopted toward LSFM images. We successfully demonstrate the rNGF-based AAM in two experiments on acquired images of the c57bl mouse brain. It is first demonstrated for the purpose of segmenting five anatomical brain regions in images which were artificially corrupted by a user controlled bias field. Secondly the approach is demonstrated on data exhibiting common LSFM artefacts.

2. DATA

2.1. Tissue preparation and data acquisition

All *in vivo* studies were conducted in accordance with approved national regulations in Denmark which are fully compliant with internationally accepted principles for the care and use of laboratory animals, and with animal experimental licenses granted by the Danish Ministry of Justice. After sedation the mice were euthanized by cardiac perfusion with heparinized (10U/ml) saline followed by 10% neutral buffered formalin (NBF). The brains were removed and immersed into 10% NBF and stored at 4°C until further processed. The brains were cleared for LSFM by a stepwise dehydration and clearing process using tetra-hydro-flurane and di-benzyl-ether (DBE), respectively [2]. Data acquisition was performed with a dual side illumination Ultamicroscope using a SuperK white light laser, and an Andor Neo sCMOS camera. The images were acquired in 10.32 μm isotropic resolution.

2.2. Shape annotation of images

After acquisition the brain volumes were transformed to a standard space using rigid registration. For the purpose of building the AAM,

a coronal slice corresponding to the same anatomy across subjects was selected for manual annotation. The five regions of annotations were; Lateral Ventricle (VL), Zona Incerta (ZI), Spinal Nucleus of the Trigeminal, caudal part (SPVC), Dentate Gyrus, part 1 (DG 1), and Dentate Gyrus, part 2 (DG 2), see Fig. 1, top. The shapes of these regions were annotated using 4, 4, 4, 6 and 5 anatomic landmarks respectively. As a final preprocessing each shape was equidistantly up-sampled to consists of 40 coordinates yielding a total of 200 correspondence points per image.

3. METHOD

The method used for segmenting LSFM images is based on the AAM [5]. This is a generative model of both shape and appearance (image texture). In the following sections it is explained how we extend the AAM to obtain improved LSFM segmentation performance. First we introduce the rNGF as a descriptor of image appearance. This descriptor is suitable for LSFM images as it has a built-in invariance against slowly varying spatial intensity inhomogeneities. Next follows a section detailing how to estimate the model, and the final section explains how this model was made active, enabling it to segment new images.

3.1. Texture: The regularized Normalized Gradient Field

The most common way of describing appearance is using pixel intensities. Appearance models based on intensities work well in many circumstances but have difficulties coping with intensity distortions not previously seen by the model. To achieve invariance against such distortions our appearance will be based on the rNGF as proposed by Haber [9]

$$n_\epsilon(I(x)) = \frac{\nabla I(x)}{\sqrt{\nabla I(x)^T \nabla I(x) + \epsilon^2}}, \quad \epsilon = \frac{\eta}{V} \int_\Omega |\nabla I(x)| \, \partial x. \tag{1}$$

The rNGF in $n_\epsilon(I(x))$ maps the image $I(x)$ to a higher dimensional space where the texture at pixel position x is mapped to a directional vector with elements in the range $n_\epsilon \in [0, 1]$. To control the impact of noise, the value of ϵ is set by summing the absolute image gradients across the domain Ω, dividing with the image area V, and multiplying by η. Thus η effectively controls ϵ and since $n_\epsilon \to 0$ for $\nabla I(x)^T \nabla I(x) << \epsilon^2$, it determines when an image gradient is considered noisy.

3.2. The Appearance Model

Appearance Models [5] establish a compact parameterization of object variability, as learned from a training set of shape and texture. The shape of each training image is defined by $N = 200$ manually placed landmarks as previously explained. The shapes of these training subjects are aligned to a common mean using the Generalised Procrustes Analysis (GPA) [10] removing effects of translation, rotation and scaling. Similarly, the textures of the training images are warped into the cross-correspondence mean shape space using a piece-wise affine warp. The obtained intensity textures are sampled and mapped to the rNGF representation. Shape and texture variability models are now formed based on the eigenvectors of the $Nd \times Nd$ shape covariance matrix and the $dK \times dK$ texture covariance matrix respectively. Here d is number of image dimensions, N is the number of landmarks used to represent each shape and K is the number of intensities sampled for each training example. The individual shape and texture models are

$$x = \bar{x} + \Phi_x b_x, \quad g = \bar{g} + \Phi_g b_g \tag{2}$$

Where x denotes the column form of a modeled shape, $\bar{x}$ is the training shape mean, Φ_x and b_x correspond to the shape eigenvectors and parameters respectively. Similarly, rNGF texture is modeled by g, the texture mean ($\bar{g}$), the eigenvectors (ϕ_g) and the parameters (b_g). A combined shape and texture model is made by concatenating the parameters of b_x and b_g for all training examples and performing and additional eigen-decomposition. This gives the model

$$x = \bar{x} + \Phi_x W_x^{-1} \Phi_{c(x)} c, \quad g = \bar{g} + \Phi_g \Phi_{c(g)} c, \tag{3}$$

where c is a vector containing the model parameters affiliated with the eigenvectors in matrices $\Phi_{c(x)}$, $\Phi_{c(g)}$ given by the sub-matrices of Φ_c, corresponding to rows related with shape and texture respectively. The matrix W_x is a diagonal matrix weighting which accounts for unit differences between shape and texture. These weights are estimated by perturbing the shape parameters of all training data by one unit and measuring the average euclidean change in texture.

To get a regularized model, the eigenvectors explaining least training variability are removed from the model using the 95% criteria [11]. An example of the principle variability captured by such a model is shown in Fig. 1. By varying the first parameter of the model, it appears the dominant shape variability is cause by size and the between shape positioning of the five shapes. The first parameter of the rNGF appearance is more difficult to interpret but seems to be related with gradient magnitudes.

3.3. Model-based segmentation

Fitting the rNGF-based AAM to a new image requires minimization of a cost function measuring discrepancies between the rNGF image texture $n_\epsilon(I(x))$ and the model texture $g(x)$

$$C(c, S) = \int_\Omega ||n_\epsilon(T^{-1}(I(S(x)))) - g(x)|| \, \partial x. \tag{4}$$

The brackets $|| * ||$ refers to the Euclidean norm and T^{-1} describes the texture mapping from the image to the normalized model space, achieved using a piece-wise affine warp. The cost function is minimized with respect to two parameters. The AAM parameters in c, and the parameter S which describes a global similarity transformation given by 4 parameters (scale, rotation and two translations).

Optimization details

The parameters are estimated using a gradient descent algorithm [12], where numeric gradients are obtained from a central finite difference approximation. To avoid local minima this is done with a multi-resolution strategy using 4 resolution levels, each resolution optimized and propagated in a coarse to fine manner.

The starting guess for the optimization is the mean model and the same optimization is run 9 times with different spatial starting positions. The 9 positions include the image centroid and 8 regularly sampled positions around the center. At the end of this grid search the fit with lowest cost function value in equation (4) is kept as optimal.

To prevent the AAM model parts composed of low magnitude gradients from fitting to the background, intensities are artificially inserted into the background of the intensity images prior to fitting. These values are inserted using an alternating 2×2 checkerboard pattern, set to either plus or minus the maximum image intensity.

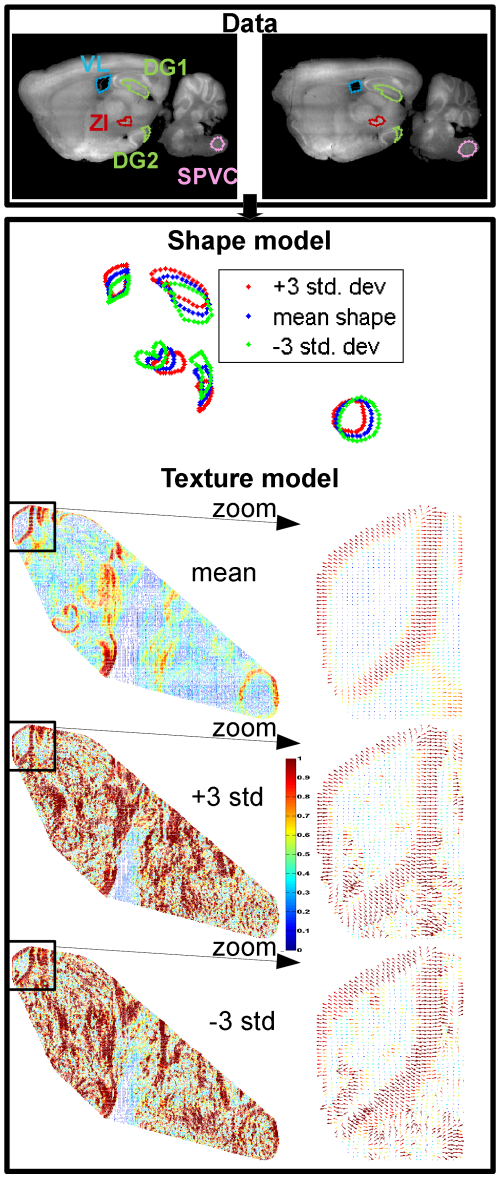

Fig. 1. Examples of two LSFM images overlaid with the shape annotations of VL, DG 1, DG 2, ZI and SPVC. The combined shape and appearance model built from 21 subjects is illustrated by setting the first parameter of equation (3) to $\pm$ 3 standard deviations of the associated eigenvalue. Magnitudes of the rNGF fields are indicated by the [0,1] color-bar. Dimension of the images is 700x957 pixels.

4. RESULTS

To show the increased robustness of using rNGF-based segmentation in LSFM images, two experiments were performed. The first experiment investigated the effect of manipulating the images by applying a controlled artificial bias field to mimic slowly varying spatial intensity inhomogeneities. The Dice score [13] was used to evaluate the quality of the segmentation. Evaluation of the AAM was performed using a leave-one-out cross validation approach based on 21 mouse brains. The brains were acquired as uniformly as possible regarding optical parameters and tissue clearing.

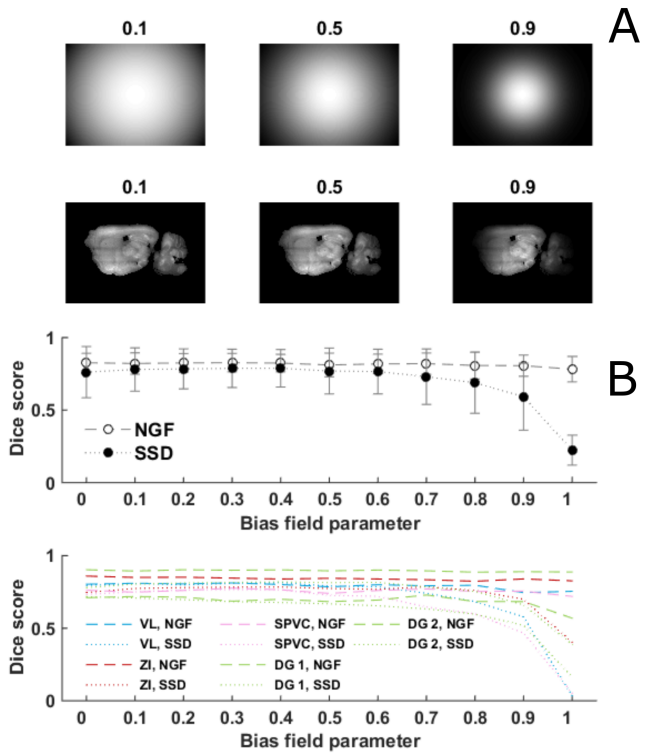

Fig. 2. A: Images of selected artificial generated bias fields and the effect of applying these to the test images. The bias field parameter value used to generate the specific bias fields are displayed above the images. B: Top plot shows the overall Dice scores (mean value and standard deviation) of the two models as function of the applied bias field strength. Bottom plot shows the Dice scores of the individual annotation structures. The rNGF-based results are shown with dashed lines, and SSD-based results are shown with dotted lines.

The left-out test images were systematically corrupted by multiplication with artificially generated bias fields of increasing strength, see Fig. 2.A. The bias fields were constructed using a Gaussian kernel with the bias field parameter corresponding to the percentage-wise decrease in pixel intensities towards the border of the images. The overall Dice score of the model as function of the bias field strength is seen in Fig. 2.B, top plot. A bias field parameter equal to zero means that no bias field distortion was applied to the images. The Dice scores of the individual anatomical shape segmentations are seen in Fig. 2.B, bottom plot. Annotation names and line color match those seen in Fig. 1. The rNGF-based model performs on par or better for all cases compared to the AAM implementation based on Sum of Squared Differences (SSD).

The second experiment investigated the model performance under a more realistic scenario. The AAM trained on the 21 brains from the first study was tested on images with common LSFM imperfections. The test set consisted of 8 images where half contained brains with poor tissue clearing and the other half contained brains scanned with a lower quality light sheet. Examples of segmentation results obtained with the rNGF-based AMM and the SSD-based AAM are seen in Fig. 3.A. The SSD-based model fails to segment the VL in case of the lower quality light sheet. Dice scores of the individual annotation structures are seen in Fig. 3.B. The rNGF-based model results in higher Dice scores and less variance.

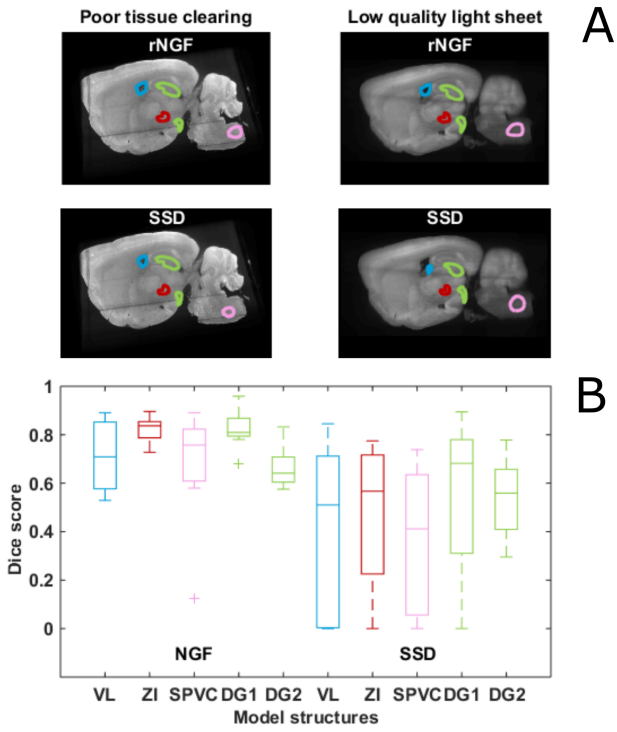

Fig. 3. A: Examples of segmentations obtained with rNGF-based model (top row) and SSD-based model (bottom row). Left image shows a brain with poor tissue clearing and right image shows a brain recorded with lower quality light sheet. B: Boxplot of Dice scores of the individual annotation structures. The median is represented as the center line of each box and the edges correspond to the 25th and 75th percentiles.

5. DISCUSSION

In contrast to the classical SSD-based model, the rNGF-based AMM is robust to artificial image corruption by a controlled bias field. The rNGF-based model shows only slight performance decrease when tested on images distorted with more extreme bias fields (Fig. 2.B, top plot). Even with the largest image distortion, the model provides a good result with a Dice score close to 0.8 whereas the SSD-based implementation breaks down completely. This result is seen for all annotation structures (Fig. 2.B, bottom plot) which confirms that the regularized normalized gradient measure is less affected by slowly varying spatial intensity inhomogeneities.

The rNGF-based model also generalizes well to images with lower quality compared to the training set (Fig. 3.B). The test set contains images obtained with a lower quality light sheet making the images appear blurry, and of images of brains with poor tissue clearing causing a different intensity distribution. Both challenges are handled by the rNGF-based model showing the promise of this model for segmentation of LSFM images. The rNGF-based model performs well for structures having large gradients to surrounding tissue such as the VL (blue), but also for structures where the gradients are smaller and more specular such as the Zona Interna (red) and SPVC (pink).

In summary we have shown that the rNGF-based AAM is robust to effects of poor tissue clearing and to variation in quality of the light sheet used during image acquisition. Having a model for robust segmentation of anatomic regions shows promise for conducting automated high-throughput studies of the mouse brain using LSFM.

6. REFERENCES

[1] K. Becker, N. Jährling, E.R. Kramer, F. Schnorrer, and H. Dodt, "Ultramicroscopy: 3d reconstruction of large microscopical specimens," *Journal of biophotonics*, vol. 1, no. 1, pp. 36–42, 2008.

[2] A. Ertürk, K. Becker, N. Jährling, C.P. Mauch, C.D. Hojer, J.G. Egen, F. "Three-dimensional imaging of solvent-cleared organs using 3disco," *Nature protocols*, vol. 7, no. 11, pp. 1983–1995, 2012.

[3] L. Silvestri, A. Bria, L. Sacconi, G. Iannello, and F.S. Pavone, "Confocal light sheet microscopy: micron-scale neuroanatomy of the entire mouse brain," *Opt. Express*, vol. 20, no. 18, pp. 20582–20598, Aug 2012.

[4] C.B. Jensen, A. Secher, J. Hecksher-Sørensen, K. Conradsen, and R. Larsen, "Quantification of brain access of exendin-4 in the c57bl mouse model by spim fluorescence imaging and the allen mouse brain reference model," in *19th Scandinavian Conf. Image Analysis*, vol. 9127, pp. 452–461. 2015.

[5] T.F. Cootes and et al., "Active appearance models," *IEEE Trans. Pattern Anal. & Mach. Intell.*, , no. 6, pp. 681–685, 2001.

[6] S. Shan, W. Gao, B. Cao, and D. Zhao, "Illumination normalization for robust face recognition against varying lighting conditions," in *Proc. IEEE Int. Workshop on Analysis and Modeling of Faces and Gestures*, 2003, pp. 157–.

[7] G. Tzimiropoulos, J. Alabort i Medina, S. Zafeiriou, and M. Pantic, "Generic active appearance models revisited," in *11th Asian Conf. on Computer Vision*, Nov 2012.

[8] P. Sauer, T.F Cootes, and C.J Taylor, "Accurate regression procedures for active appearance models," in *Proc. British Machine Vision Conference*, 2011, pp. 30.1–30.11.

[9] E. Haber and J. Modersitzki, "Intensity gradient based registration and fusion of multi-modal images," in *Methods of Information in Medicine*, 2006, pp. 726–733.

[10] I.L Dryden and K.V. Mardia, *Statistical shape analysis*, Wiley, 1998.

[11] I.T. Jolliffe, *Principal component analysis, 2nd. ed.*, Springer, 2002.

[12] J. Nocedal and S.J. Wright, *Numerical Optimization, 2nd. ed.*, Springer, 2006.

[13] L.R Dice, "Measures of the amount of ecologic association between species," *Ecology*, vol. 26, no. 3, pp. 297–302, 1945.

Appendix F

List of brain regions

ACB	Nucleus accumbens
AHN	Anterior hypothalamic nucleus
AOB	Accessory olfactory bulb
AP	Area postrema
ARH	Arcuate hypothalamic nucleus
AUDd	Dorsal auditory area
BLA	Basolateral amygdalar nucleus
BMA	Basomedial amygdalar nucleus
BST	Bed nuclei of the stria terminalis
CA1	Field CA1
CA2	Field CA2
CA3	Field CA3
CEA	Central amygdalar nucleus
COA	Cortical amygdalar area
CU	Cuneate nucleus
DG	Dentate gyrus
DMH	Dorsomedial nucleus of the hypothalamus
DMX	Dorsal motor nucleus of the vagus nerve
DR	Dorsal nucleus raphe
ECT	Ectorhinal area
ECU	External cuneate nucleus
GENd	Geniculate group, dorsal thalamus
GR	Gracile nucleus

IC	Inferior colliculus
LC	Locus ceruleus
LH	Lateral habenula
LHA	Lateral hypothalamic area
LPO	Lateral preoptic area
LRNM	Lateral reticular nucleus, magnocellular part
LS	Lateral septal nucleus
LSc	Lateral septal nucleus, caudal part
ME	Median eminence
MEA	Medial amygdalar nucleus
MEPO	Median preoptic nucleus
MH	Medial habenula
MM	Medial mammillary nucleus
MPT	Medial pretectal area
MRN	Midbrain reticular nucleus
MTN	Midline group of the dorsal thalamus
NI	Nucleus incertus
NLL	Nucleus of the lateral lemniscus
NTS	Nucleus of the solitary tract
OV	Vascular organ of the lamina terminalis
PAG	Periaqueductal gray
PB	Parabrachial nucleus
PCG	Pontine central gray
PG	Pontine gray
PH	Posterior hypothalamic nucleus
PMv	Ventral premammillary nucleus
PSTN	Parasubthalamic nucleus
PVH	Paraventricular hypothalamic nucleus
PVp	Periventricular hypothalamic nucleus, posterior part
PVT	Paraventricular nucleus of the thalamus
RE	Nucleus of reunions
RHP	Retrohippocampal region
SCH	Suprachiasmatic nucleus
SCm	Superior colliculus, motor related
SF	Septofimbrial nucleus
SFO	Subfornical organ
SNc	Substantia nigra, compact part
SNr	Substantia nigra, reticular part
SO	Supraoptic nucleus
SPVC	Spinal nucleus of the trigeminal, caudal part
SSs	SSupplemental somatosensory area

TTd	Taenia tecta, dorsal part
TU	Tuberal nucleus
V4	fourth ventricle
VL	lateral ventricle
VMH	Ventromedial hypothalamic nucleus
VTA	Ventral tegmental area
ZI	Zona incerta

Bibliography

[AZM+16] Courtney M Anderson, Bingqing Zhang, Melanie Miller, Emerald Butko, Xingyong Wu, Thomas Laver, Casey Kernag, Jeffrey Kim, Yuling Luo, Henry Lamparski, et al. Fully automated rnascope in situ hybridization assays for formalin-fixed paraffin-embedded cells and tissues. *Journal of cellular biochemistry*, 117(10):2201–2208, 2016.

[BDL+14] Eglantine Balland, Julie Dam, Fanny Langlet, Emilie Caron, Sophie Steculorum, Andrea Messina, S Rasika, Anthony Falluel-Morel, Youssef Anouar, Bénédicte Dehouck, et al. Hypothalamic tanycytes are an erk-gated conduit for leptin into the brain. *Cell metabolism*, 19(2):293–301, 2014.

[BH95] Yoav Benjamini and Yosef Hochberg. Controlling the false discovery rate: a practical and powerful approach to multiple testing. *Journal of the royal statistical society. Series B (Methodological)*, pages 289–300, 1995.

[BM09] Susann Blüher and Christos S Mantzoros. Leptin in humans: lessons from translational research. *The American journal of clinical nutrition*, 89(3):991S–997S, 2009.

[BSD+03] Sarah H Bates, Walter H Stearns, Trevor A Dundon, Markus Schubert, et al. Stat3 signalling is required for leptin regulation of energy balance but not reproduction. *Nature*, 421(6925):856, 2003.

[C+09] Prospective Studies Collaboration et al. Body-mass index and cause-specific mortality in 900 000 adults: collaborative analyses of 57 prospective studies. *The Lancet*, 373(9669):1083–1096, 2009.

[CBSP16] Carlos A Campos, Anna J Bowen, Michael W Schwartz, and Richard D Palmiter. Parabrachial cgrp neurons control meal termination. *Cell metabolism*, 23(5):811–820, 2016.

[CCT+96] Hong Chen, Olga Charlat, Louis A Tartaglia, Elizabeth A Woolf, Xun Weng, Stephen J Ellis, Nathan D Lakey, Janice Culpepper, Karen J More, Roger E Breitbart, et al. Evi-

dence that the diabetes gene encodes the leptin receptor: identification of a mutation in the leptin receptor gene in db/db mice. *Cell*, 84(3):491–495, 1996.

[CDdLS98] Nancy L Chamberlin, Bin Du, Sonsoles de Lacalle, and Clifford B Saper. Recombinant adeno-associated virus vector: use for transgene expression and anterograde tract tracing in the cns. *Brain research*, 793(1):169–175, 1998.

[CET01] Timothy F. Cootes, Gareth J. Edwards, and Christopher J. Taylor. Active appearance models. *IEEE Transactions on pattern analysis and machine intelligence*, 23(6):681–685, 2001.

[CHAA14] Haijiang Cai, Wulf Haubensak, Todd E Anthony, and David J Anderson. Central amygdala pkc-[delta]+ neurons mediate the influence of multiple anorexigenic signals. *Nature neuroscience*, 17(9):1240–1248, 2014.

[CM12] John Cawley and Chad Meyerhoefer. The medical care costs of obesity: an instrumental variables approach. *Journal of health economics*, 31(1):219–230, 2012.

[Col78] Douglas L Coleman. Obese and diabetes: two mutant genes causing diabetes-obesity syndromes in mice. *Diabetologia*, 14(3):141–148, 1978.

[CRH+15] Simon C Cork, James E Richards, Marie K Holt, Fiona M Gribble, Frank Reimann, and Stefan Trapp. Distribution and characterisation of glucagon-like peptide-1 receptor expressing cells in the mouse brain. *Molecular metabolism*, 4(10):718–731, 2015.

[CSZP13] Matthew E Carter, Marta E Soden, Larry S Zweifel, and Richard D Palmiter. Genetic identification of a neural circuit that suppresses appetite. *Nature*, 503(7474):111, 2013.

[DBT+01] ME Dickinson, G Bearman, S Tille, R Lansford, and SE Fraser. Multi-spectral imaging and linear unmixing add a whole new dimension to laser scanning fluorescence microscopy. *Biotechniques*, 31(6):1272–1279, 2001.

[DCZ+03] Matthew J During, Lei Cao, David S Zuzga, Jeremy S Francis, Helen L Fitzsimons, Xiangyang Jiao, Ross J Bland, Matthias Klugmann, William A Banks, Daniel J Drucker, et al. Glucagon-like peptide-1 receptor is involved in learning and neuroprotection. *Nature medicine*, 9(9):1173, 2003.

[Dic45] Lee R Dice. Measures of the amount of ecologic association between species. *Ecology*, 26(3):297–302, 1945.

[DLS+07] Hans-Ulrich Dodt, Ulrich Leischner, Anja Schierloh, Nina Jährling, Christoph Peter Mauch, Katrin Deininger, Jan Michael Deussing, Matthias Eder, Walter Zieglgänsberger, and Klaus Becker. Ultramicroscopy: three-dimensional visualization of neuronal networks in the whole mouse brain. *Nature methods*, 4(4):331, 2007.

[DM98] IL Dryden and KV Mardia. *Statistical analysis of shape*. Wiley, 1998.

[EBJ+12] Ali Ertürk, Klaus Becker, Nina Jährling, Christoph P Mauch, Caroline D Hojer, Jackson G Egen, Farida Hellal, Frank Bradke, Morgan Sheng, and Hans-Ulrich Dodt. Three-dimensional imaging of solvent-cleared organs using 3disco. *Nature protocols*, 7(11):1983, 2012.

[EES99] Joel K Elmquist, Carol F Elias, and Clifford B Saper. From lesions to leptin: hypothalamic control of food intake and body weight. *Neuron*, 22(2):221–232, 1999.

[FCKO12] Katherine M Flegal, Margaret D Carroll, Brian K Kit, and Cynthia L Ogden. Prevalence of obesity and trends in the distribution of body mass index among us adults, 1999-2010. *Jama*, 307(5):491–497, 2012.

[FEB+11] Vladimir Fonov, Alan C Evans, Kelly Botteron, C Robert Almli, Robert C McKinstry, D Louis Collins, Brain Development Cooperative Group, et al. Unbiased average age-appropriate atlases for pediatric studies. *Neuroimage*, 54(1):313–327, 2011.

[FH98] Jeffrey M Friedman and Jeffrey L Halaas. Leptin and the regulation of body weight in mammals. *Nature*, 395(6704):763, 1998.

[FSC+11] Mariel M Finucane, Gretchen A Stevens, Melanie J Cowan, Goodarz Danaei, John K Lin, Christopher J Paciorek, Gitanjali M Singh, Hialy R Gutierrez, Yuan Lu, Adil N Bahalim, et al. National, regional, and global trends in body-mass index since 1980: systematic analysis of health examination surveys and epidemiological studies with 960 country-years and 9· 1 million participants. *The Lancet*, 377(9765):557–567, 2011.

[HBBW+97] Jeffrey L Halaas, Carol Boozer, John Blair-West, Naseem Fidahusein, Derek A Denton, and Jeffrey M Friedman. Physiological response to long-term peripheral and central leptin infusion in lean and obese mice. *Proceedings of the National Academy of Sciences*, 94(16):8878–8883, 1997.

[HM06] Eldad Haber and Jan Modersitzki. Intensity gradient based registration and fusion of multi-modal images. *Medical Image Computing and Computer-Assisted Intervention–MICCAI 2006*, pages 726–733, 2006.

[KS15] Stefan Klein and Marius Staring. *elastix the manual*. http://elastix.isi.uu.nl/, 2015.

[KSM+10] Stefan Klein, Marius Staring, Keelin Murphy, Max A Viergever, and Josien PW Pluim. Elastix: a toolbox for intensity-based medical image registration. *IEEE transactions on medical imaging*, 29(1):196–205, 2010.

[LHA+07] Ed S Lein, Michael J Hawrylycz, Nancy Ao, Mikael Ayres, Amy Bensinger, Amy Bernard, Andrew F Boe, Mark S Boguski, Kevin S Brockway, Emi J Byrnes, et al. Genome-wide atlas of gene expression in the adult mouse brain. *Nature*, 445(7124):168, 2007.

[LLL+13] Fanny Langlet, Barry E Levin, Serge Luquet, Massimiliano Mazzone, Andrea Messina, Ambrose A Dunn-Meynell, Eglantine Balland, Amelie Lacombe, Daniele Mazur, Peter Carmeliet, et al. Tanycytic vegf-a boosts blood-hypothalamus barrier plasticity and access

of metabolic signals to the arcuate nucleus in response to fasting. *Cell metabolism*, 17(4):607–617, 2013.

[MFB04] Heike Mu¨nzberg, Jeffrey S Flier, and Christian Bjørbæk. Region-specific leptin resistance within the hypothalamus of diet-induced obese mice. *Endocrinology*, 145(11):4880–4889, 2004.

[MHN+10] Anne-Sophie Montcuquet, Lionel Herve, Fabrice Navarro, Jean-Marc Dinten, and Jérôme I Mars. Nonnegative matrix factorization: a blind spectra separation method for in vivo fluorescent optical imaging. *Journal of biomedical optics*, 15(5):056009–056009, 2010.

[MLS99] Istvan Merchenthaler, Malcolm Lane, and Paul Shughrue. Distribution of pre-proglucagon and glucagon-like peptide-1 receptor messenger rnas in the rat central nervous system. *Journal of Comparative Neurology*, 403(2):261–280, 1999.

[MMLL09] Martin G Myers, Heike Münzberg, Gina M Leinninger, and Rebecca L Leshan. The geometry of leptin action in the brain: more complicated than a simple arc. *Cell metabolism*, 9(2):117–123, 2009.

[Mon17] Douglas C Montgomery. *Design and analysis of experiments*. John Wiley & Sons, 2017.

[NBF+11] Edward A Neuwelt, Björn Bauer, Christoph Fahlke, Gert Fricker, Constantino Iadecola, Damir Janigro, Luc Leybaert, Zoltán Molnár, Martha O'Donnell, John Povlishock, et al. Engaging neuroscience to advance translational research in brain barrier biology. *Nature reviews. Neuroscience*, 12(3):169, 2011.

[NHF+06] MA Nauck, M Hompesch, R Filipczak, TDT Le, M Zdravkovic, and J Gumprecht. Five weeks of treatment with the glp-1 analogue liraglutide improves glycaemic control and lowers body weight in subjects with type 2 diabetes. *Experimental and clinical endocrinology & diabetes*, 114(08):417–423, 2006.

[oBS17] Allen Institute of Brain Science. http://help.brain-map.org/display/mousebrain/documentation?preview=/2818169/8454277/mouseccf.pdf, 2017.

[OGGC+16] Patrick M O'Neil, W Timothy Garvey, J Michael Gonzalez-Campoy, Pablo Mora, Rafael Violante Ortiz, German Guerrero, Birgitte Claudius, and Xavier Pi-Sunyer. Effects of liraglutide 3.0 mg on weight and risk factors in hispanic versus non-hipanic populations: Subgroup analysis from scale randomized trials. *Endocrine Practice*, 22(11):1277–1287, 2016.

[OHN+14] Seung Wook Oh, Julie A Harris, Lydia Ng, Brent Winslow, Nicholas Cain, Stefan Mihalas, Quanxin Wang, Chris Lau, Leonard Kuan, Alex M Henry, et al. A mesoscale connectome of the mouse brain. *Nature*, 508(7495):207, 2014.

[PCQ+16] Chenchen Pan, Ruiyao Cai, Francesca Paola Quacquarelli, Alireza Ghasemigharagoz, Athanasios Lourbopoulos, Paweł Matryba, Nikolaus Plesnila, Martin Dichgans, Farida Hellal, and Ali Ertürk. Shrinkage-mediated imaging of entire organs and organisms using udisco. *Nature*, 201:6, 2016.

[PK01] Weihong Pan and Abba J Kastin. Diurnal variation of leptin entry from blood to brain involving partial saturation of the transport system. *Life sciences*, 68(24):2705–2714, 2001.

[PLJM11] Christa M Patterson, Rebecca L Leshan, Justin C Jones, and Martin G Myers. Molecular mapping of mouse brain regions innervated by leptin receptor-expressing cells. *Brain research*, 1378:18–28, 2011.

[RAK+16] Nicolas Renier, Eliza L Adams, Christoph Kirst, Zhuhao Wu, Ricardo Azevedo, Johannes Kohl, Anita E Autry, Lolahon Kadiri, Kannan Umadevi Venkataraju, Yu Zhou, et al. Mapping of brain activity by automated volume analysis of immediate early genes. *Cell*, 165(7):1789–1802, 2016.

[RLM08] Scott A Robertson, Gina M Leinninger, and Martin G Myers. Molecular and neural mediators of leptin action. *Physiology & behavior*, 94(5):637–642, 2008.

[RP06] Michael H Ross and Wojciech Pawlina. *Histology*. Lippincott Williams & Wilkins, 2006.

[RSH+99] Daniel Rueckert, Luke I Sonoda, Carmel Hayes, Derek LG Hill, Martin O Leach, and David J Hawkes. Nonrigid registration using free-form deformations: application to breast mr images. *IEEE transactions on medical imaging*, 18(8):712–721, 1999.

[RWS+14] Nicolas Renier, Zhuhao Wu, David J Simon, Jing Yang, Pablo Ariel, and Marc Tessier-Lavigne. idisco: a simple, rapid method to immunolabel large tissue samples for volume imaging. *Cell*, 159(4):896–910, 2014.

[SGAS+14] Stephanie Sisley, Ruth Gutierrez-Aguilar, Michael Scott, David A D'Alessio, Darleen A Sandoval, and Randy J Seeley. Neuronal glp1r mediates liraglutide's anorectic but not glucose-lowering effect. *The Journal of clinical investigation*, 124(6):2456, 2014.

[SH13] Roland Sturm and Aiko Hattori. Morbid obesity rates continue to rise rapidly in the us. *International journal of obesity (2005)*, 37(6):889, 2013.

[SHH99] Colin Studholme, Derek LG Hill, and David J Hawkes. An overlap invariant entropy measure of 3d medical image alignment. *Pattern recognition*, 32(1):71–86, 1999.

[SJB+14] Anna Secher, Jacob Jelsing, Arian F Baquero, Jacob Hecksher-Sørensen, Michael A Cowley, Louise S Dalbøge, Gitte Hansen, Kevin L Grove, Charles Pyke, Kirsten Raun, et al. The arcuate nucleus mediates glp-1 receptor agonist liraglutide-dependent weight loss. *The Journal of clinical investigation*, 124(10):4473, 2014.

[SLL+13] Marie Schaeffer, Fanny Langlet, Chrystel Lafont, François Molino, David J Hodson, Thomas Roux, Laurent Lamarque, Pascal Verdié, Emmanuel Bourrier, Bénédicte Dehouck, et al. Rapid sensing of circulating ghrelin by hypothalamic appetite-modifying neurons. *Proceedings of the National Academy of Sciences*, 110(4):1512–1517, 2013.

[SRQ+01] Julia A Schnabel, Daniel Rueckert, Marcel Quist, Jane M Blackall, Andy D Castellano-Smith, Thomas Hartkens, Graeme P Penney, Walter A Hall, Haiying Liu, Charles L Truwit, et al. A generic framework for non-rigid registration based on non-uniform multi-level free-form deformations. In *International Conference on Medical Image Computing and Computer-Assisted Intervention*, pages 573–581. Springer, 2001.

[TC15] Stefan Trapp and Simon C Cork. Ppg neurons of the lower brain stem and their role in brain glp-1 receptor activation. *American Journal of Physiology-Regulatory, Integrative and Comparative Physiology*, 309(8):R795–R804, 2015.

[VCSJ+14] J Van Can, B Sloth, CB Jensen, A Flint, EE Blaak, and WHM Saris. Effects of the once-daily glp-1 analog liraglutide on gastric emptying, glycemic parameters, appetite and energy metabolism in obese, non-diabetic adults. *International journal of obesity (2005)*, 38(6):784, 2014.

[VL09] Koen Van Leemput. Encoding probabilistic brain atlases using bayesian inference. *IEEE Transactions on Medical Imaging*, 28(6):822–837, 2009.

[VL10] Niels Vrang and Philip Just Larsen. Preproglucagon derived peptides glp-1, glp-2 and oxyntomodulin in the cns: role of peripherally secreted and centrally produced peptides. *Progress in neurobiology*, 92(3):442–462, 2010.

[WFS+12] Fay Wang, John Flanagan, Nan Su, Li-Chong Wang, Son Bui, Allissa Nielson, Xingyong Wu, Hong-Thuy Vo, Xiao-Jun Ma, and Yuling Luo. Rnascope: a novel in situ rna analysis platform for formalin-fixed, paraffin-embedded tissues. *The Journal of Molecular Diagnostics*, 14(1):22–29, 2012.

[WZW04] Simon K Warfield, Kelly H Zou, and William M Wells. Simultaneous truth and performance level estimation (staple): an algorithm for the validation of image segmentation. *IEEE transactions on medical imaging*, 23(7):903–921, 2004.

[ZMMH02] Mette Zander, Sten Madsbad, Jan Lysgaard Madsen, and Jens Juul Holst. Effect of 6-week course of glucagon-like peptide 1 on glycaemic control, insulin sensitivity, and β-cell function in type 2 diabetes: a parallel-group study. *The Lancet*, 359(9309):824–830, 2002.